EXACT COHERENT STRUCTURES IN SPATIOTEMPORAL CHAOS: FROM QUALITATIVE DESCRIPTION TO QUANTITATIVE PREDICTIONS

A Thesis
Presented to
The Academic Faculty

by

Nazmi B. Budanur

In Partial Fulfillment
of the Requirements for the Degree
Doctor of Philosophy in the
School of Physics

Georgia Institute of Technology
version 2.0, Apr 3 2017

ACKNOWLEDGEMENTS

I would like to thank to my advisor Predrag Cvitanović for his guidance and support. I am tremendously grateful to him for patiently listening to all my ideas, even the ones that were obviously wrong. I believe the most valuable lesson I learned over the last three years is his approach to training researchers.

I would like to acknowledge collaborations with Daniel Borrero-Echeverry in our study of the two-modes system, and Ashley Willis, Mohammad Farazmand, and Kimberly Short in our study of the pipe flow. I am indebted to Xiong Ding for sharing his code for periodic Schur decomposition, and to Ruslan Davidchack for sharing his solution data set for Kuramoto-Sivashinsky system. In addition, I would like to thank to Evangelos Siminos, Francesco Fedele, Roman Grigoriev, John Gibson, Yohann Duguet, and Björn Hof for fruitful discussions; to the family of late G. Robinson, Jr. and NSF grant DMS-1211827 for financial support.

Lastly, I would like to thank to my family for their unconditional love and support.

TABLE OF CONTENTS

SUMMARY

The term spatiotemporal chaos refers to physical phenomena that exhibit irregular oscillations in both space and time. Examples of such phenomena range from cardiac dynamics to fluid turbulence, where the motion is described by nonlinear partial differential equations. It is well known from the studies of low-dimensional chaotic systems that the state space, the space of solutions to the governing dynamical equations, is shaped by the invariant sets such as equilibria, periodic orbits, and invariant tori. State space of partial differential equations is infinite-dimensional, nevertheless, recent computational advancements allow us to find their invariant solutions (exact coherent structures) numerically. In this thesis, we try to elucidate the chaotic dynamics of nonlinear partial differential equations by studying their exact coherent structures and invariant manifolds. Specifically, we investigate the Kuramoto-Sivashinsky equation, which describes the velocity of a flame front, and the Navier-Stokes equation for an incompressible fluid in a circular pipe.

An important aspect of the problems studied in this thesis is the presence of continuous symmetries, which complicates the state space by allowing solutions to have infinitely many symmetry copies. Therefore, the main problem addressed in the thesis is the symmetry reduction, i.e. a transformation to new coordinates where each symmetry-related solution is represented by one. We solve this problem for continuous translation and discrete reflection symmetries by the method of slices and invariant polynomials respectively. Reducing symmetries allows us to study unstable manifolds of high dimensional exact coherent structures such as relative equilibria and relative periodic orbits. Our visualizations of unstable manifolds unveil the structure of the state space in the vicinity of exact coherent structures.

Besides understanding the state space geometry, periodic orbits can also be used for predicting the long term behavior of chaotic systems by utilizing periodic orbit theory. We show with examples that these techniques successfully extend to systems with continuous symmetries, when relative periodic orbits are used in calculations. We argue with examples that the methods developed in this thesis can contribute towards devising a theory of turbulence with predictive capabilities.

CHAPTER I

INTRODUCTION

In this thesis, we study spatiotemporally chaotic systems with the methods of dynamical systems theory. In particular, our goal is to find the exact coherent structures in these systems and understand their roles in shaping dynamics. Ultimately, we would like to use this understanding to make quantitative predictions about the long term behavior of these systems. As it will be clear further in the thesis, this is an ambitious goal, hence the study that we present here is part of a longer research program. Specifically, we are going to focus on the systems with continuous symmetries and construction of symmetry invariant descriptions.

The term "spatiotemporal chaos" covers a wide range of phenomena in physics and chemistry, whenever a physical observable exhibits irregular patterns in both space and time while the underlying laws of dynamics are deterministic. Arguably, the most extensively studied problem of spatiotemporal chaos is the fluid turbulence, in which the laws of motion is governed by Navier-Stokes equation. In the next section, we are going to introduce the turbulence problem and the dynamical systems approach to it in an informal way to motivate the reader for the rest of the thesis.

1.1 Turbulence

Navier-Stokes equation

$$\mathbf{u}_\tau + \mathbf{u}\cdot\nabla\mathbf{u} = -\frac{\nabla p}{\rho} + \nu\nabla^2\mathbf{u} + \mathbf{f} \tag{1}$$

is purely classical statement of momentum conservation known since the 19^{th} century. In (1), $\mathbf{u}(\mathbf{x},\tau)$ is the velocity of the fluid as function of space $\mathbf{x}$ and time τ, $p(\mathbf{x},\tau)$ is pressure, $f(\mathbf{x},\tau)$ is external forcing, ρ and ν are respectively the density and the kinematic viscosity of the fluid. While it is possible to write Navier-Stokes equation on a single line, its solutions can be as complicated as the turbulent water waves in Figure 1. Understanding the nature of solutions $\mathbf{u}(\mathbf{x},\tau)$ to (1) is a big challenge for mathematicians and physicists. In the purely mathematical setting, existence and smoothness of solutions to the Navier-Stokes equation is listed as one of the millennium problems by the Clay Mathematics Institute [36]. In physics and engineering, one asks questions such as "under which conditions turbulence occurs?", "is turbulence transient or persistent?", "how are the physical observables effected by turbulence?", "are the turbulent solutions of Navier-Stokes equation organized in a certain way?"... The question, to which we will seek an answer in this thesis is the last one and the method we are going to follow to this end is the dynamical systems approach to turbulence.

From the dynamical systems viewpoint, turbulence is viewed as a motion in the infinite-dimensional state space, where the solutions of the Navier-Stokes equation (1) are defined. Let us try to explain what do we mean by this with a thought experiment: Suppose we marked the center of Figure 1 as $\mathbf{x}_0$ and measured the 3-dimensional fluid velocity at this point $\mathbf{u}(\mathbf{x}_0,\tau)$ for a time interval $[\tau_i,\tau_f]$. Then we can plot our measurements on a $3D$ graph and obtain a trajectory similar to the blue curve sketched in Figure 2 (a). Now let

Figure 1: Turbulent water waves (photo by Marcus Ranum).

us pick three more points on Figure 1 and repeat our measurements to obtain Figure 2 (b). While we can look only at three dimensions due to our visual limitations, we can think of Figure 2 (b) as a single trajectory in $4 \times 3 = 12$ dimensions. If we continue picking more and more points to cover entire Figure 1 and below it to until we reach the bottom of the ocean, the data we are going to collect would correspond to a trajectory in an infinite-dimensional space. Furthermore, if we know boundary conditions for the velocity field $\mathbf{u}(\mathbf{x}, \tau)$ at the ends of Figure 1, the layers below it, and on the bottom of the ocean; then we can, in principle, compute the shape of the water waves after time τ_f by solving Navier-Stokes equation (1) with incompressibility and free-surface conditions, using our final measurement $\mathbf{u}(\mathbf{x}, \tau_f)$ as the initial condition. In other words, the turbulent dynamics of fluid can be thought as a motion in an infinite-dimensional space.

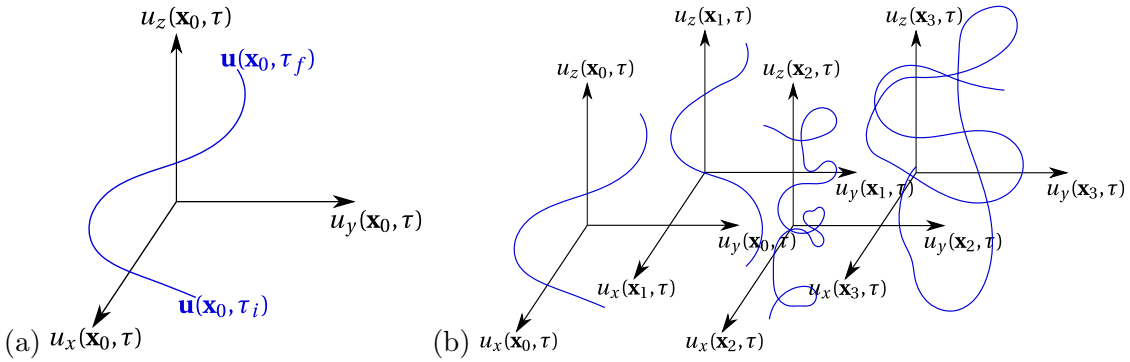

Figure 2: (a) Sketch of the fluid velocity measured at a single point $\mathbf{x}_0$ for a time interval. (b) Sketch of the fluid velocity measured at a points $\mathbf{x}_{0,1,2,3}$ for a time interval.

Now that we established the dynamical notion of turbulence as a trajectory in an infinite-dimensional space, we can repose the question of "How are the turbulent solutions organized?" as "What is the *geometry* of the *state space* of turbulence?"

In order to build an intuition, let us ask the same question for a much simpler problem with chaotic dynamics. An extensively studied nonlinear system of ordinary differential

equations is the Lorenz equations

$$\begin{aligned} \dot{x} &= \sigma(y-x)\,, \\ \dot{y} &= \rho x - y - xz\,, \\ \dot{z} &= xy - bz\,, \end{aligned} \tag{2}$$

which were derived as an extreme simplification of the Rayleigh-Benard problem by Edward Lorenz [74]. When parameters of (2) set to $\sigma = 10\,,\ \beta = 8/3\,,\ \rho = 28$, solutions of (2) yields the famous "butterfly" attractor shown in Figure 3 (a). The equilibria $E_{0,1,2}$ (points for which the RHS of (2) is 0) and the unstable manifold of E_0 are also shown in Figure 3 (a). As can be seen from Figure 3 (a), the borders of the Lorenz attractor is set by the unstable manifold of the equilibrium E_0 at the origin. Dynamics on two sides of the attractor is similar to the "spiral-out" dynamics in the neighborhood of equilibria E_1 and E_2. Thus, we observe that the equilibrium solutions play an important role in shaping the 3-dimensional state space of the Lorenz system.

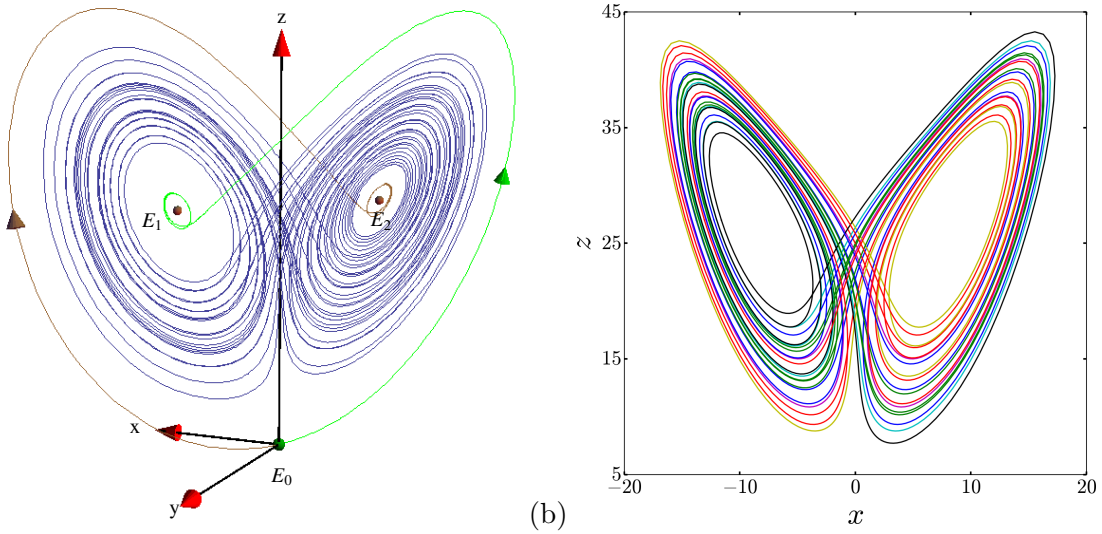

Figure 3: (a) Lorenz attractor (blue), its equilibria E_i, and the unstable manifold (brown and green) of the equilibrium E_0 . (b) 10 periodic orbits of the Lorenz system.

In Figure 3 (b), we show 10 periodic orbits of the Lorenz system (2), which we computed using the data provided in ref. [109]. Periodic orbits are trajectories that close onto themselves after a certain amount of time, and they seem to be embedded in the chaotic attractor as can be seen from Figure 3. In fact, we can use periodic orbits of a system to predict its long-term behavior using periodic orbit theory. Foundational ideas behind the periodic orbit theory goes as far back as Poincaré's geometric approach to the three body problem [86], and Birkhoff's proof of the ergodic theorem [10]. The key developments following them are seminal works of Smale [105], Sinai [102], Bowen [11], and Ruelle [98]; where the mathematical foundations of thermodynamic approach to the deterministic chaotic dynamics can be found. Following a different path Gutzwiller arrived at the periodic orbit sum formulas for the energy spectrum of the quantum mechanical systems [51, 52]. The long-term goal of the research program that this thesis is a part of is to extend these techniques for turbulence.

The dynamical approach to turbulence, which we tried to describe in this section, was first articulated in 1948 by Hopf [61]. However, it took more than 40 years for researchers

to start to numerically find invariant solutions of Navier-Stokes equation [82]. Since then, many groups started to compute equilibria, traveling wave, periodic, and relative periodic solutions of plane Couette flow [67, 83, 110] and pipe flow [34, 113, 115]. In fluid dynamics literature, these solutions are usually referred to as 'exact coherent structures' [112] (we avoid the term 'exact coherent states' [111], as that has a well established and different meaning in quantum mechanics). We adopt this terminology in this thesis when we talk about these solutions in fluid dynamics context. In addition to computation of the exact coherent structures, Gibson *et al.* [45] discovery and low-dimensional visualizations of heteroclinic connections in the plane Couette flow is one of the most significant developments in the dynamical description of turbulence.

1.2 Idealized geometries and symmetries

Our thought experiment of the previous section was too ambitious for a real life implementation. In reality, one studies the turbulence in much simpler geometries; such as water flowing through a circular pipe (pipe flow, Figure 4 (a)), or between walls that move in opposite direction (plane Couette flow, Figure 4 (b)). In these settings, fluid velocity at the bounding walls, relative to the wall vanishes and if the experiment is carried out on a computer, one typically imposes periodic boundary conditions in the unbounded directions.

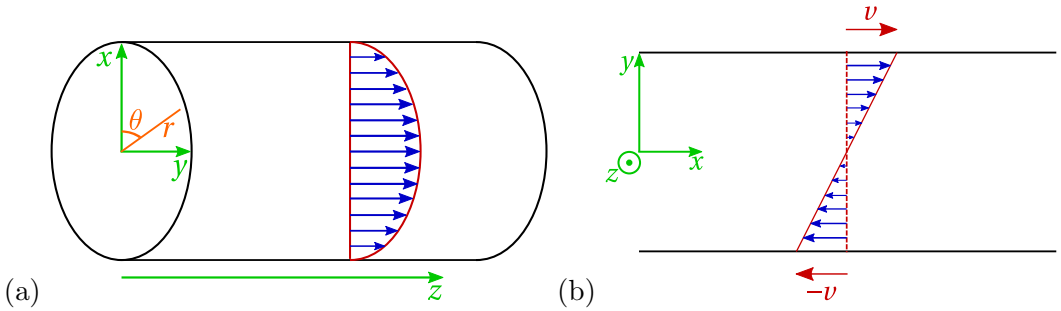

Figure 4: (a) Schematic of the pipe flow with the sketch (blue) of the laminar velocity profile. (b) Schematic of the plane Couette flow with the sketch (blue) of the laminar velocity profile.

Navier-Stokes equation (1) does not have an explicit dependence on space coordinates, which is a confirmation of the fact that governing laws of physics does not change if you move in space. Therefore, the turbulence problem in simple geometries such as the ones illustrated in Figure 4 admits symmetries of the system. This, however, does not mean that all the solutions of Navier-Stokes equation must have the symmetries of the problem. In fact, turbulent structures, such as the ones in Figure 1 never have symmetries. The fact that problem has symmetries only implies that one can obtain new solutions by applying symmetry transformations to the known ones. This distinction and its implications are of central importance for this thesis and we are going to study them in depth. As an example, consider the pipe flow, in which one applies a net pressure gradient in z direction to sustain a constant mean flow, thus all of its solutions drift in z direction. This physical constraint disallows having stationary solutions such as those of the Lorenz system in Figure 3 (a); thus the simplest nontrivial exact coherent structure one could obtain in this setting is a traveling wave (relative equilibrium) that is a steady wave profile drifting in z direction at a constant speed. Similarly, roles of periodic orbit in pipe flow are also taken over by relative

periodic orbit, which are wave forms that recur exactly after a certain period at a shifted location.

According to Cushman, Bates [19] and Yoder [120], an early study of relative equilibria was the work of Huyghens' [63] on the spherical pendulum. Vierkandt [108] showed that all solutions of the rolling disk are periodic, if the continuous symmetry of the system is reduced. According to Chenciner [17], Poincaré [86] was first to propose finding relative periodic solutions of the three body problem. In more recent mathematics literature, foundational works on the dynamical systems with symmetries are those of Smale [106], Field [40], and Ruelle [97]. In plane Couette flow, Nagata [83] was first to find a non-trivial traveling wave solution and Viswanath [110] was first to find a relative periodic orbit numerically. Traveling waves in pipe flow were first discovered by Faisst and Eckhardt [34] and relative periodic orbits of the pipe flow was first found by Duguet *et al.* [32]. These developments and many others that followed significantly improved our understanding of turbulence at transitional Reynolds numbers, which we will review in Chapter 6.

Presence of continuous symmetries add a "redundant" degree of freedom to the state space, since almost all solutions have continuously many symmetry copies. Such a redundant degree of freedom is undesirable for us since our objective is to find dynamical relations between exact coherent structures in order to understand the geometry of the state space. For this reason, the main problem to be addressed in this thesis is the 'translation symmetry reduction', that is, finding symmetry-invariant representations for systems with translation symmetry.

1.3 Overview of this thesis and its results

This thesis is divided into seven chapters including the current one. The next chapter is a very brief summary of the theory of nonlinear dynamics that will be applied to the problems in the rest of the thesis. A reader who is familiar with nonlinear dynamics and periodic orbit theory may safely skip Chapter 2. If you are familiar with nonlinear dynamics, but have never seen Perron-Frobenius operator and trace formulas, then you may find it useful to review Sect. 2.2. Chapter 3 is devoted to the main problem of this thesis. In this chapter, we introduce the SO(2) symmetry reduction problem, in a system-independent way, and describe its solution via method of slices. Following three chapters presents applications of the symmetry reduction to the problems of increasing difficulty. Our first application, the two-modes system (Chapter 4), is a toy problem that has the same symmetry structure with the problems to follow. In this example, we carry out all steps, including finding all periodic orbits and computing dynamical averages with them, that one should apply to spatiotemporally chaotic systems. The second example is the Kuramoto-Sivashinsky system, where in addition to the translation symmetry, we also have a reflection symmetry. In Chapter 5, we introduce reflection-invariant polynomials that take care of the remaining symmetry of the Kuramoto-Sivashinsky system, and within its fully-reduced state space we study Kuramoto-Sivashinsky system's transition to chaos via torus-breakdown. Finally in Chapter 6, we introduce the pipe flow, explain how its stream-wise translation symmetry is reduced, and what one learns afterwards. We summarize our conclusions and outline some future directions in Chapter 7

CHAPTER II

NONLINEAR DYNAMICS AND THE PERIODIC ORBIT THEORY

In this chapter, we introduce the essential concepts of nonlinear dynamics and periodic orbit theory; and set up the notation for the rest of the thesis. The material covered in this chapter is summary of the first 22 chapters of the ChaosBook.org [24], which as of this writing, spans 412 pages with figures, examples, and exercises. In other words, the purpose of this chapter is not to teach reader the periodic orbit theory, but to provide a quick reference for rest of the thesis.

2.1 Basics of dynamics

As a mathematical abstraction, a dynamical system is defined by its *state space* $\mathcal{M} \in \mathbb{R}^D$ and evolution rule $f^\tau(a)$ that maps every point in the state space (or a state vector) $a(0) \in \mathcal{M}$ to $a(\tau) \in \mathcal{M}$ after some time τ. A dynamical system for which τ takes discrete values is called a *map*, whereas the one for which τ takes continuous values is called a *flow*. Our main interest in this thesis will be flows that can be described by a set of first order ordinary differential equations ([**ode??**]s):

$$\dot{a} = v(a)\,. \tag{3}$$

Elements of a and the form of v depend on the underlying problem and physical laws. For example, when (3) describes a classical mechanics problem, then a consists of position and momenta of the particles involved, and $v(a)$ reflects Newton's laws of motion. Whereas if (3) describes an electrical circuit, then a has voltages across capacitors and currents flowing through the inductors and $v(a)$ is determined by Kirchoff's laws and the terminal relations of components.

2.1.1 Linear versus nonlinear

If (3) can be brought into the following form

$$\dot{a} = Aa\,, \tag{4}$$

where A is a $d \times d$ matrix, the flow is said to be *linear*, since its velocity function is linear in a . In this case, the solution is immediately given by the matrix exponential:

$$a(\tau) = e^{A\tau}a(0)\,, \text{ where } \quad e^{A\tau} = \sum_{n=0}^{\infty} \frac{(A\tau)^n}{n!}\,. \tag{5}$$

Thus, if A is diagonalizable, understanding the dynamics is equivalent to finding eigenvalues (λ_i) and eigenvectors (v_i) of A. Suppose that they satisfy $Av_i = \lambda_i v$, and the initial condition can be decomposed into $a(0) = \sum_i c_i v_i$, then we can rewrite (5) as

$$a(\tau) = \sum_i c_i e^{\lambda_i \tau} v_i\,. \tag{6}$$

From (6), it is clear that as time advances, the flow will expand in directions v_e with $Re[\lambda_e] > 0$ and components in directions v_c with $Re[\lambda_c] < 0$ will vanish. The former are

said to be *unstable* directions and the latter are called the *stable* directions. While (4) can describe only a small portion of what actually happens in nature, as we shall see, this notion of *linear stability* is essential in understanding general, nonlinear systems.

2.1.2 Equilibria, periodic orbits and their linear stability

2.1.2.1 Equilibria

[ode??] form of a flow given in (3) is sometimes referred to as the *Eulerian* description of the flow. We can write an equivalent description, so-called *Lagrangian* description of the flow by integrating (3):

$$a(\tau) = f^{\tau}(a_0)\,, \text{ where } \quad f^{\tau}(a_0) = a_0 + \int_0^{\tau} v(a(\tau))d\tau \tag{7}$$

An *equilibrium* is a special point such that its trajectory satisfies $f^t(a_{eq}) = a_{eq}$, equivalently $v(a_{eq}) = 0$. For the linear dynamical system described by (4), we described stable and unstable directions, in order to construct a similar notion for a nonlinear system, we consider the time evolution of small perturbations around a state space point a and expand (3) up to first order perturbations in every direction in the state space:

$$\dot{a}_i + \dot{\delta a}_i = v_i(a) + \sum_j \frac{\partial v_i(a)}{\partial a_j}\delta a_j\,. \tag{8}$$

We define the partial derivatives of velocity function as the *stability matrix*

$$A_{ij}(a) = \frac{\partial v_i(a)}{\partial a_j}\,. \tag{9}$$

For an equilibrium, by definition, $\dot{a}_{eq} = v(a_{eq}) = 0$, hence the time evolution of the small perturbations around the equilibrium is described by the linear relation

$$\dot{\delta a} = A(a_{eq})\delta a \tag{10}$$

In analogy with the linear case we described above, eigenvalues of $A(a_{eq})$ determine the stability of the equilibrium a_{eq} . If all eigenvalues of A, have negative real parts, then the equilibrium is called a *sink*; if some of them has negative and some of them has positive real parts, then the equilibrium called a *saddle*; and if all eigenvalues have positive real parts, then the equilibrium is called a *source*.

2.1.2.2 Periodic orbits

If every state space point on an orbit closes onto itself after evolving for a non-zero period T_p, then such an orbit is called a *periodic orbit*. In other words, if a_p is on a periodic orbit with period T_p then

$$a_p = f^{T_p}(a_p)\,. \tag{11}$$

Similar to the equilibrium, we study the stability of a periodic orbit again by investigating the time evolution

$$f^{\tau}(a_p + \delta a)_i = f^{\tau}(a_p)_i + \sum_j \left.\frac{\partial f^{T_p}(a)_i}{\partial a_j}\right|_{a=a_p} \delta a_j\,. \tag{12}$$

of a slightly perturbed trajectory. Second term in (12) determines the expansion of nearby perturbations to an orbit. We define the Jacobian of the flow as

$$J^\tau_{ij}(a_0) = \left.\frac{\partial f^\tau(a)_i}{\partial a_j}\right|_{a=a_0} . \tag{13}$$

Since for a periodic orbit, $f^{T_p}(a_p) = a_p$ stability of perturbations to the periodic orbit is determined by the Jacobian of the periodic orbit $J^p = J^{T_p}(a_p)$, which has a special name: the Floquet matrix. Eigenvalues Λ_i and eigenvectors V_i of the Floquet matrix, which we will refer as Floquet multipliers and Floquet vectors respectively, determines the stability of a periodic orbit. For every state space point on a periodic orbit, the Floquet matrix has at least one Floquet vector with unit multiplier, at the same direction with the flow velocity. In other words, velocity field evaluated at a state space point on a periodic orbit is an eigenvector of Floquet matrix with unit eigenvalue:

$$J^p v(a_p) = \Lambda_m v(a_p) \quad , \text{where } \Lambda_m = 1. \tag{14}$$

This simply states that if one perturbs the periodic orbit along the orbit itself, the flow stays on it. Directions with unit Floquet multipliers ($\Lambda_m = 1$) are called *marginal*. Directions with Floquet multipliers greater ($\Lambda_e > 1$) and lesser ($\Lambda_c < 1$) than 1 are respectively called *expanding* and *contracting*. As the names suggest, periodic orbit is unstable against the perturbations towards the former whereas it is stable against the perturbations towards the latter.

We shall now explain how we compute the Jacobian (13) numerically. For infinitesimal time $\delta\tau$, (13) becomes

$$\begin{aligned} J^{\delta\tau}_{ij}(a_0) &= \frac{\partial(a_{0,i} + v(a_{0,i})\delta\tau)}{\partial a_j} , \\ &= \delta_{ij} + A_{ij}(a_0)\delta\tau , \end{aligned} \tag{15}$$

from which we see that $J^0(a_0) = \mathbf{1}$. By definition (7), flows satisfy the semi-group property

$$f^{\tau_1}(f^{\tau_2}(a_0)) = f^{\tau_1+\tau_2}(a_0) . \tag{16}$$

Using which we can divide the evaluation of the perturbed flow into two steps

$$\begin{aligned} f^{\tau_1+\tau_2}(a_0 + \delta a) &= f^{\tau_1}(f^{\tau_2}(a_0) + J^{\tau_2}(a_0)\delta a) , \\ &= f^{\tau_1+\tau_2}(a_0) + J^{\tau_1}(f^{\tau_2}(a_0))J^{\tau_2}(a_0)\delta a . \end{aligned} \tag{17}$$

We again kept terms up to first order in perturbations and showed that along the trajectory, the Jacobian is multiplicative from the left: $J^{\tau_1+\tau_2} = J^{\tau_1}J^{\tau_2}$. Now we can divide a finite time trajectory into infinitesimal pieces and write the Jacobian using its multiplicative property as

$$J^\tau(a_0) = \lim_{m\to\infty} J^{\delta\tau}(a_{m-1})J^{\delta\tau}(a_{m-2})\dots J^{\delta\tau}(a_1)J^{\delta\tau}(a_0) \quad \text{where}, m = \tau/\delta\tau . \tag{18}$$

Substituting the definition of the short time Jacobian into (18), we get

$$\begin{aligned} J^\tau(a_0) &= \lim_{m\to\infty} (\mathbf{1} + A(a_{m-1})\delta\tau)(\mathbf{1} + A(a_{m-2})\delta\tau)\dots(\mathbf{1} + A(a_0)\delta\tau) , \\ &= \lim_{m\to\infty} e^{A(a_{m-1})\delta\tau} e^{A(a_{m-2})\delta\tau} \dots e^{A(a_0)\delta\tau} , \\ &= \mathbf{T} e^{\int_0^\tau d\tau A(a(\tau))} , \end{aligned} \tag{19}$$

where in the last step, we took the $m \to \infty$ limit and obtained the time-ordered integral. In practice, we solve

$$\dot{J}^\tau(a_0) = A(a(\tau))J^\tau(a_0)\,, \text{ where } \quad a(0) = a_0\,,\ J^0(a_0) = \mathbf{1}\,, \tag{20}$$

numerically along with the **[ode??]**s (3). One can easily check that (19) is the solution of (20).

2.1.3 Time-invariant sets

Since time evolution satisfies the semi-group property (16), we can talk about invariants of this semi-group action. The *orbit* of a state space point a_0 is the set of points $\mathcal{M}_{a_0}$, that can be reached from a_0 by the flow mapping (7)

$$\mathcal{M}_{a_0} = \{f^\tau(a_0)\,|\,\tau \in [0,\infty)\}\,. \tag{21}$$

The orbit (21) is by definition time invariant, that is if we act on the members of set (21) with the flow mapping (7) the new set of points we obtained are contained in (21). Equilibria and periodic orbits we defined in the previous section form "compact" time-invariant sets. Relative equilibria and relative periodic orbits, which we will introduce in the next chapter, also form time-invariant sets. In several places in this thesis, we call these states "invariant solutions" in reference to their time-invariance property.

2.2 Densities and averages

When a system is chaotic, numerical solutions of the equations of motion (3) describe trajectory of a state space point, with exponentially decreasing accuracy; hence they by themselves are not very useful for long-term predictions. However, as we shall see, we can think in terms of collection of state space points, *densities*, and define long-term expectation value of an observable as the average over an "invariant density". We are going to start with a few words on need for this way of thinking.

2.2.1 Chaos

Set of **[ode??]**s (3) which define a dynamical system are by definition time-invariant, hence we say that the system is deterministic. Laws of physics underlying the motions of streams in oceans or a double rod pendulum are also deterministic, yet, knowing them is not enough to predict how much energy will the waves dissipate this year, or how many full turns will the double pendulum make in a certain amount of time. The reason is chaos, which is the extreme dependence on the initial conditions. We can state this in mathematical terms as follows: Let δa_0 be an infinitesimal perturbation to the initial condition a_0. After some time τ, let us denote the image of the original and perturbed trajectory as

$$a(\tau) = f^\tau(a_0) \quad \text{and} \quad a(\tau) + \delta a(\tau) = f^\tau(a_0 + \delta a_0)\,. \tag{22}$$

For every a_0 in a bounded volume of the state space, if the magnitude $|\delta a_0|$ of the initial separations grow as

$$|\delta a(\tau)| \approx e^{\lambda\tau}|\delta a_0| \quad \text{with } \lambda > 0\,, \tag{23}$$

we say the dynamics is chaotic with the leading Lyapunov exponent λ.

Above statements of chaos tells us that it is impossible to predict much about a chaotic system by just solving equations of motions since no computer has infinite precision, or no measurement device can provide us a perfectly accurate initial condition. We thus, move from thinking in terms of points in the state space to thinking in terms of collection of them.

2.2.2 Evolving densities

A density $\rho(a,\tau)$ is a function of state space coordinates and time, which satisfies the normalization condition

$$\int_{\mathcal{M}} da\rho(a,\tau) = 1\,. \tag{24}$$

at all times. We think of a density as a continuous collection of state space points, each of which evolves according to the evolution rule (7). A density will also evolve in time, which we will describe by the action of Perron-Frobenius operator as

$$\begin{aligned}
\rho(a,\tau) &= [\mathcal{L}^\tau_{PF}\,\rho](a) && (25)\\
&= \int_{\mathcal{M}} da_0 \delta(a - f^\tau(a_0))\rho(a_0,0), && (26)\\
&= \frac{\rho(a_0,0)}{\left|\det \left.\frac{\partial f^\tau(a)}{\partial a}\right|_{a=a_0}\right|}\,, \quad \text{where } a = f^\tau(a_0)\\
&= \frac{\rho(a_0,0)}{|\det J^t(a_0)|}\,, \quad \text{where } a = f^\tau(a_0)\,, && (27)
\end{aligned}$$

where the last two steps followed from the integration over the delta function in (26) and we assumed every state space point a has only one pre-image. Since our attention here is restricted to deterministic flows, this assumption is valid.

In order to develop some intuition, we can think of the kernel

$$\mathcal{L}^\tau_{PF}(a,a_0) = \delta(a - f^\tau(a_0))\,. \tag{28}$$

of the Perron-Frobenius operator (26) as a matrix with continuous indices a and a_0 that runs over all state space. In this sense, Perron-Frobenius operator is an infinite dimensional transition matrix with a continuous time variable.

An *invariant density* or an *invariant measure* is a density that stays unchanged, in other words, $\rho(a)$ is called an invariant measure if it is an eigenfunction of Perron-Frobenius operator with unit eigenvalue

$$[\mathcal{L}^\tau_{PF}\rho](a) = \int_{\mathcal{M}} da_0 \delta(a - f^\tau(a_0))\rho(a_0) = \rho(a)\,. \tag{29}$$

It is possible to construct many invariant measures. Take, for example, a set of N_{eq} equilibria a_{eq}, then $\rho(a) = (1/N_{eq})\sum_{eq}\delta(a-a_{eq})$ by definition is stationary. Another invariant set can be a uniform density over all the points on a periodic orbit. An invariant measure that will be important for what comes next is the so-called *natural measure*, or *Sinai-Bowen-Ruelle measure*:

$$\rho_0(a) = \lim_{\tau\to\infty}\frac{1}{\tau}\int_0^\tau d\tau\delta(a - f^\tau(a_0))\,, \tag{30}$$

where a_0 is some initial point in $\mathcal{M}$. If the natural measure limit (30) exists, it is by definition an invariant measure since evolving it for finite time will not have an effect on infinite time limit.

2.2.3 Averages

As we stated earlier, state space coordinates of a system completely specifies its physical state and carries all relevant information at a certain instance. With this in mind, it is reasonable to assume that we can define *observables* as functions of state space coordinates. Let $\omega(a)$ be an observable that we can define on a system, then its average over a certain density is given by

$$\langle \omega \rangle_\rho = \int_{\mathcal{M}} da \rho(a) \omega(a) \,. \tag{31}$$

We dropped in (31) the time dependence of density $\rho(a)$ since it is of no importance, and assumed that it is normalized as in (24). Now let us evaluate (31) using the natural measure (30)

$$\begin{aligned} \langle \omega \rangle_{\rho_0} &= \lim_{\tau \to \infty} \frac{1}{\tau} \int_0^\tau d\tau \int_{\mathcal{M}} da \delta(a - f^\tau(a_0)) \omega(a) \,, \\ &= \lim_{\tau \to \infty} \frac{1}{\tau} \int_0^\tau d\tau \omega(f^\tau(a_0)) \,. \end{aligned} \tag{32}$$

We obtained in (32) that average of an observable over the natural measure (30) is its long time average. Existence of the limit (32) and its independence from the arbitrary initial point a_0 are important questions that we do not attempt to answer in this thesis. However, as we will show in our examples, this is not an unreasonable assumption.

In what follows, our goal is to develop a formalism to evaluate the integral

$$\langle \omega \rangle = \int_{\mathcal{M}} da \omega(a) \rho_0(a) \,, \tag{33}$$

which is the space average of the observable a over the natural measure, or as we have shown in (32), long time average of a.

We restrict our attention to scalar observables which are additive along an orbit and define the *evolution operator*

$$[\mathcal{L}^\tau \rho](a) = \int_{\mathcal{M}} da_0 \delta(a - f^\tau(a_0)) e^{\beta \Omega^\tau(a_0)} \rho(a_0, 0). \tag{34}$$

Here, β is an auxiliary variable and $\Omega^\tau(a_0)$ is the integrated value of the ω observable along the orbit $f^\tau(a_0)$, namely

$$\Omega^\tau(a_0) = \int_0^\tau \omega(a(\tau')) d\tau' \,, \quad a(0) = a_0. \tag{35}$$

Note that when $\beta \to 0$, the evolution operator becomes Perron-Frobenius operator (25). Since we required the observable ω to be additive along an orbit, the kernel

$$\mathcal{L}^\tau(a, a_0) = \delta(a - f^\tau(a_0)) e^{\beta \Omega^\tau(a_0)} \tag{36}$$

of the evolution operator (34) satisfies

$$\mathcal{L}^{\tau_2 + \tau_1}(a, a_0) = \int_{\mathcal{M}} da_1 \mathcal{L}^{\tau_2}(a, a_1) \mathcal{L}^{\tau_1}(a_1, a_0) \,. \tag{37}$$

Hence the evolution operator itself satisfies

$$\mathcal{L}^{\tau_2 + \tau_1} = \mathcal{L}^{\tau_2} \mathcal{L}^{\tau_1} \,. \tag{38}$$

Multiplicative, or *semi-group* property (38) of the evolution operator allows us to study its action in infinitesimal pieces as we can divide every trajectory into smaller and smaller steps and add them together. Let us consider the action of evolution operator (34) on a density for an infinitesimal time:

$$\begin{aligned}
[\mathcal{L}^{\delta\tau}\rho](a) &= \int da_0 e^{\beta\Omega^{\delta\tau}} \delta(a - f^{\delta\tau}(a_0))\rho(a_0) \\
&= \int da_0 e^{\beta\delta\tau\omega(a_0)} \delta(a - a_0 - \delta\tau v(a_0))\rho(a_0) \\
&= \int da_0 (1 + \beta\delta\tau\omega(a_0))\delta(a - a_0 - \delta\tau v(a_0))\rho(a_0) \\
&= (1 + \beta\delta\tau\omega(a)) \frac{\rho(a - \delta\tau v(a))}{\left|\det\left(1 + \delta\tau \left.\frac{\partial v(a_0)}{\partial a_0}\right|_{a_0=a}\right)\right|} \,. \qquad (39)
\end{aligned}$$

Denominator of (39) requires some care. We start by applying the identity $\ln\det M = \mathrm{tr}\,\ln M$ and expanding the logarithm to the linear order as

$$\begin{aligned}
\ln\det\left(1 + \delta\tau \left.\frac{\partial v(a_0)}{\partial a_0}\right|_{a_0=a}\right) &= \mathrm{tr}\,\ln\left(1 + \delta\tau \left.\frac{\partial v(a_0)}{\partial a_0}\right|_{a_0=a}\right) \\
&= \mathrm{tr}\,\delta\tau \left.\frac{\partial v(a_0)}{\partial a_0}\right|_{a_0=a} \\
&= \delta\tau \sum_i \left.\frac{\partial v_i(a_0)}{\partial a_{0i}}\right|_{a_0=a} \,. \qquad (40)
\end{aligned}$$

We exponentiate both sides and expand again to the linear order in $\delta\tau$ to obtain the denominator of (39) as $1 + \delta\tau\partial_i v_i(a_0)|_{a_0=a}$. Expanding the numerator also to the first order in $\delta\tau$ we obtain

$$[\mathcal{L}^{\delta\tau}\rho](a) = (1 + \beta\delta\tau\omega(a)) \left.\frac{\rho(a) - \delta\tau v_i(a_0)\partial_i\rho(a_0)}{1 + \delta\tau\partial_i v_i(a_0)}\right|_{a_0=a} \,. \qquad (41)$$

Multiplying and dividing RHS of the above equation by $1 - \delta\tau\partial_i v_i(a_0)$ and keeping terms up to the linear order in $\delta\tau$ we get

$$\begin{aligned}
[\mathcal{L}^{\delta\tau}\rho](a) &= (1 + \beta\delta\tau\omega(a))[\rho(a) - \delta\tau\partial_i(v_i(a_0)\rho(a_0))|_{a_0=a}] \\
&= \rho(a) + \beta\delta\tau\omega(a)\rho(a) - \delta\tau\partial_i(v_i(a_0)\rho(a_0))|_{a_0=a} \,. \qquad (42)
\end{aligned}$$

The final trick is to express the evolution operator in terms of its infinitesimal generator. Since it satisfies the semi-group property (38), we can express evolution operator formally as exponential of its infinitesimal generator $\mathcal{A}$,

$$\mathcal{L}^\tau = e^{\mathcal{A}\tau} \,. \qquad (43)$$

Eigenfunctions of the evolution operator are also the eigenfunctions of its generator, and corresponding eigenvalues are related by $S(\tau) = e^{\tau s}$, where s is the eigenvalue of $\mathcal{A}$. Now if we expand the infinitesimal-time evolution operator (42) in terms of its infinitesimal generator we obtain

$$\rho(a) + \delta\tau\mathcal{A}\rho(a) = \rho(a) + \beta\delta\tau\omega(a)\rho(a) - \delta\tau\partial_i(v_i(a_0)\rho(a_0))|_{a_0=a} \,, \qquad (44)$$

which simplifies as

$$\mathcal{A}\rho(a) = \beta\omega(a)\rho(a) - \partial_i(v_i(y)\rho(y))|_{y=a}\,. \tag{45}$$

Now we are going to restrict our consideration to the eigenfunctions of $\mathcal{A}$, which are functions of β satisfying,

$$\mathcal{A}\rho(a,\beta) = s(\beta)\rho(a,\beta)\,. \tag{46}$$

Note that $\rho(a,0) = \rho_0(a)$ and $s(0) = 0$. Plugging the eigenfunction $\rho(a,\beta)$ in (45) we get

$$s(\beta)\rho(a,\beta) = \beta\omega(a)\rho(a,\beta) - \partial_i(v_i(a_0)\rho(a_0,\beta))|_{a_0=a}\,. \tag{47}$$

This is the equation that we are going to use for relating long term average of the observable ω to the eigenvalue $s(\beta)$. We are going to carry out this calculation step-by-step, starting with differentiating (47) with respect to β:

$$s'(\beta)\rho(a,\beta) + s(\beta)\frac{\partial\rho(a,\beta)}{\partial\beta} = \omega(a)\rho(a,\beta) + \beta\omega(a)\frac{\partial\rho(a,\beta)}{\partial\beta} - \partial_i\left(v_i(a_0)\frac{\partial\rho(a_0,\beta)}{\partial\beta}\right)\Big|_{a_0=a}\,. \tag{48}$$

We now set $\beta \to 0$ and use $s(0) = 0$ and $\rho(a,0) = \rho_0(a)$ to obtain

$$s'(0)\rho_0(a) = \omega(a)\rho_0(a) - \partial_i((v_i(a_0)\frac{\partial}{\partial\beta}\rho(a_0,\beta))|_{a_0=a,\beta=0})\,, \tag{49}$$

finally we integrate over a dropping the divergence term (assuming the $\rho(a,\beta)$ vanishes on the surface at infinity) and get

$$s'(0) = \int da\omega(a)\rho_0(a) = \langle\omega\rangle\,. \tag{50}$$

We have found that we can generate the long time average of an observable by differentiating eigenvalues of the corresponding infinitesimal evolution operator. Before moving onto developing techniques to find these eigenvalues, let us see if we can extract any more information from $s(\beta)$.

We arrived at (50) by assuming the system in consideration produces the natural measure from all physically important initial distributions; and hence, the long term average of observables exist. For (50) to be valid, as $t \to \infty$, expectation value $\langle e^{\beta\Omega^\tau}\rangle$ must grow like

$$\langle e^{\beta\Omega^\tau}\rangle \propto e^{ts(\beta)}\,, \tag{51}$$

thus we can define $s(\beta)$ in terms of $\langle e^{\beta\Omega^\tau}\rangle$ as

$$s(\beta) = \lim_{\tau\to\infty}\frac{1}{\tau}\ln\langle e^{\beta\Omega^\tau}\rangle\,. \tag{52}$$

Let us first confirm (50)

$$\begin{aligned}\frac{\partial s(\beta)}{\partial\beta}\Big|_{\beta=0} &= \lim_{\tau\to\infty}\frac{1}{\tau}\frac{\langle\Omega^\tau e^{\beta\Omega^\tau}\rangle}{\langle e^{\beta\Omega^\tau}\rangle}\Big|_{\beta=0}\,,\\ &= \lim_{\tau\to\infty}\frac{1}{\tau}\langle\Omega^\tau\rangle\,,\\ &= \langle\omega\rangle\,.\end{aligned} \tag{53}$$

The second derivative

$$\left.\frac{\partial^2 s(\beta)}{\partial \beta^2}\right|_{\beta=0} = \lim_{\tau\to\infty}\frac{1}{\tau}\left.\frac{\langle\Omega^\tau\Omega^\tau e^{\beta\Omega^\tau}\rangle\langle e^{\beta\Omega^\tau}\rangle - \langle\Omega^\tau e^{\beta\Omega^\tau}\rangle\langle\Omega^\tau e^{\beta\Omega^\tau}\rangle}{\langle e^{\beta\Omega^\tau}\rangle^2}\right|_{\beta=0},$$
$$= \lim_{\tau\to\infty}\frac{1}{\tau}\left(\langle\Omega^\tau\Omega^\tau\rangle - \langle\Omega^\tau\rangle\langle\Omega^\tau\rangle\right). \tag{54}$$

gives us growth rate of the variance. We can obtain higher order moments by continuing taking derivatives but we stop here.

Equations (50–54) relate statistical moments of an observable to the leading eigenvalue of corresponding evolution operator (34). Thus, if we can find $s(\beta)$, we can generate long-term averages of observables from it. For this purpose we construct the resolvent of the infinitesimal evolution operator $\mathcal{A}$, by taking Laplace transform of $\mathcal{L}^\tau = e^{\mathcal{A}\tau}$

$$\int_0^\infty dt e^{-s\tau}\mathcal{L}^\tau = \frac{1}{s-\mathcal{A}}, \tag{55}$$

trace of which peaks at the eigenvalues of $\mathcal{A}$. Hence, we are going to compute Laplace transform of the trace of the evolution operator (34)

$$\int_0^\infty d\tau e^{-s\tau}\mathrm{tr}\,\mathcal{L}^\tau = \int_0^\infty d\tau e^{-s\tau}\int da\mathcal{L}^\tau(a,a),$$
$$= \int_0^\infty d\tau e^{-s\tau}\int da\delta(a-f^\tau(a))e^{\beta\Omega^\tau(a)}. \tag{56}$$

We see that periodic orbits will contribute to the trace (56).[1] We also know that integral over delta function in (56) will produce terms that are inversely proportional to $\det(1-J^\tau(a_p)) = \prod_k(1-\Lambda_k)$, which may cause a problem since every periodic orbit has one marginal ($\Lambda_m = 1$) Floquet multiplier corresponding to the perturbations along the orbit. In order to deal with this, for every periodic orbit we carry out (56) in a local coordinate frame. We transform from $(a_1, a_2, ..., a_d)$ to $(a_\parallel, a_{\perp,1}, a_{\perp,2}, ..., a_{\perp,d-1})$, where $a_\parallel$ is always parallel to the flow and $a_{\perp,i}$ are transverse. In this coordinate frame, we can write the contribution from a prime cycle[2] p to the trace (56) as

$$\int_0^\infty d\tau e^{-s\tau}\mathrm{tr}_p\mathcal{L}^\tau = \int_0^\infty d\tau e^{-s\tau}\int da_\parallel da_\perp\delta(a_\parallel - f^\tau(a)_\parallel)\delta(a_\perp - f^\tau(a)_\perp)e^{\beta\Omega^\tau(a)}. \tag{57}$$

Let us start with the integration along the orbit and the Laplace transform. By definition, velocity field $v(a)$ is parallel to the $a_\parallel$, and its value on the periodic orbit is completely specified by $a_\parallel$ hence, we can parametrize both of them by a flight time τ_f satisfying $da_\parallel = d\tau_f|v(a)|$ as

$$\int_0^\infty d\tau e^{-st}\oint da_\parallel\delta(a_\parallel - f^\tau(a)_\parallel) = \int_0^\infty d\tau e^{-s\tau}\int_0^{T_p} d\tau_f|v(\tau_f)|\delta(a_\parallel(\tau_f) - a_\parallel(\tau_f+\tau)). \tag{58}$$

Note that the integral over $a_\parallel$ is a loop integral, hence its time parametrization runs for only one period. Note also that $a_\parallel$ is a cyclic coordinate, hence, τ-integral will get contributions

[1] There can be contributions to the trace (56) from other invariant objects, such as equilibria and invariant tori. For a trace formula for an equilibrium, as well for tori generated by relative periodic orbits, see ref. [24].

[2] A periodic orbit that is not a repeat of a shorter one.

at every repeat of the periodic orbit:

$$\begin{aligned}\int_0^\infty d\tau e^{-s\tau} \oint da_\parallel \delta(a_\parallel - f^\tau(a)_\parallel) &= \int_0^{T_p} d\tau_f |v(\tau_f)| \int_0^\infty d\tau e^{-s\tau} \delta(a_\parallel(\tau_f) - a_\parallel(\tau_f+\tau)) \,, \\ &= \int_0^{T_p} d\tau_f |v(\tau_f)| \sum_{r=0}^\infty e^{-sT_p r} \frac{1}{|\partial a_\parallel/\partial\tau|_{\tau=rT_p}} \,, \\ &= T_p \sum_{r=0}^\infty e^{-sT_p r} \,, \end{aligned} \tag{59}$$

where we have used $|\partial a_\parallel/\partial\tau|_{\tau=rT_p}| = |v(\tau)|$ and in the last step, τ integration simply gave us the period of the prime cycle. Finally we compute the contribution from the transverse integral for the r^{th} repeat of the prime cycle p:

$$\int_r da_\perp \delta(a_\perp - f^{rT_p}(a)_\perp) = \frac{1}{\left|\det\left(\mathbf{1} - M_p^r\right)\right|} \,. \tag{60}$$

Where M_p is the transverse monodromy matrix, eigenvalues of which are those of the Jacobian J^p except the marginal eigenvalue corresponding to the velocity field direction. Summing over all the prime cycles, we obtain the *classical trace formula*

$$\sum_{\alpha=0}^\infty \frac{1}{s - s_\alpha} = \sum_p T_p \sum_{r=1}^\infty \frac{e^{r(\beta A_p - sT_p)}}{\left|\det\left(\mathbf{1} - M_p^r\right)\right|} \,, \tag{61}$$

where sum over α runs over the eigenvalues of the evolution operator. Classical trace formula (61) is the fundamental relation that will allow us determine the leading eigenvalue of the evolution operator (34) and hence the dynamical averages via its derivatives (50–54).

It is important to note that the classical trace formula (61) is independent of the choice of coordinates, since Floquet multipliers that will appear in the expansion of $\left|\det\left(\mathbf{1} - M_p^r\right)\right|$ are invariant under smooth changes of coordinates (see e.g. ref. [24] for a proof). Hence, long term averages of observables are independent from the particular parametrization of a problem.

Computationally, it is more convenient to search for zeros of a function, rather than its poles; for this purpose, one defines the *spectral determinant*

$$\det\left(s - \mathcal{A}\right) = \exp\left(-\sum_p \sum_{r=1}^\infty \frac{1}{r} \frac{e^{r(\beta A_p - sT_p)}}{\left|\det\left(\mathbf{1} - M_p^r\right)\right|}\right) \,, \tag{62}$$

logarithmic derivative of which yields (61). Computational aspects and convergence of (61) and (62) are non-trivial and require case-by-case attention. We will come back to these issues in Sect. 4.3 and Sect. 6.3.6.

CHAPTER III

CONTINUOUS SYMMETRIES

We mentioned in Sect. 1.2 with heuristic arguments that the spatiotemporally chaotic systems with continuous symmetries have redundant degrees of freedom. We start this chapter by restating this in mathematical terms and introducing the concept of "equivariance" and its implications. We then move on to the symmetry reduction by method of slices and present the central result of this study: SO(2) symmetry reduction by the first Fourier mode slice. For simplicity, we are going to present the techniques in this chapter for a one-dimensional scalar field with translation symmetry. We then generalize the first Fourier mode slice to higher spatial dimensions and direct products of SO(2).

3.1 Fields

In the preceding chapter, we introduced nonlinear dynamics and the periodic orbit theory for [**ode??**]s, but in this thesis we are interested in fields, dynamics of which is determined by nonlinear [**pde??**]s. For concreteness, let us consider a real valued scalar field $u(x,\tau)$ defined over a finite one-dimensional space $x \in [0, L]$ and time τ. Assume that its dynamics is determined by a [**pde??**] of the following form

$$u_\tau = \mathcal{N}(u, u_x, u_{xx}, u_{xxx}, \ldots)\,, \tag{63}$$

where subscripts τ and x indicates partial derivatives with respect to time and space respectively and $\mathcal{N}(.)$ is a general nonlinear functional of the field itself and its spatial derivatives. We will assume that the solutions of (63) exist, are unique, and evolve smoothly.

When we defined the dynamical system in Sect. 2.1, we stated that the state space vector contains all the necessary information regarding the physical state of a system at a time τ; the velocity vector contains the information of laws, which describes the evolution of the state space coordinates. Let us assume that we construct a state space vector which contains the value of the field $u(x,\tau)$ everywhere in space at a time τ

$$a(t) = (u(0,\tau), u(x_1,\tau), u(x_2,\tau), u(x_3,\tau), \ldots)^T\,, \quad x_i \in [0, L]\,. \tag{64}$$

We can then, in principle, construct a velocity vector that would describe the evolution of (64) by looking at the [**pde??**] (63). This, however, is not a trivial task since the space is continuous and as a result the state space vector (64) is infinite-dimensional. Nevertheless, we can think of a [**pde??**] as an *infinite-dimensional* dynamical system. This correspondence can be made explicit if we expand the field $u(x,t)$ as a sum over basis functions, which satisfy the boundary conditions of the problem and form a complete set. In particular, let us assume that we have periodic boundary conditions

$$u(x + L, \tau) = u(x, \tau)\,, \tag{65}$$

then the natural choice is an expansion in Fourier basis

$$u(x,\tau) = \sum_{k=-\infty}^{\infty} \tilde{u}_k(\tau) e^{iq_k x}\,, \quad \text{where } q_k = 2\pi k/L\,. \tag{66}$$

By plugging (66) in (63), we obtain an [**ode??**] for each Fourier mode $\tilde{u}_k$, since all partial derivatives with respect to x will be replaced by multiplications by iq_k. Furthermore, in diffusive systems that we consider in this thesis, higher Fourier modes (short wavelengths) are subjected to strong damping, hence a finite number of Fourier modes is typically enough to study dynamics numerically. Thus we reduce the state space dimension from infinite to a large, but finite number.

Our recipe for transforming a [**pde??**] to a set of [**ode??**]s is straightforward, however, imposing periodic boundary conditions comes at a cost: Since the value of the field $u(x,\tau)$ is subjected to the same boundary conditions at every point in $[0,L]$, each solution of the [**pde??**] (63) will have translation copies, namely, if $u(x,\tau)$ is a solution to (63) then the shifted field $u(x+\delta x,\tau)$ is also one. In other words, the system is *symmetric* under translations

$$u(x,\tau) \to u(x+\delta x,\tau)\,. \tag{67}$$

This symmetry operation shows itself as U(1) group action on the Fourier modes

$$\tilde{u}_k \to e^{ik\theta}\tilde{u}_k\,, \quad \text{where } \theta = 2\pi\delta x/L\,. \tag{68}$$

To be more explicit, let us construct a state space vector for this system. For simplicity, let us assume that $u(x,\tau)$ is real valued, hence $\tilde{u}_{-k} = \tilde{u}_k^*$, and 0^{th} Fourier mode has no dynamics and decoupled from the rest. Hence we can set $\tilde{u}_0 = 0$[1]. In this case, we can construct a real valued state vector

$$a = (b_1, c_1, b_2, c_2, \ldots, b_N, c_N)\,, \quad b_k = \operatorname{Re}\tilde{u}_k\,,\ c_k = \operatorname{Im}\tilde{u}_k\,. \tag{69}$$

In this state space, the continuous translation symmetry is represented by the SO(2) action

$$g(\theta) = \begin{pmatrix} R(\theta) & 0 & \cdots & 0 \\ 0 & R(2\theta) & \cdots & 0 \\ \vdots & \vdots & \ddots & \vdots \\ 0 & 0 & \cdots & R(m\theta) \end{pmatrix}, \tag{70}$$

where

$$R(n\theta) = \begin{pmatrix} \cos n\theta & -\sin n\theta \\ \sin n\theta & \cos n\theta \end{pmatrix} \tag{71}$$

are 2×2 rotation matrices. The groups U(1) and SO(2) are isomorphic, that is there is a one-to-one correspondence of their elements: Complex phases $e^{ik\theta}$ (68) act on the subspace of the k-th complex Fourier mode $\tilde{u}_k$ while rotation matrices $R(k\theta)$ (71) act on the real valued two-dimensional subspace $(b_k, c_k) = (\operatorname{Re}\tilde{u}_k, \operatorname{Im}\tilde{u}_k)$.

In the next section, we will set up the terminology for the properties of dynamical systems with continuous symmetries.

3.2 Equivariance under a continuous symmetry

A dynamical system is said to be *equivariant* under G if its evolution rule (7) commutes with $g(\theta)$

$$a(\tau) = g^{-1}(\theta) f^\tau(g(\theta)a)\,, \tag{72}$$

[1]For the discussion of translation symmetry, this assumption does not cause a loss of generality since $\tilde{u}_0$ is invariant under translation.

where $g(\theta)$ is a member of the symmetry group G, $\theta \in [0, 2\pi)$ is a real number that parametrizes the continuous symmetry action, which we assume to be compact, i.e. $g(2\pi) = \mathbf{1}$.

We are going to refer (72) as equivariance condition. For flows, (72) can be equivalently stated in the Eulerian description as

$$\dot{a} = g^{-1}(\theta) v(g(\theta) a) \,. \tag{73}$$

The equivariance property (72) implies that dynamics of state space points that are related by symmetry operations are equivalent, that is one can be obtained from the other by a symmetry operation. For a state vector a, the set of all such dynamically equvialent points

$$\mathcal{M}_{g(\theta)\, a} = \{ g(\theta)\, a \mid \theta \in [0, 2\pi) \} \tag{74}$$

is called the *group orbit* of a.

Assuming the action of $g(\theta)$ is smooth, we can define its infinitesimal action as

$$g(\delta\theta) = 1 + T\delta\theta \,, \tag{75}$$

where T is called the generator of infinitesimal transformations, or the Lie algebra element. We can express a finite transformation as a matrix exponential

$$g(\theta) = \lim_{n\to\infty} \left(1 + \frac{\theta}{n} T \right)^n = e^{\theta T} \,. \tag{76}$$

The direction, towards which an infinitesimal group action moves the state vector a

$$t(a) = Ta \tag{77}$$

is called *group tangent* of a.

We can now express the equivariance condition (73) for infinitesimal transformations by expanding (73) for small $\theta \to \delta\theta \ll 1$ to the first order

$$\begin{aligned} v(a) &= (1 - \delta\theta T) v((1 + \delta\theta T) a) \,, \\ &= (1 - \delta\theta T)(v(a) + A(a)\delta\theta T a) \,, \end{aligned}$$

keeping terms up to linear order in $\delta\theta$ and canceling common terms we obtain the infinitesimal equivariance condition as

$$A(a)t(a) - Tv(a) = 0 \tag{78}$$

With these definitions, we can now investigate some of the consequences of continuous symmetries, starting with the relative exact coherent structures and their stability.

3.2.1 Relative equilibria and relative periodic orbits

3.2.1.1 Relative equilibria

In Sect. 2.1.2, we introduced equilibria, periodic orbits and the notion of linear stability. Dynamical systems with continuous symmetries have relative equilibria and relative periodic orbits, which are equilibria and periodic orbits with additional dynamics in symmetry directions. A relative equilibrium's trajectory follows its group orbit:

$$a_{tw}(\tau) = g(\theta(\tau))\, a_{tw}(0) \,. \tag{79}$$

Using Lagrangian description of the flow (7) and expanding (79) for small times $\delta\tau$ we find

$$\begin{aligned} a_{tw}(0) + \int_0^{\delta\tau} v(a_{tw}(\tau'))\tau' &= e^{\delta\theta T} a_{tw}(0)\,, \\ a_{tw}(0) + v(a_{tw}(0))\delta\tau &= (1+\delta\theta T)\, a_{tw}(0)\,, \\ v(a_{tw}(0)) &= (\delta\theta/\delta\tau)\, t(a_{tw}(0)) \end{aligned} \tag{80}$$

that the velocity field and the group tangent are parallel for a relative equilibrium. Since we consider orthogonal (length preserving) group actions here, the proportionality constant $\delta\theta/\delta\tau$ in (80) is a constant along the orbit. Thus, we define the phase velocity of the relative equilibrium as

$$c = \lim_{\delta\tau\to 0} \frac{\delta\theta}{\delta\tau} \tag{81}$$

Multiplying the infinitesimal equivariance condition (78) with c for the relative equilibrium, we obtain

$$(A(a_{tw}) - cT)v(a_{tw}) = 0\,, \tag{82}$$

which tells us that the velocity field $v(a_{tw})$ is in the null space of $(A(a_{tw}) - cT)$. Later in this chapter, we are going to find that $(A(a_{tw}) - cT)$ is the stability matrix in the frame that moves with the relative equilibrium.

3.2.1.2 Relative periodic orbits

Second type of relative exact coherent structure is a relative periodic orbit whose trajectory intersects its group orbit after a finite time

$$a_{rpo}(T_p) = g(\theta_p)a_{rpo}(0)\,, \tag{83}$$

where T_p and θ_p respectively are period and phase shift of the relative periodic orbit. We determine the linear stability of a relative periodic orbit by rewriting (83) as

$$a_{rpo} = g(-\theta_p)f^T(a_{rpo})\,. \tag{84}$$

Expanding RHS to the linear order in perturbations to a_{rpo} as in (12), we obtain the Floquet matrix for a relative periodic orbit as

$$J_{rpo} = g(-\theta_p)J^{T_p}(a_{rpo})\,. \tag{85}$$

Spectrum of (85) determines the linear stability of the relative periodic orbit. State space points on the orbit (21) and group orbit (74) of a_{rpo} satisfy (84). Let us write (84) for a small perturbation $a_{rpo} + \epsilon v(a_{rpo})$ towards the orbit of a_{rpo} and expand to linear order

$$\begin{aligned} a_{rpo} + \epsilon v(a_{rpo}) &= g(-\theta_p)f^T(a_{rpo} + \epsilon v(a_{rpo}))\,, \\ a_{rpo} + \epsilon v(a_{rpo}) &= g(-\theta_p)f^T(a_{rpo}) + \epsilon J_{rpo} v(a_{rpo}) \\ v(a_{rpo}) &= J_{rpo} v(a_{rpo})\,. \end{aligned} \tag{86}$$

We found that $v(a_{rpo})$ is an eigenvector of J_{rpo} with unit eigenvalue. The same steps follow for a small perturbation $a_{rpo} + \epsilon t(a_{rpo})$, hence J_{rpo} has at least two marginal eigenvectors, namely $v(a_{rpo})$ and $t(a_{rpo})$.

3.3 Symmetry reduction

Symmetry reduction is a coordinate transformation $\hat{a} = S(a)$ such that

$$\begin{aligned} S(a) &= S(a') \quad \text{if} \quad a' = ga\,, \quad g \in G \\ S(a) &\neq S(a') \quad \text{if} \quad a' \neq ga\,, \quad g \in G \end{aligned} \tag{87}$$

i.e. reduced coordinates $\hat{a}$ are symmetry invariant. In such a representation, the relative equilibria and relative periodic orbits respectively become equilibria and periodic orbits, hence the theory of previous chapter becomes directly applicable. First question to ask is whether if such a transformation exist or not. For compact Lie groups, the answer is given by the Hilbert-Weyl theorem

Theorem 3.1 (Hilbert-Weyl) *For a compact group G there exist a finite G-invariant homogenous polynomial basis $\{u_1, u_2, \ldots, u_m\}$, $m \geq d$ such that any G-invariant polynomial can be written as a multinomial*

$$h(a) = p(u_1(a), u_2(a), \ldots, u_m(a)) \quad a \in \mathcal{M} \tag{88}$$

for proof of the Hilbert-Weyl theorem 3.1, see ref. [48]. What Hilbert-Weyl theorem tells us is that there exists a finite set of polynomials, with which all G-invariant information in $\mathcal{M}$ can be represented. Hence such polynomials can serve as a basis for a transformation like (87). What Hilbert-Weyl theorem does not tell us is how to find such polynomials. For low-dimensional systems, such as the Lorenz model (2), invariant polynomial methods are very useful and studied in detail, see for example [46]. For higher-dimensional systems, however, computation of the polynomial invariants becomes a harder task, and the computer algebra methods become impractical at dimensions larger than 12 [44]. We need a different strategy to attack this problem, if we want to apply it to turbulent flows with $\sim 10^5$-dimensional discretizations. The method of slices, which we introduce next, does the job.

3.3.1 Method of slices

Geometrical idea behind the method of slices is simple and intuitive: Since the action of the symmetry group at consideration is smooth, the group orbits (74) of the nearby points in the state space look alike. In mathematical terms, group orbits of infinitesimally close state space points are also infinitesimally close. Imagine such a *fiber bundle* of nearby group orbits, and a co-dimension 1 submanifold $\hat{\mathcal{M}} \in \mathcal{M}$ that is cut by these group orbits transversally as sketched in Figure 5 (a). Now if we take the intersections of group orbits with the slice as their "representatives", then we obtain a "local" symmetry reduced representation within the slice $\hat{\mathcal{M}}$.

Cartan [16] used method of slices in differential geometry. In dynamical systems literature, slicing techniques appears in many places under different names, with various applications. Therefore, we are going to list some examples from different sides of the early literature as an incomplete review. Works of Field, [41] Krupa, [70] and Ashwin and Melbourne, [7] are notable examples from the mathematics literature, where slicing methods were used to prove rigorous results. Fels and Olver [37, 38] compute symmetry invariant polynomials with the help of method of slices. In Hamiltonian dynamics, Haller and Mezić [54] used the method of slices, under the name "orbit projection map". Rowley and Marsden [96] used slicing methods in the reduced-order modeling of **[pde??]**s, and Beyn and Thümmler [9] used slicing methods to "freeze" spiral waves in the reaction-diffusion systems. Our formulation of the slice hyperplanes will closely follow that of ref. [96].

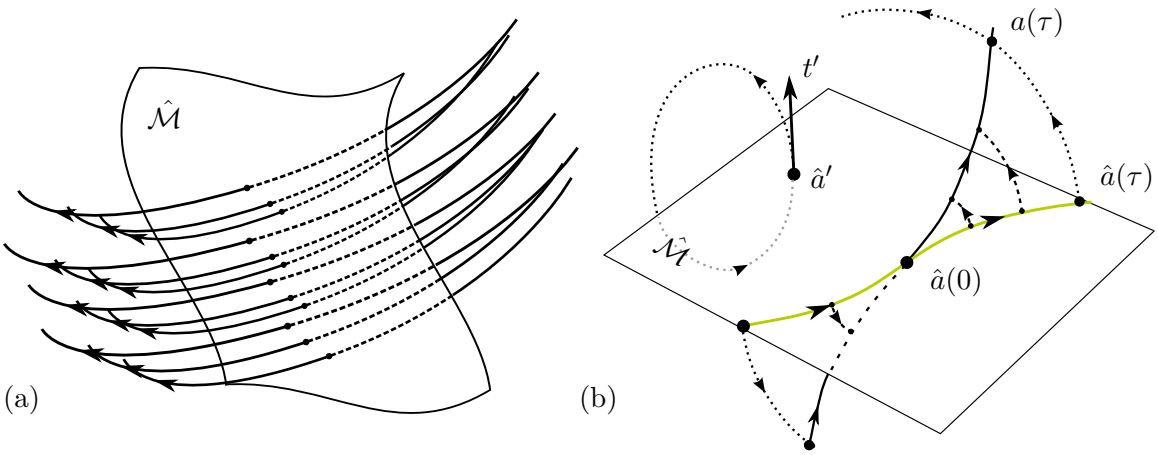

Figure 5: (a) A sketch of nearby group orbit segments and a slice that is cut by them transversally. (b) The slice hyperplane $\hat{\mathcal{M}}$, which passes through the template point $\hat{a}'$ and is normal to its group tangent t', intersects all group orbits (dotted lines) in an open neighborhood of $\hat{a}'$. The full state space trajectory $a(\tau)$ (solid black line) and the reduced state space trajectory $\hat{a}(\tau)$ (solid green line) belong to the same group orbit $\mathcal{M}_{g(\theta)a(\tau)}$ and are equivalent up to a 'moving frame' rotation by phase $\theta(\tau)$.

3.3.2 Slice hyperplane

We are now going to define a slice and formulate the symmetry reduced dynamics on it. The conceptual definition of the slice as a codimension-1 submanifold does not say much about its shape. The simplest choice one can think of is the set of points $\hat{a}$ satisfying the hyperplane condition

$$\langle \hat{a} - \hat{a}', t' \rangle = 0\,, \tag{89}$$

in an open neighbourhood

$$||\hat{a} - \hat{a}'|| < \alpha\,, \tag{90}$$

where $\hat{a}'$ and $t' = T\hat{a}'$ respectively are "slice template" and the "slice tangent", which together defines a hyperplane as the one sketched in Figure 5 (b). For orthogonal groups, $\langle a, Ta \rangle = 0$ by definition thus the first condition in (89) simplifies to

$$\langle \hat{a}, t' \rangle = 0\,. \tag{91}$$

Our textual definition of the slice relied on the assumption that the nearby group orbits are similar to each other, hence we can find a surface that is locally cut by them transversally. This notion of locality is included in the inequality condition of (89), where we ask for $\hat{a}$ to be in the α neighborhood of the template $\hat{a}'$ such that the transversality is not lost.

Full state space dynamics a(τ) can be brought to the slice hyperplane (89) by finding parameters $\theta(\tau)$ such that

$$\hat{a}(\tau) = g(-\theta(\tau))a(\tau) \tag{92}$$

satisfies the slice condition (89) as illustrated in Figure 5 (b). In order to find the dynamics

within the slice, we take a time derivative of (92)

$$\begin{aligned}\hat{v}(\hat{a}(\tau)) &= \frac{d\hat{a}(\tau)}{d\tau} \\ &= g(-\theta(\tau))v(a(\tau)) - \dot{\theta}(\tau)\, T\, g(-\theta(\tau))\, a(\tau)\,, \\ &= v(\hat{a}(\tau)) - \dot{\theta}(\tau)\, t(\hat{a}(\tau))\,, \end{aligned} \tag{93}$$

where the last step followed from the commutativity of the group action and the velocity field (73). Reduced velocity field $\hat{v}(\hat{a}(\tau))$ (93) satisfies the slice condition (91), thus we plug it into (91) to find the phase speed $\dot{\theta}$ as

$$\dot{\theta}(\tau) = \frac{\langle v(\hat{a}(\tau)), t' \rangle}{\langle t(\hat{a}(\tau)), t' \rangle}\,. \tag{94}$$

As it is of central importance for everything follows, we are going to rewrite (93) and (94) dropping the time arguments for clarity as

$$\hat{v}(\hat{a}) = v(\hat{a}) - \dot{\theta}(\hat{a}) t(\hat{a})\,, \tag{95}$$

$$\dot{\theta}(\hat{a}) = \langle v(\hat{a}), t' \rangle / \langle t(\hat{a}), t' \rangle\,. \tag{96}$$

Equations (95) and (96) have a nice geometrical interpretation: In (95) we subtract from the full state space velocity $v(\hat{a})$, its component in the direction towards the group tangent $t(\hat{a})$; and the proportionality constant $\dot{\theta}(\hat{a})$ is found in (96) by projecting the full state space velocity onto the group tangent direction and dividing by a normalization factor.

The locality of the slice hyperplane also becomes apparent from the phase velocity (96), which becomes singular if the inner product on its denominator is 0. The vanishing inner product $\langle t(\hat{a}), t' \rangle$ exactly corresponds to the "loss of transversality", that is if the group tangent at a point does not have a component perpendicular to the slice hyperplane, then the corresponding group orbit cannot pierce it. Froehlich and Cvitanović [43] defined such codimension-2 set of points $\hat{a}^*$ as the *slice border*, which satisfy

$$\langle t(\hat{a}^*), t' \rangle = 0\,. \tag{97}$$

Froehlich and Cvitanović [43] studied what happens to the nearby reduced trajectories in detail. The slice border (97) rigorously sets the border of a slice and if the trajectories cross it, one has discontinuities.

Let us take a break and remember why we were concerned about the continuous symmetries in the first place. Our purpose in this thesis is to understand the chaotic dynamics of nonlinear **[pde??]**s, by charting their infinite-dimensional state spaces. Our strategy was to understand exact coherent structures in such systems and their dynamical relations. However, the presence of continuous symmetries in these problems brought a huge complication due to the fact that the state space had infinite amount of redundant data, which we would like to get rid off. Furthermore, the relative invariant solutions, which we introduced in Sect. 3.2.1, had dimensions larger than their regular counterparts, which would make their study much more challenging, if not impossible. For this reason, we attempted to transform the dynamics to a symmetry-invariant representation, where we would quotient out the symmetry copies. Finally, we ended up with a reduced description, which would only be applicable in an open neighborhood of the state space, border of which is set by (97). A strategy to overcome this difficulty was suggested in ref. [43] as using multiple slices,

glued together to cover the strange attractor avoiding the border of each slice. This idea was applied to the complex Lorenz equations in ref. [23] and to the pipe flow in ref. [115]. However, finding such intelligent templates is never straightforward and requires a careful investigation of each problem at hand. In the course of this thesis study, we asked a different question: Can we define a single slice hyperplane such that its border never visited by the generic dynamics? The answer turned out to be affirmative for the SO(2) symmetry [14].

3.3.3 First Fourier mode slice

In previous section, we introduced method of slices for a general continuous symmetry. Let us now focus on the specific problem we have: We would like to reduce the SO(2) symmetry that we have as the result of studying a nonlinear **[pde??]** (63) under periodic boundary condition (65). Notice that in the real-valued state space representation (69), the projections of the group orbits onto the first Fourier mode subspace (b_1, c_1) are circles. Therefore, we can think of transforming to polar coordinates in this subspace to quotient out the SO(2) symmetry by the following transformation

$$\hat{a}(\tau) = g(-\theta(\tau))\, a(\tau) \quad \theta(\tau) = \arg(b_1(\tau) + i\, c_1(\tau)) \tag{98}$$

as depicted on Figure 6.

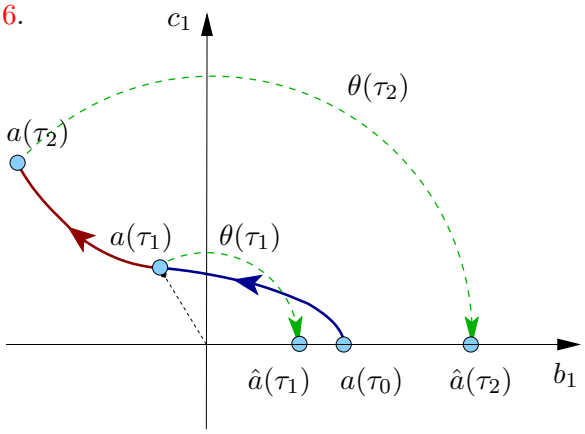

Figure 6: A sketch of the state space trajectory $a(t)$ (blue and red) projected onto the first Fourier mode subspace (b_1, c_1), and the rotation phases $\theta(\tau_{1,2})$ (98) at times τ_1 and τ_2.

We are now going to cast this into slicing language. For that, we first need the generator of infinitesimal SO(2) transformations, which for the representation (70) reads

$$T = \begin{pmatrix} T_1 & 0 & \cdots & 0 \\ 0 & T_2 & \cdots & 0 \\ \vdots & \vdots & \ddots & \vdots \\ 0 & 0 & \cdots & T_m \end{pmatrix}, \text{ where } T_k = \begin{pmatrix} 0 & -1 \\ 1 & 0 \end{pmatrix}. \tag{99}$$

If we now choose a slice template as

$$\hat{a}' = (1, 0, 0, \ldots, 0)^T, \tag{100}$$

we find the corresponding template tangent as

$$t' = (0, 1, 0, \ldots, 0)^T, \tag{101}$$

these render the hyperplane condition (91) for state vectors (69) as $c_1 = 0$. Moreover, the slice border condition (97) for this choice becomes $b_1 = 0$. As can be seen from Figure 6 each circular group orbit in the (b_1, c_1) plane would cut $c_1 = 0$ line twice and the slice border $b_1 = 0$ lies between the two intersections. Therefore, we need to pick one side of b_1 line in order to uniquely define our slice; the choice that agrees with the phase fixing transformation of (98) is $b_1 > 0$. We can now express the dynamics directly within the first Fourier mode slice. Expressing (96) for the slice template (100) and plugging into (95) we obtain

$$\hat{v}(\hat{a}) = v(\hat{a}) - \frac{\dot{c}_1}{\hat{b}_1} t(\hat{a}) \,, \tag{102}$$

where $\dot{c}_1$ and $\hat{b}_1$ respectively denotes the second element of $v(\hat{a})$ and first element of $\hat{a}$. We see that the reduced dynamics (102) is singular when $\hat{b}_1 = 0$. We regularize this by defining the *slice time* as

$$d\hat{\tau} = d\tau / \hat{b}_1 \,, \tag{103}$$

which regularizes this singularity as the reduced dynamics with respect to the slice time is defined by

$$d\hat{a}/d\hat{\tau} = \hat{b}_1 v(\hat{a}) - \dot{c}_1(\hat{a})\, t(\hat{a}) \,, \tag{104}$$

$$d\theta(\hat{a})/d\hat{\tau} = \dot{c}_1(\hat{a}) \,. \tag{105}$$

We call this method *first Fourier mode slice*, since the effect of this transformation is fixing the phase of the first Fourier mode to 0 as in (98).

The first Fourier mode slice is a valid SO(2) symmetry reduction method as long as the amplitude of the first Fourier mode is non-zero. Moreover, if the first Fourier mode amplitude is small, then the flow can be regularized by adapting the time steps as (103). As we shall demonstrate in the applications of the following chapters, we found that this method works for state space regions of interest.

3.3.4 Stability in the symmetry-reduced state space

3.3.4.1 Stability of relative equilibria

Since the relative equilibria become equilibria after symmetry reduction, we treat them as equilibria in the slice, and compute the corresponding stability matrix similar to (10) by computing partial derivatives of the reduced velocity (95) as

$$\begin{aligned} \frac{\partial \hat{v}(\hat{a})_i}{\partial \hat{a}_j} &= \frac{\partial}{\partial \hat{a}_j} \left\{ v(\hat{a})_i - \frac{\langle v(\hat{a}), t' \rangle}{\langle t(\hat{a}), t' \rangle} t(\hat{a})_i \right\} \,, \\ \hat{A}(\hat{a})_{ij} &= A(\hat{a})_{ij} - \frac{t(\hat{a})_i \left\{ (\langle t(\hat{a}), t' \rangle A(\hat{a})^T - \langle v(\hat{a}), t' \rangle T^T) t' \right\}_j}{\langle t(\hat{a}), t' \rangle^2} \\ &\quad - \frac{\langle v(\hat{a}), t' \rangle}{\langle t(\hat{a}), t' \rangle} T_{ij} \,. \end{aligned} \tag{106}$$

We can express this in the matrix notation as

$$\begin{aligned} \hat{A}(\hat{a}) &= A(\hat{a}) - \frac{t(\hat{a}) \left[\left(\langle t(\hat{a}), t' \rangle A(\hat{a})^T - \langle v(\hat{a}), t' \rangle T^T \right) t' \right]^T}{\langle t(\hat{a}), t' \rangle^2} \\ &\quad - \frac{\langle v(\hat{a}), t' \rangle}{\langle t(\hat{a}), t' \rangle} T \,. \end{aligned} \tag{107}$$

We stated the reduced velocity gradient matrix (107) for an arbitrary point and a slice template and this is the formula one should indeed use when applying the first Fourier mode slice. However, it is informative to check what happens when (107) is expressed using a relative equilibrium itself as the template. Since for a relative equilibrium we have $v(a_{tw}) = c\,t(a_{tw})$, when we substitute $\hat{a}' = a_{tw}$ in (107), expression in the brackets in the second term becomes (82), hence vanishes. We then obtain a much simpler form

$$\hat{A}(a_{tw})|_{\hat{a}'=a_{tw}} = A(a_{tw}) - cT\,, \tag{108}$$

which we know from (82) to have $v(a_{tw})$ as an eigenvector with zero eigenvalue, as it should.

3.3.4.2 Stability of relative periodic orbits

We have shown in Sect. 3.2.1 that the Floquet matrix for a relative periodic orbit is $J_{rpo} = g(-\theta_p)J^T(a_{rpo})$. We are now going to show that its eigenvalues are invariant in a symmetry reduced representation, except the marginal one corresponding to the continuous symmetry direction. We will present this result in a representation invariant way, since the topological invariance of the Floquet multipliers is essential for periodic orbit theory.

In a symmetry-invariant representation obtained by a transformation like (87), a relative periodic orbit becomes a periodic orbit since both initial and final points on its orbit is mapped to the same point

$$\hat{a}_{rpo} = S(g(\theta)a_{rpo})\,, \quad \forall\theta \in [0,\, 2\pi)\,. \tag{109}$$

Now if we consider a small perturbation δa to the relative periodic orbit in the full state space, and expand (83) to the linear order, we obtain

$$\begin{aligned} a_{rpo} + \delta a(T_p) &= g(-\theta_p)f^{T_p}(a_{rpo} + \delta a(0))\,, \\ &= g(-\theta_p)f^{T_p}(a_{rpo}) + J_{rpo}\,\delta a(0)\,, \end{aligned} \tag{110}$$

hence

$$\delta a(T_p) = J_{rpo}\,\delta a(0)\,. \tag{111}$$

If we transform $a_{rpo} + \delta a(T_p)$ to the symmetry reduced coordinates, we obtain

$$\begin{aligned} \hat{a}_{rpo} + \delta\hat{a}(T_p) &= S(\hat{a}_{rpo} + \delta a(T_p))\,, \\ &= \hat{a}_{rpo} + \Gamma(a)J_{rpo}\delta a(0)\,, \end{aligned} \tag{112}$$

where $\Gamma_{ij}(a) = \partial S_i(a)/\partial a_j$ is the Jacobian of the symmetry reducing transformation. Therefore, if $\delta a(0)$ is an eigenvector $V_i \neq \text{const.}\, t(a_{rpo})$ of J_{rpo} with eigenvalue Λ_i, then the symmetry reduced relative periodic orbit would also have the same Floquet multiplier, with corresponding eigenvector $\hat{V}_i = \Gamma V_i$. From the definition of the symmetry reduction (87), we must have $\Gamma(a)t(a) = 0$, hence this marginal eigenvector disappears after symmetry reduction.

The periodic orbit formulas (61) and (62) both have $\left|\det\left(\mathbf{1} - M_p^r\right)\right|$ terms, which can be expressed in terms of Floquet multipliers. Therefore, the topological invariance of the Floquet multipliers is crucial for these formulas to make sense. In this section, we have confirmed that the non-marginal Floquet multipliers of relative periodic orbits are preserved in any symmetry reduced representation; hence we can use them to treat the relative periodic orbits as if they are periodic orbits in the symmetry-reduced state space and apply periodic orbit theory to these systems.

3.3.5 The first Fourier mode slice in higher spatial dimensions

We introduced the method of slices in a general setting and then made a specific choice of slice for the SO(2) symmetry, whose effect was essentially to fix the phase of the first Fourier mode to 0 as shown in Figure 6. We can state this phase fixing transformation for Fourier modes (66) as

$$\hat{u}_k(\tau) = e^{-ik\phi_1(\tau)}\tilde{u}_k(\tau)\,, \tag{113}$$

where $\hat{u}_k$ is the kth symmetry reduced Fourier mode and ϕ_1 is the phase of the first Fourier mode. It is straightforward to check that $\hat{u}_k$ is invariant under (68) and $\hat{u}_1$ is purely real.

We could have also formulated the first Fourier mode slice in the physical space without transforming to the Fourier representation. Notice that the slice template (100) and template tangent (101) correspond to the flow fields $2\cos(2\pi x/L)$ and $2\sin(2\pi x/L)$. Thus, for the flow field $u(x,\tau)$, we can find the slice fixing phase as

$$\phi_1(\tau) = \arg(\langle u(x,\tau),\, \cos(2\pi x/L)\rangle + i\langle u(x,\tau),\, \sin(2\pi x/L)\rangle)\,. \tag{114}$$

Thus the symmetry reduced field $\hat{u}(x,\tau)$ is given by

$$\hat{u}(x,\tau) = u\left(x - \frac{L\phi_1(\tau)}{2\pi}, \tau\right)\,. \tag{115}$$

The physical space formulation can be convenient if the data is not represented as a Fourier expansion. In addition, it will be helpful to understand the generalization of the first Fourier mode slice for vector fields.

3.3.5.1 Scalar field in two dimensions

Let us now consider a scalar field $u(\mathbf{x},\tau)$ defined over a two-dimensional space $\mathbf{x} = (x,y)$ with dynamics equvariant under translations

$$g(\ell_x,\ell_y)u(x,y;\tau) = u(x+\ell_x, y+\ell_y;\tau). \tag{116}$$

If periodic boundary conditions

$$u(x,y;\tau) = u(x+L_x,y;\tau)\,, \quad u(x,y;\tau) = u(x,y+L_y;\tau) \tag{117}$$

are imposed, then it is natural to express $u(\mathbf{x},\tau)$ in a Fourier expansion

$$u(\mathbf{x},\tau) = \sum_{kl} \tilde{u}_{kl}(\tau)e^{i(q_k x + q_l y)}\,, \quad \text{where } q_k = 2\pi k/L_x\,,\ q_l = 2\pi k/L_y\,. \tag{118}$$

The symmetry action (116) on the Fourier modes (118) is

$$g(\ell_x,\ell_y)\tilde{u}_{kl} = e^{i(k\theta_x + l\theta_y)}\tilde{u}_{kl}\,, \quad \text{where } \theta_{x,y} = 2\pi\ell_{x,y}/L_{x,y}\,. \tag{119}$$

Thus we can write the phase fixing condition analogous to (113) for Fourier modes $\tilde{u}_{kl}$ as

$$\hat{u}_{kl}(\tau) = e^{-i(k\,\phi_{10}(\tau) + l\,\phi_{01}(\tau))}\tilde{u}_{kl}(\tau)\,, \tag{120}$$

where $\hat{u}_{kl}$ is the klth symmetry reduced Fourier mode and ϕ_{kl} is the phase of the Fourier mode $\tilde{u}_{kl}$.

We could have also found the slice fixing phases ϕ_{10} and ϕ_{01} from flow fields as

$$\begin{aligned}\phi_{10}(\tau) &= \arg\left(\langle u(\mathbf{x},\tau),\cos(2\pi x/L)\rangle + i\langle u(\mathbf{x},\tau),\sin(2\pi x/L)\rangle\right),\\ \phi_{01}(\tau) &= \arg\left(\langle u(\mathbf{x},\tau),\cos(2\pi y/L)\rangle + i\langle u(\mathbf{x},\tau),\sin(2\pi y/L)\rangle\right).\end{aligned} \tag{121}$$

Then the symmetry reduced flow field is

$$\hat{u}(x,y;t) = u\left(x - L_x\frac{\phi_{10}(\tau)}{2\pi}, y - L_y\frac{\phi_{01}(\tau)}{2\pi};\tau\right). \tag{122}$$

Finally, in the two dimensions, we have two conditions for the slice border

$$\begin{aligned}|\tilde{u}_{10}| &= |\langle u(\mathbf{x},\tau),\cos(2\pi x/L)\rangle + i\langle u(\mathbf{x},\tau),\sin(2\pi x/L)\rangle| = 0,\\ |\tilde{u}_{01}| &= |\langle u(\mathbf{x},\tau),\cos(2\pi y/L)\rangle + i\langle u(\mathbf{x},\tau),\sin(2\pi y/L)\rangle| = 0.\end{aligned} \tag{123}$$

Thus the slice time can be defined as

$$d\hat{\tau} = \frac{d\tau}{|\tilde{u}_{10}||\tilde{u}_{01}|}. \tag{124}$$

3.3.5.2 Vector field in two dimensions

Generalization of the first Fourier mode slice for a two-dimensional scalar field on a periodic box was straightforward. We shall now take one step further and consider a vector field

$$\mathbf{u}(\mathbf{x},t) = u(x,y;t)\,\hat{\mathbf{x}} + v(x,y;t)\,\hat{\mathbf{y}} \tag{125}$$

equivariant under

$$g(\ell_x,\ell_y)\mathbf{u}(x,y;\tau) = \mathbf{u}(x+\ell_x, y+\ell_y;\tau), \tag{126}$$

and satisfying the periodic boundary conditions

$$\mathbf{u}(x,y;\tau) = \mathbf{u}(x+L_x,y;\tau), \quad \mathbf{u}(x,y;\tau) = \mathbf{u}(x,y+L_y;\tau). \tag{127}$$

When we write the Fourier expansion for $\mathbf{u}(x,y;\tau)$ as

$$\mathbf{u}(\mathbf{x},t) = \sum_{kl}[\tilde{u}_{kl}(\tau)\hat{\mathbf{x}} + \tilde{v}_{kl}(\tau)\hat{\mathbf{y}}]e^{i(q_k x + q_l y)}, \quad \text{where } q_k = 2\pi k/L_x,\ q_l = 2\pi k/L_y \tag{128}$$

we see that we now have four modes (two for each continuous symmetry direction), namely $\tilde{u}_{01}, \tilde{u}_{10}, \tilde{v}_{01}, \tilde{v}_{10}$ that we can fix the phase of, in order to obtain a symmetry reduced representation. For instance, we can define a symmetry reducing transformation as

$$\hat{\mathbf{u}}_{kl}(\tau) = e^{-i(k\,\phi_{u,10}(\tau) + l\,\phi_{v,01}(\tau))}\tilde{\mathbf{u}}_{kl}(\tau), \tag{129}$$

where $\phi_{u(v),kl}$ is the phase of the Fourier mode $\tilde{u}(\tilde{v})_{kl}$. In fact, our choices are infinitely many since we are allowed to express the flow field (125) as

$$\mathbf{u}(\mathbf{x},t) = u'(x,y;t)\,\hat{\mathbf{x}}' + v'(x,y;t)\,\hat{\mathbf{y}}', \tag{130}$$

where $\hat{\mathbf{x}}'$ and $\hat{\mathbf{y}}'$ are linearly independent (not necessarily orthogonal) unit vectors that span the 2D physical space. We can express the general first Fourier mode slice templates for the two-dimensional vector field as

$$\begin{aligned}\mathbf{u'}_x(\mathbf{x}) &= \mathbf{f}\cos(2\pi x/L_x),\\ \mathbf{u'}_y(\mathbf{x}) &= \mathbf{g}\cos(2\pi y/L_y),\end{aligned} \tag{131}$$

where $\mathbf{f}$ and $\mathbf{g}$ are two-dimensional vectors that can be same or different. With (131), we can express the slice-fixing phases as inner products

$$\begin{aligned}\phi_{10}(\tau) &= \arg\left(\langle \mathbf{u}(\mathbf{x},\tau), \mathbf{u'}_x(\mathbf{x})\rangle + i\langle \mathbf{u}(\mathbf{x},\tau), g(L_x/4,0)\,\mathbf{u'}_x(\mathbf{x})\rangle\right)\,,\\ \phi_{01}(\tau) &= \arg\left(\langle \mathbf{u}(\mathbf{x},\tau), \mathbf{u'}_y(\mathbf{x})\rangle + i\langle \mathbf{u}(\mathbf{x},\tau), g(0,L_y/4)\,\mathbf{u'}_y(\mathbf{x})\rangle\right)\end{aligned} \tag{132}$$

and the symmetry reducing transformation as

$$\hat{\mathbf{u}}(x,y;t) = \mathbf{u}\left(x - L_x\frac{\phi_{10}(\tau)}{2\pi}, y - L_y\frac{\phi_{01}(\tau)}{2\pi};\tau\right)\,. \tag{133}$$

The choice for $\mathbf{f}$ and $\mathbf{g}$ in (131) should be specific for the problem at hand such that the slice border conditions

$$\begin{aligned}|\tilde{\mathbf{u}}_{10}| &= \left|\langle \mathbf{u}(\mathbf{x},\tau), \mathbf{u'}_x(\mathbf{x})\rangle + i\langle \mathbf{u}(\mathbf{x},\tau), g(L_x/4,0)\,\mathbf{u'}_x(\mathbf{x})\rangle\right| = 0\,,\\ |\tilde{\mathbf{u}}_{01}| &= \left|\langle \mathbf{u}(\mathbf{x},\tau), \mathbf{u'}_y(\mathbf{x})\rangle + i\langle \mathbf{u}(\mathbf{x},\tau), g(0,L_y/4)\,\mathbf{u'}_y(\mathbf{x})\rangle\right| = 0\,.\end{aligned} \tag{134}$$

are avoided. Finally, we can define the slice time for this case as

$$d\hat{\tau} = \frac{d\tau}{|\tilde{\mathbf{u}}_{10}||\tilde{\mathbf{u}}_{01}|}\,. \tag{135}$$

3.3.5.3 Vector field in three dimensions

Final case we are going to consider is a three-dimensional vector field $\mathbf{u}(\mathbf{x},\tau)$ with dynamics equivariant under

$$g(\ell_x,\ell_y)\mathbf{u}(x,y,z;\tau) = \mathbf{u}(x+\ell_x, y+\ell_y, z;\tau)\,, \tag{136}$$

satisfying periodic boundary conditions

$$\mathbf{u}(x,y,z;\tau) = \mathbf{u}(x+L_x,y,z;\tau)\,, \quad \mathbf{u}(x,y,z;\tau) = \mathbf{u}(x,y+L_y,z;\tau)\,, \tag{137}$$

and some Dirichlet boundary condition

$$\mathbf{u}(\mathbf{x};\tau)|_{z\in\partial\Omega} = \mathbf{d}(\mathbf{x})\,. \tag{138}$$

In this case, the slice templates that we are allowed to chose are in the following form

$$\begin{aligned}\mathbf{u'}_x(\mathbf{x}) &= \mathbf{f}(z)\cos(2\pi x/L_x)\,,\\ \mathbf{u'}_y(\mathbf{x}) &= \mathbf{g}(z)\cos(2\pi y/L_y)\,,\end{aligned} \tag{139}$$

where $\mathbf{f}(z)$ and $\mathbf{g}(z)$ are three dimensional vector functions of z. The rest of the formulation is the same with that of the two-dimensional vector field case, and the functions $\mathbf{f}(z)$ and $\mathbf{g}(z)$ should again be picked in order to avoid slice borders (134).

Notice that the case we consider here covers axially periodic pipe flow and stream-wise and span-wise periodic plane Couette flow. In pipe flow (see Figure 4 (a)), periodic directions are z and θ and the Dirichlet boundary condition (138) is $\mathbf{u}_{r=R} = 0$, where R is the pipe radius. Similarly, in plane Couette flow(see Figure 4 (b)), the periodic directions are x and z and the Dirichlet boundary condition (138) is $\mathbf{u}_{y=\pm D/2} = \pm v$, where D is the distance between walls.

3.4 Conclusions

In this chapter, we introduced continuous translation symmetry that frequently appears in the studies of spatiotemporal chaos, its implications, and symmetry reduction by method of slices. In Sect. 3.3.3 we presented the main contribution of this thesis: first Fourier mode slice method for reducing the SO(2) symmetry for Fourier expansion of a field in one space dimension. The main idea was to fix the phase of the first Fourier mode in order to reduce the SO(2) symmetry and to regularize the singularity of the reduced flow by defining a rescaled slice time. Finally, in Sect. 3.3.5, we presented different formulations of the first Fourier mode slice in terms of flow fields, and its generalizations to the higher dimensional settings. In the rest of this thesis, we are going to present three applications of the first Fourier mode slice in problems with increasing difficulty.

CHAPTER IV

THE TWO-MODES SYSTEM

We are now going to apply the theory we presented to a simple problem that has the symmetry structure described in the previous chapter with only four dimensions, which is just enough to have chaotic dynamics. The work presented in this chapter is published in ref. [13].

4.1 Two-modes SO(2)-equivariant flow

Dangelmayr, [27] Armbruster, Guckenheimer and Holmes, [2] Jones and Proctor, [64] and Porter and Knobloch [88] (for more detail, see Sect. XX.1 in Golubitsky *et al.* [48]) have investigated bifurcations in 1:2 resonance **[ode??]** normal form models to third order in the amplitudes. Here, we use this model as a starting point from which we derive what may be one of the simplest chaotic systems with continuous symmetry. We refer to this as the two-modes system:

$$\begin{aligned} \dot{z}_1 &= (\mu_1 - i\,e_1)\,z_1 + a_1\,z_1|z_1|^2 + b_1\,z_1|z_2|^2 + c_1\,\overline{z}_1\,z_2 \\ \dot{z}_2 &= (\mu_2 - i\,e_2)\,z_2 + a_2\,z_2|z_1|^2 + b_2\,z_2|z_2|^2 + c_2\,z_1^2\,, \end{aligned} \tag{140}$$

where z_1 and z_2 are complex and all parameters are real-valued. The parameters $\{e_1, e_2\}$ break the reflectional symmetry of the O(2)-equivariant normal form studied by Dangelmayr [27] leading to an SO(2)-equivariant system. This complex two mode system can be expressed as a 4-dimensional system of real-valued first order **[ode??]**s by substituting $z_1 = x_1 + i\,y_1$, $z_2 = x_2 + i\,y_2$, so that

$$\begin{aligned} \dot{x}_1 &= (\mu_1 + a_1 r_1^2 + b_1 r_2^2 + c_1 x_2)x_1 + c_1 y_1 y_2 + e_1 y_1\,, \\ \dot{y}_1 &= (\mu_1 + a_1 r_1^2 + b_1 r_2^2 - c_1 x_2)y_1 + c_1 x_1 y_2 - e_1 x_1\,, \\ \dot{x}_2 &= (\mu_2 + a_2 r_1^2 + b_2 r_2^2)x_2 + c_2(x_1^2 - y_1^2) + e_2 y_2\,, \\ \dot{y}_2 &= (\mu_2 + a_2 r_1^2 + b_2 r_2^2)y_2 + 2c_2 x_1 y_1 - e_2 x_2\,, \\ &\quad \text{where } r_1^2 = x_1^2 + y_1^2\,, \quad r_2^2 = x_2^2 + y_2^2\,. \end{aligned} \tag{141}$$

The large number of parameters $(\mu_1, \mu_2, a_1, a_2, b_1, b_2, c_1, c_2, e_1, e_2)$ in this system makes full exploration of the parameter space impractical. Following in the tradition of Lorenz, [74] Hénon, [55] and Rössler, [95] we have tried various choices of parameters until settling on the following set of values, which we will use in all numerical calculations presented here:

μ_1	μ_2	e_1	e_2	a_1	a_2	b_1	b_2	c_1	c_2
-2.8	1	0	1	-1	-2.66	0	0	-7.75	1

(142)

This choice of parameters is far from the bifurcation values studied by previous authors, [2, 27, 64, 88] so that the model has no physical interpretation. However, these parameters yield chaotic dynamics, making the two-mode system a convenient minimal model for the study of chaos in the presence of a continuous symmetry: It is a 4-dimensional SO(2)-equivariant model, whose symmetry-reduced dynamics are chaotic and take place on a three-dimensional manifold.

It can be confirmed by inspection that eqs. (140) are equivariant under the U(1) transformation

$$(z_1, z_2) \to (e^{i\phi} z_1, e^{i2\phi} z_2)\,. \tag{143}$$

In the real representation (141), the U(1) group action (143) on a state space point a is given by the SO(2) action (70) with the Lie algebra element (99) both truncated at $m = 2$. One can easily check that the real two-modes system (141) satisfies the equivariance condition (78).

From (140), it is obvious that the equilibrium point $(z_1, z_2) = (0, 0)$ is an invariant subspace and that $z_1 = 0$, $z_2 \neq 0$ is a 2-dimensional flow-invariant subspace

$$\dot{z}_1 = 0\,, \qquad \dot{z}_2 = (\mu_2 - i\, e_2 + b_2 |z_2|^2)\, z_2 \tag{144}$$

with a single circular relative equilibrium of radius $r_2 = \| z_2 \| = \sqrt{-\mu_2/b_2}$ with phase velocity $c = -e_2/2$. At the origin the stability matrix A commutes with T, and so, can be block-diagonalized into two $[2 \times 2]$ matrices. The eigenvalues of A at $(0, 0, 0, 0)$ are $\lambda_{1,2} = \mu_1$ with multiplicity 2 and $\lambda_{3,4} = \mu_2 \pm i e_2$. In the (x_1, y_1, x_2, y_2) coordinates, the eigenvectors with eigenvalues λ_1 and λ_2 are $(1, 0, 0, 0)$ and $(0, 1, 0, 0)$ and the eigenvectors with eigenvalues λ_3 and λ_4 are $(0, 0, 1, \pm i)$.

In contrast, $z_2 = 0$ is not, in general, a flow-invariant subspace since the dynamics

$$\dot{z}_1 = (\mu_1 - i\, e_1)\, z_1 + a_1\, z_1 |z_1|^2\,, \qquad \dot{z}_2 = c_2\, z_1^2\,.$$

take the flow out of the $z_2 = 0$ plane.

4.1.1 Invariant polynomial bases

Before applying the first Fourier mode slice, we briefly discuss the symmetry reduction of the two-modes system using invariant polynomials. While representations of our model in terms of invariant polynomials and polar coordinates are useful for cross-checking our calculations in the full state space $a^\top = (x_1, x_2, y_1, y_2)$, their construction requires a bit of algebra even for this simple 4-dimensional flow. For very high-dimensional flows, such as Kuramoto-Sivashinsky and Navier-Stokes flows, we do not know how to carry out such constructions. As discussed in refs. [2, 27, 88], for the two-modes system, it is easy to construct a set of four real-valued SO(2) invariant polynomials

$$\begin{aligned} u &= z_1 \overline{z}_1\,, \quad v = z_2 \overline{z}_2 \\ w &= z_1^2 \overline{z}_2 + \overline{z}_1^2 z_2\,, \quad q = (z_1^2 \overline{z}_2 - \overline{z}_1^2 z_2)/i\,. \end{aligned} \tag{145}$$

The polynomials $[u, v, w, q]$ are linearly independent, but related through one syzygy,

$$w^2 + q^2 - 4\, u^2 v = 0 \tag{146}$$

that confines the dynamics to a 3-dimensional manifold $\hat{\mathcal{M}} = \mathcal{M}/\mathrm{SO}(2)$, which is a symmetry-invariant representation of the 4-dimensional SO(2) equivariant dynamics. We call this the reduced state space. By construction, $u \geq 0$, $v \geq 0$, but w and q can be of either sign. That is explicit if we express z_1 and z_2 in polar coordinates ($z_1 = |u|^{1/2} e^{i\phi_1}$, $z_2 = |v|^{1/2} e^{i\phi_2}$), so that w and q take the form

$$\begin{aligned} w &= 2\,\mathrm{Re}\,(z_1^2 \overline{z}_2) = 2\, u |v|^{1/2} \cos\psi \\ q &= 2\,\mathrm{Im}\,(z_1^2 \overline{z}_2) = 2\, u |v|^{1/2} \sin\psi\,, \end{aligned} \tag{147}$$

where $\psi = 2\phi_1 - \phi_2$.

The dynamical equations for $[u, v, w, q]$ follow from the chain rule, which yields

$$\begin{aligned} \dot{u} &= \overline{z}_1\dot{z}_1 + z_1\dot{\overline{z}}_1\,, \qquad \dot{v} = \overline{z}_2\dot{z}_2 + z_2\dot{\overline{z}}_2 \\ \dot{w} &= 2\,\overline{z}_2 z_1\dot{z}_1 + 2\,z_2\overline{z}_1\dot{\overline{z}}_1 + z_1^2\dot{\overline{z}}_2 + \overline{z}_1^2\dot{z}_2 \\ \dot{q} &= (2\,\overline{z}_2 z_1\dot{z}_1 - 2\,z_2\overline{z}_1\dot{\overline{z}}_1 + z_1^2\dot{\overline{z}}_2 - \overline{z}_1^2\dot{z}_2)/i \end{aligned} \tag{148}$$

Substituting (140) into (148), we obtain a set of four SO(2)-invariant equations,

$$\begin{aligned} \dot{u} &= 2\,\mu_1\,u + 2\,a_1\,u^2 + 2\,b_1\,u\,v + c_1\,w \\ \dot{v} &= 2\,\mu_2\,v + 2\,a_2\,u\,v + 2\,b_2\,v^2 + c_2\,w \\ \dot{w} &= (2\,\mu_1 + \mu_2)\,w + (2a_1 + a_2)\,u\,w + (2b_1 + b_2)\,v\,w \\ &\quad + 4c_1\,u\,v + 2c_2\,u^2 + (2e_1 - e_2)\,q \\ \dot{q} &= (2\mu_1 + \mu_2)\,q + (2a_1 + a_2)\,u\,q \\ &\quad + (2b_1 + b_2)\,v\,q - (2e_1 - e_2)\,w\,. \end{aligned} \tag{149}$$

Note that the O(2)-symmetry breaking parameters $\{e_1, e_2\}$ of the Dangelmayr normal form system [27] appear only in the relative phase combination $(2e_1 - e_2)$, so one of the two can be set to zero without loss of generality. This consideration motivated our choice of $e_1 = 0$ in (142). Using the syzygy (146), we can eliminate q from (149) to get

$$\begin{aligned} \dot{u} &= 2\,\mu_1\,u + 2\,a_1\,u^2 + 2\,b_1\,u\,v + c_1\,w \\ \dot{v} &= 2\,\mu_2\,v + 2\,a_2\,u\,v + 2\,b_2\,v^2 + c_2\,w \\ \dot{w} &= (2\,\mu_1 + \mu_2)\,w + (2a_1 + a_2)\,u\,w + (2b_1 + b_2)\,v\,w \\ &\quad + 4c_1\,u\,v + 2c_2\,u^2 + (2e_1 - e_2)(4u^2v - w^2)^{1/2} \end{aligned} \tag{150}$$

This invariant basis can be used either to investigate the dynamics directly or to visualize solutions computed in the full equivariant basis (140).

4.1.2 Equilibria of the symmetry-reduced dynamics

The first step in elucidating the geometry of attracting sets is the determination of their equilibria. We shall now show that the problem of determining the equilibria of the symmetry-reduced two-modes (149) system can be reduced to finding the real roots of a multinomial expression. First, we define

$$A_1 = \mu_1 + a_1\,u + b_1\,v\,, \qquad A_2 = \mu_2 + a_2\,u + b_2\,v \tag{151}$$

and rewrite (149) as

$$\begin{aligned} 0 &= 2\,A_1\,u + c_1\,w\,, \qquad 0 = 2\,A_2\,v + c_2\,w \\ 0 &= (2\,A_1 + A_2)\,w + 2\,(c_2\,u + 2\,c_1\,v)\,u \\ &\quad + (2e_1 - e_2)\,q \\ 0 &= (2\,A_1 + A_2)\,q - (2e_1 - e_2)\,w \end{aligned} \tag{152}$$

We already know that $[0, 0, 0, 0]$ and $[0, -\mu_2/b_2, 0, 0]$ are the only roots in the $u = 0$ and $v = 0$ subspaces, so we are looking only for the $u > 0$, $v > 0$, $w, q \in \mathbb{R}$ solutions; there could be non-generic roots with either $w = 0$ or $q = 0$, but not both simultaneously, since the

syzygy (146) precludes that. Either w or q can be eliminated by obtaining the following relations from (152):

$$\begin{aligned} w &= -\frac{2\,u}{c_1}\,A_1 = -\frac{2\,v}{c_2}\,A_2 \\ q &= \frac{2(-2e_1+\,e_2)\,u\,v}{c_2\,u+2\,c_1\,v}. \end{aligned} \tag{153}$$

Substituting (153) into (152) we get two bivariate polynomials whose roots are the equilibria of the system (149):

$$\begin{aligned} f(u,v) &= c_2\,u\,A_1 - c_1\,v\,A_2 = 0\,, \\ g(u,v) &= \left(4\,A_1^2u^2 - 4\,c_1^2\,u^2v\right)(c_2\,u+2\,c_1\,v)^2 \\ &\quad + 4\,c_1^2\,(-2e_1+e_2)^2\,u^2\,v^2 = 0\,. \end{aligned} \tag{154}$$

We divide the common multiplier u^2 from the second equation and by doing so, eliminate one of the two roots at the origin, as well as the $[0,-\mu_2/b_2,0,0]$ root within the invariant subspace (144). Furthermore, we scale the parameters and variables as $\tilde{u}=c_2\,u$, $\tilde{v}=c_1\,v$, $\tilde{a_1}=a_1/c_2$, $\tilde{b_1}=b_1/c_1$, $\tilde{a_2}=a_2/c_2$, $\tilde{b_2}=b_2/c_1$ to get

$$\tilde{f}(\tilde{u},\tilde{v}) = \tilde{u}\,\tilde{A}_1 - \tilde{v}\,\tilde{A}_2 = 0\,, \tag{155}$$

$$\tilde{g}(\tilde{u},\tilde{v}) = \left(\tilde{A}_1^2 - c_1\,\tilde{v}\right)(\tilde{u}+2\,\tilde{v})^2 + e_2^2\,\tilde{v}^2 = 0\,, \tag{156}$$

where $\tilde{A}_1=\mu_1+\tilde{a_1}\,\tilde{u}+\tilde{b_1}\,\tilde{v}$ and $\tilde{A}_2=\mu_2+\tilde{a_2}\,\tilde{u}+\tilde{b_2}\,\tilde{v}$.

Solving coupled bivariate polynomials such as (155) and (156), is not, in general, a trivial task. However, for the choice of parameters given by (142), Eq. (155) yields $\tilde{v}=(\mu_1+\tilde{a}_1\tilde{u})/(\mu_2+\tilde{a}_2\tilde{u})$. Substituting this into (156) makes it a fourth order polynomial in u, which we can solve. Only the non-negative, real roots of this polynomial correspond to relative equilibria in the two-modes state space since u and v are the squares of first and second mode amplitudes, respectively. Two roots satisfy this condition, the equilibrium at the origin

$$p_{\mathrm{E}} = [0,0,0,0]\ , \tag{157}$$

and the relative equilibrium

$$p_{\mathrm{TW}} = [0.193569, 0.154131, -0.149539, -0.027178]\ . \tag{158}$$

Note that by setting $b_2=0$, we send the relative equilibrium at $[0,-\mu_2/b_2,0,0]$ to infinity. Thus, (158) is the only relative equilibrium of the two-modes system for our choice of parameters. While this is an equilibrium in the invariant polynomial basis, in the SO(2)-equivariant, real-valued state space this is a 1-dimensional relative equilibrium group orbit. The point on this orbit that lies in first Fourier mode slice is (see Figure 9 (c)):

$$(x_1,y_1,x_2,y_2) = (0.439966, 0, -0.386267, 0.070204)\ . \tag{159}$$

We computed the linear stability eigenvalues and eigenvectors of this relative equilibrium, by analyzing the stability matrix within the first Fourier mode slice $\hat{A}_{ij}(\hat{a}) = \partial\hat{v}_i/\partial\hat{a}_j|_{\hat{a}}$ (107), resulting in linear stability eigenvalues

$$\lambda_{1,2} = 0.05073 \pm i\,2.4527, \quad \lambda_3 = -5.5055, \quad \lambda_4 = 0\,. \tag{160}$$

The 0 eigenvalue corresponds to the direction outside the slice. We expect this since the reduced trajectory evolution equation (95) keeps the solution within the slice. The imaginary part of the expanding complex pair sets the 'winding time' in the neighborhood of the equilibrium to $T_w = 2\pi/\mathrm{Im}\,(\lambda_1) = 2.5617$. The large magnitude of the contracting eigenvalue λ_3 yields a very thin attractor in the reduced state space, thus, when looked at on a planar Poincaré section, the two-modes flow is almost one-dimensional, as shown in Figs. 10(a) and 10(b).

4.1.3 No chaos when the reflection symmetry is restored

Before finishing our discussion of invariant polynomials, we make an important observation regarding the case when both of the reflection symmetry breaking parameters, e_1 and e_2 are set to 0. In this case, $z_{1,2} \to \bar{z}_{1,2}$ symmetry is restored and the evolution equations for u, v, and w in (149) become independent of q. Furthermore, the time evolution equation for q becomes linear in q itself, so that it can be expressed as

$$\dot{q} = \xi(u, v)q\,. \tag{161}$$

Hence, the time evolution of q can be written as

$$q(\tau) = e^{\int_0^\tau d\tau' \xi(u(\tau'),v(\tau'))} q(0)\,. \tag{162}$$

If we assume that the flow is bounded, then we can also assume that a long time average of ξ exists. The sign of this average determines the long term behavior of $q(\tau)$; it will either diverge or vanish depending on the sign of $\langle\xi\rangle$ being positive or negative respectively. The former case leads to a contradiction: If $q(\tau)$ diverges, the symmetry-invariant flow cannot be bounded since the syzygy (146) must be satisfied at all times. If $q(t)$ vanishes, there are three invariant polynomials left, which are still related to each other by the syzygy. Thus, the flow is confined to a two-dimensional manifold and cannot exhibit chaos. We must stress that this is a special result that holds for the two-mode normal form with terms up to third order.

4.1.4 Two-modes system in the first Fourier mode slice

Reduction of SO(2) symmetry of the two-modes system via first Fourier mode slice is straightforward as described in Sect. 3.3.3. We choose the slice template as $\hat{a}' = (1, 0, 0, 0)^T$, which defines the first Fourier mode slice as the half-hyperplane

$$y_1 = 0\,, x_1 > 0\,. \tag{163}$$

Reduced velocity field for the two-modes system in the first Fourier mode slice is given by

$$\hat{v}(\hat{a}) = v(\hat{a}) - \frac{\dot{y}_1\,(\hat{a})}{\hat{x}_1}\, t(\hat{a})\,, \tag{164}$$

where we substituted the phase velocity $\dot{\theta} = \dot{y}_1(a)/\hat{x}_1$. The slice border condition (97) for the two-modes system corresponds to $\hat{x}_1 = |z_1| = 0$, however, in this particular problem, this condition is never satisfied since $z_1 = 0$ is a flow-invariant subspace (144) of the two-modes system.

Figure 7 shows visualizations of the slice half-hyperplane (blue, transparent), three group orbits (yellow, green, and pink), and group tangents (red arrows) at the intersection

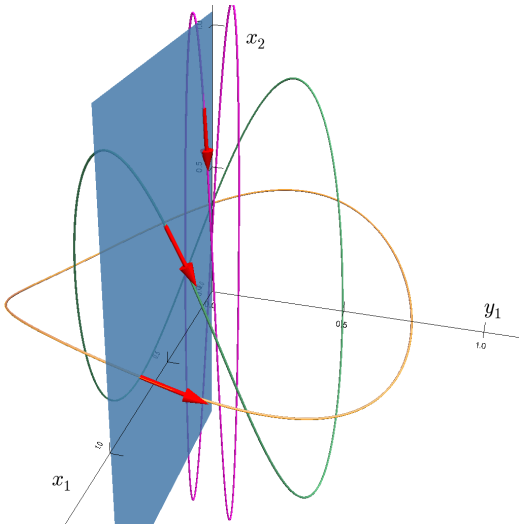

Figure 7: SO(2) group orbits of state space points $(0.75, 0, 0.1, 0.1)$ (orange), $(0.5, 0, 0.5, 0.5)$ (green) $(0.1, 0, 0.75, 0.75)$ (pink) and the first Fourier mode (163) slice hyperplane (blue). The group tangents at the intersections with the slice hyperplane are shown as red arrows. As the magnitude of the first Fourier mode decreases relative to the magnitude of the second one, so does the group tangent angle to the slice hyperplane.

of group orbits with the first Fourier mode slice as projections onto (x_1, y_1, x_2). In Figure 7, the slice hyperplane appears two-dimensional as a result of its definition (163), however, one should keep in mind that it has a third dimension y_2 that is not shown in this projection. For the group orbits, we have chosen three points in the slice with decreasing first Fourier mode amplitude in order to illustrate the following: When the magnitude of the first mode is small relative to that of the second (pink curve), the group tangent at the representative point for the group orbit (i.e., where the group orbit and the slice hyperplane intersect) has a larger component parallel to the slice hyperplane. If the magnitude of the first mode was exactly 0, the group tangent would lie entirely on the slice hyperplane, satisfying the slice border condition (97).

4.1.5 Visualizing two-modes dynamics

We now present visualizations of the dynamics of the two-modes system in four different representations: as 3D projections of the four-dimensional real-valued state space, as 3D projections in the invariant polynomial basis, as dynamics in the 3D slice hyperplane, and as two-dimensional spacetime diagrams of the color-coded field $u(x, \tau)$, which is defined as follows:

$$u(x, \tau) = \sum_{k=-2}^{2} z_k(\tau)\, e^{ikx}\,, \tag{165}$$

where $z_{-k} = \bar{z}_k\,,\ z_0 = 0$, and $x \in [-\pi, \pi]$. We can also define the symmetry reduced field $\hat{u}(x, \tau)$, as the inverse Fourier transform of the symmetry reduced Fourier modes:

$$\hat{u}(x, \tau) = \sum_{k=-2}^{2} \hat{z}_k(\tau) e^{ikx}\,, \tag{166}$$

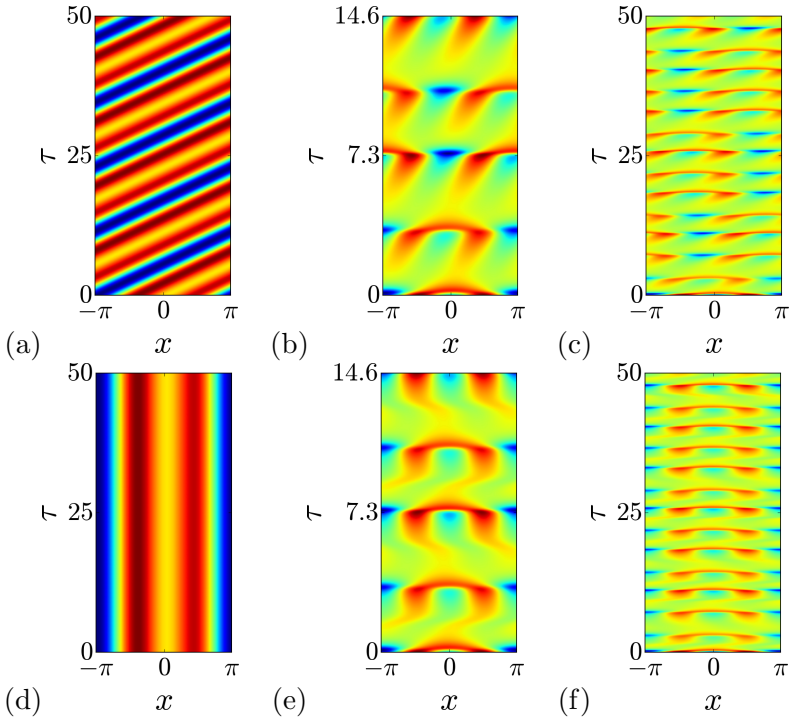

Figure 8: The relative equilibrium TW in (a) the scalar field representation becomes an equilibrium of (d) the symmetry-reduced field. Two cycles of the relative periodic orbit $\overline{01}$ of (b) the symmetry-equivariant field become a periodic orbit of (e) the symmetry-reduced field. (c) A typical ergodic trajectory of the two-modes system in the symmetry-equivariant field representation, (f) in the symmetry-reduced field representation. The color scale used in each figure is different to enhance contrast.

where $\hat{z}_{-k} = \bar{\hat{z}}_k \ , \quad \hat{z}_0 = 0 \quad$ and $x \in [-\pi, \pi]$. (165) defines an analogous physical space representation for the two-modes system as a scalar field in one space dimension, similar to the one we discussed in Sect. 3.1. In this representation, we expect SO(2) group action to become translations in space coordinate x. Figures 8 (a) and 8 (d) show the sole relative equilibrium TW of the two-modes system as color coded amplitude of the symmetry-equivariant and symmetry-reduced fields, respectively. After symmetry reduction, the relative equilibrium becomes an equilibrium. Figures 8 (b) and 8 (e) show the relative periodic orbit $\overline{01}$ again respectively in the symmetry-equivariant and symmetry-reduced scalar field representations. Similar to the relative equilibrium, the relative periodic orbit becomes a periodic orbit after symmetry reduction. Finally, Figures 8 (c) and 8 (f) show a typical ergodic trajectory of the two-modes system in symmetry-equivariant and symmetry-reduced scalar field representations. Note that in each case, symmetry reduction cancels the 'drifts' along the symmetry (x) direction.

As can be seen clearly in Figure 9 (a), these drifts show up in state space as SO(2) rotations. The relative equilibrium TW traces its SO(2) group orbit (green curve in Figure 9 (a)) as it drifts in space. The relative periodic orbit $\overline{01}$ (red) and the ergodic trajectory (blue) rotate in the same fashion as they evolve. Figures 9(b) and 9(c) show a three-dimensional projection onto the invariant polynomial basis and the 3-dimensional trajectory on the slice hyperplane for the same orbits. In both figures, the relative equilibrium is reduced to an equilibrium and the relative periodic orbit is reduced to a periodic orbit.

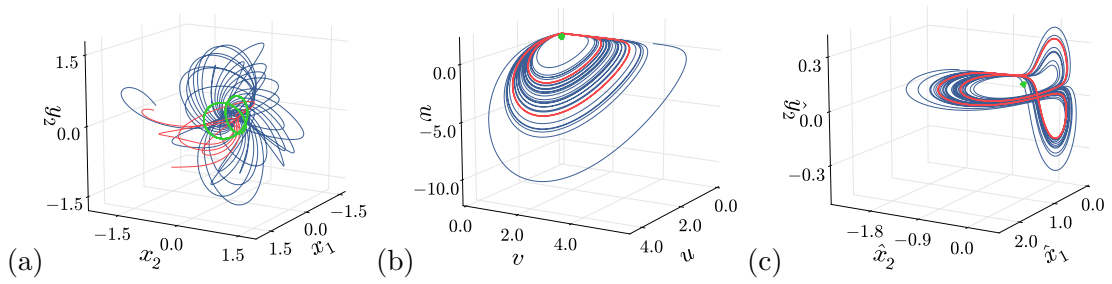

Figure 9: The relative equilibrium TW (green), two repeats of the relative periodic orbit $\overline{01}$ (red), and a chaotic trajectory (blue) of the two-modes system (a) in a 3D projection of the 4-dimensional state space, (b) in a terms of 3 invariant polynomials, (c) in the 3-dimensional first Fourier mode slice hyperplane. Note that in the symmetry reduced representations (b and c), the relative equilibrium TW is reduced to an equilibrium, the green point; and the periodic orbit $\overline{01}$ (red) closes onto itself after one repeat. In contrast to the invariant polynomial representation (b), in the first Fourier mode slice hyperplane (c), the qualitative difference between shifts by $\approx \pi$ and $\approx -\pi$ in near passages to the slice border is very clear, and it leads to the unimodal Poincaré return map of Figure 10.

4.2 Periodic orbits

The simple structure of the symmetry-reduced dynamics allows us to determine the relative periodic orbits of the two-modes system by means of a Poincaré section and a return map. We illustrate this procedure in Figure 10. Starting with an initial point close to the TW, we compute a long, symmetry-reduced ergodic trajectory by integrating (95) and record where it crosses the Poincaré section, which we define as the plane that contains TW and is spanned the imaginary part of its unstable stability eigenvector and $\hat{y}_2$. We then project these points onto a basis (v_1, v_2), which spans the Poincaré section and fit cubic splines to the data as shown in Figure 10 (b). This allows us to construct a return map along this curve, which can be expressed in terms of the distance s from TW as measured by the arc length along the cubic spline fit. The resulting map, which is shown in Figure 10 (c), is unimodal with a sharp cusp located at its critical point. Note that the region $s \in (0, 0.6)$ corresponds to the neighborhood of the relative equilibrium and is only visited transiently. Once the dynamics fall onto the chaotic attractor, this region is never visited again. Removing this region from the return map, we obtain the return map shown in Figure 10 (d), which we can then use to determine the accessible relative periodic orbits with their respective binary symbol sequences.

The unimodal return map of Figure 10 (d) diverges around $s \approx 0.98$ and this neighborhood is visited very rarely by the flow. We took the furthest point that is visited by the ergodic flow, $s_C = 0.98102264$ as the critical point of this map and coded points to the left and right hand sides of this point as '0' and '1' respectively, and constructed a binary symbolic dynamics. This encoding is going to allow us to find all accessible periodic orbits of the two-modes system as we shall explain next.

4.2.1 Determining admissible cycles

We would like to find all relative periodic orbits of the two-modes system up to a certain period in order to carry out periodic orbit theory calculations. For unimodal maps such as Figure 10 (d), we can achieve this by kneading theory. In this section, we are going to

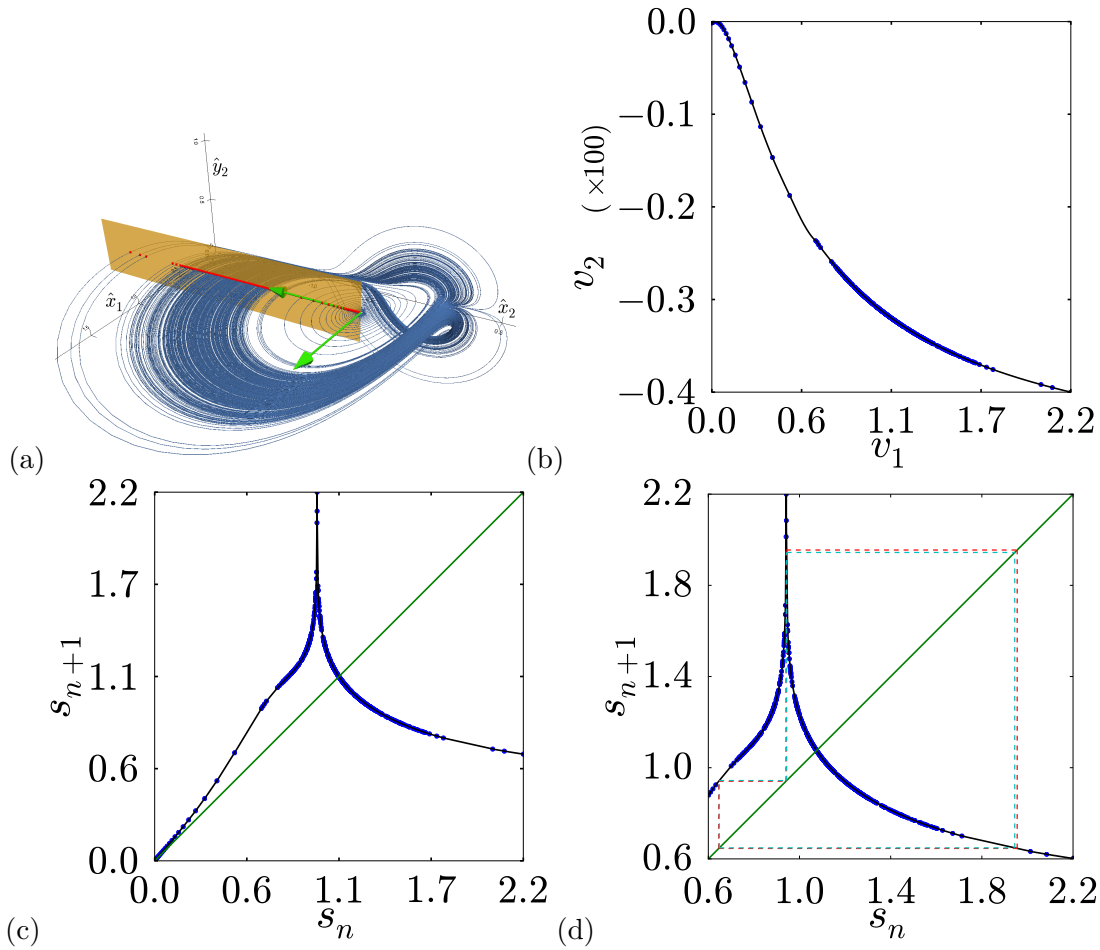

Figure 10: (a) A Symmetry-reduced ergodic trajectory within the slice hyperplane (blue). Green arrows indicate the real and imaginary parts of the complex eigenvectors v_u that span the linear unstable manifold of TW. The Poincaré section, which contains TW and is spanned by $\mathrm{Im}\,[v_u]$ and $\hat{y}_2$, is visualized as a transparent plane. Points where the flow crosses the section are marked in red. (b) A closer look at the Poincaré section shows that the attractor is very thin. Note that the vertical axis, which corresponds to the direction parallel to $\hat{y}_2$ is magnified by 100. All (blue) points are located relative to the TW, which is at the origin. The black curve is a cubic spline interpolation of the data. (c) By measuring arclengths s along the interpolation curve, a return map of the Poincaré section can be constructed. Note that once the flow exits the neighborhood of the TW ($s < 0.6$) it stays on the attractor and never comes back. Thus the data up to this point is transient. (d) The return map without the transient points framed by orbit of the critical point. Dashed lines show the 3-cycles $\overline{001}$ (red) and $\overline{011}$ (cyan).

state the symbolic dynamics methods we use in this chapter and for a general pedagogical introduction to these topics, we refer the reader to refs. [24, 30].

Let $s_1, s_2, s_3, \ldots$ be the orbit of an initial point s_0 under a unimodal return map $s_{n+1} = f(s_n)$, such as Figure 10 (d), then the *future itinerary* $I^+(s_0) = .i_1 i_2 i_3 \ldots$ of s_0 is given by

$$i_n = \begin{cases} 0 & \text{if} \quad s_n < s_C \\ C & \text{if} \quad s_n = s_C \\ 1 & \text{if} \quad s_n > s_C \end{cases} . \tag{167}$$

Unimodal maps that contain all possible itineraries are said to have complete binary symbolic dynamics. A canonical example of such maps is full tent map

$$f(\gamma) = 1 - 2|\gamma - 1/2| \,, \qquad \gamma \in \mathcal{M} = [0,1] \,, \tag{168}$$

which has a critical point at $\gamma = 1/2$ as shown in Figure 11 (a). Figure 11 (a) also shows partitions of the unit interval according to the first iterate of the map. This partition should not be mistaken with the future itinerary in (167): Labels in spatial partition of the unit interval starts from the initial point i.e. 00 corresponds to the initials points on the LHS of the γ_C that stays on the same side after iteration, 01 means initial points on the LHS of the γ_C that goes to the RHS after one iteration, and so on. One can obtain finer partitions of the unit interval by considering longer symbol sequences, doubling the precision at each step. This yields the relation between the future itinerary $I^+(\gamma_0) = .i_1 i_2 i_3 \ldots$ of a point γ_0 and its image $\gamma_1 = f(\gamma_0)$ that can be computed via the following algorithm

$$\begin{aligned} w_{n+1} &= \begin{cases} w_n & \text{if} \quad i_{n+1} = 0 \\ 1 - w_n & \text{if} \quad i_{n+1} = 1 \end{cases} , \qquad w_1 = i_1 \\ \gamma(I^+) &= \gamma_1 = \sum_{n=1}^{\infty} \frac{w_n}{2^n} \,. \end{aligned} \tag{169}$$

Since we can compute binary future itinerary of every point on a unimodal map, such as the one in Figure 10, we can compute their counterparts on the full tent map via (169). This defines a topological conjugacy between all unimodal maps and the full tent map, hence $\gamma(I^+)$ is called (future) "topological coordinate".

It can be confirmed by inspection that the topological coordinate of the critical point of the tent map is $\gamma(I^+(\gamma_c)) = 1$ as expected. However, this is not the case for any unimodal map. In fact, this would be only true if the map had complete binary symbolic dynamics, that is all possible itineraries are accessible in the system. Generically, topological coordinate of the critical point $\kappa = \gamma(I^+(s_C))$ is different from 1. As a canonical example, consider the dike map

$$f(\gamma) = \begin{cases} f_0(\gamma) = 2\gamma & \gamma \in \mathcal{M}_0 = [0, \kappa/2) \\ f_c(\gamma) = \kappa & \gamma \in \mathcal{M}_c = [\kappa/2, 1-\kappa/2] \\ f_1(\gamma) = 2(1-\gamma) & \gamma \in \mathcal{M}_1 = (1-\kappa/2, 1] \end{cases} , \tag{170}$$

which is obtained by modifying the tent map (168) by setting images of $\gamma \in [\kappa/2, 1-\kappa/2]$ to κ. It can be seen from Figure 11 (b) that this modification disallows any orbit to reach $\gamma > \kappa$ part of the unit interval. Consequently, periodic orbits of the tent map, which visit $\gamma > \kappa$ part of the unit interval are "pruned" in the dike map (170). This is the main topological correspondence that we are going to use to determine accessible periodic orbits. Due to

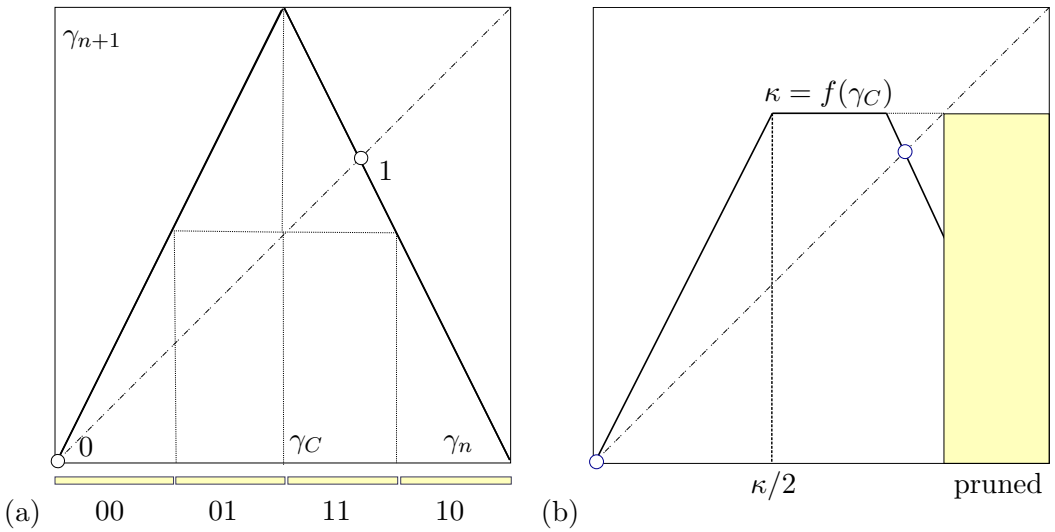

Figure 11: (a) Full tent map (168) and its partition $\mathcal{M}_{00}$, $\mathcal{M}_{01}$, $\mathcal{M}_{10}$, $\mathcal{M}_{11}$ according to symbolic dynamics. (b) The dike map is obtained by slicing off the top portion of the tent map in (a). Any full tent map orbit that visits the primary pruning interval $(\kappa, 1]$ is inadmissible.

their particular importance, future itinerary and the corresponding topological coordinate of the critical point have special names: $K = I^+(s_C)$ is called the "kneading sequence" and $\kappa = \gamma(K)$ is called the "kneading value".

We are now ready to explain how admissible periodic orbits are determined. Let us assume the future itinerary $I^+(s_p) = .\overline{i_0 i_1 i_2 \dots i_{n-1}}$ belongs to a periodic orbit of discrete period n and define the shift operator σ as

$$\sigma I^+(s_p) = .\overline{i_1 i_2 \dots i_{n-1} i_0} = I^+(f(s_p))\,. \tag{171}$$

The *maximal value* of a future itinerary is given by

$$\hat{\gamma}(I^+(s_p)) = \sup_m \gamma(\sigma^m I^+(s_p)) \tag{172}$$

In any unimodal map, if the maximal value $\hat{\gamma}(I^+(s_p))$ of a periodic orbit p is smaller than the kneading value κ, then this orbit is admissible. By checking this for all possible binary itineraries, we determine all admissible cycles of the two-modes system.

4.2.2 Finding relative periodic orbits

We are now going to summarize the procedure of locating relative periodic orbits in the state space: Suppose the binary itinerary $\overline{i_0 i_1 i_2 \dots i_{n-1}}$, where $i_j = 0, 1$ corresponds to an admissible 'n-cycle', a relative periodic orbit that intersects our Poincaré section n-times. We first find arc-lengths $\{s_0, s_1, \dots s_{n-1}\}$ that constitute this cycle on the return map Figure 10 (d) from the fixed points of the nth iterate of the return map. We then find corresponding reduced state space points $\{\hat{a}_0, \hat{a}_1, \dots \hat{a}_{n-1}\}$. Finally, we integrate the reduced flow (95) and the phase (96) starting from each point $\hat{a}_j$ until it returns to the Poincaré section, and divide this trajectory into N small pieces. As a result, we obtain $n \times N$ state space points, durations and phase shifts $\{a_i^{(0)}, \tau_i^{(0)}, \theta_i^{(0)}\}$, where $i = 1, 2, \dots n \times N$,

which we feed into the multiple shooting Newton solver (see Appendix A) to precisely determine the relative periodic orbit, its period and the associated phase shift. After finding $n \times N$ state space points (a_i), flight times (τ_i), and phase shifts (θ_i) associated with the n cycle, we can compute the stability of the orbit. We do this by computing the Jacobian associated with each segment of the orbit $J^{\tau_i}(a_i)$, so that the Jacobian associated with the relative periodic orbit is then

$$\begin{aligned} \hat{J} &= g(-\theta_{n\times N})J^{\tau_{n\times N}}(a_{n\times N})\dots \\ &\quad g(-\theta_2)J^{\tau_2}(a_2)g(-\theta_1)J^{\tau_1}(a_1)\,. \end{aligned} \tag{173}$$

This construction (173) of the Jacobian is equivalent to our definition in (85), since the group action g and the Jacobian J are both multiplicative and commute with each other as a consequence of g-equivariance of the flow. The form (173) is essential in determining its eigenvalues (Floquet multipliers) precisely, since it allows us to use periodic Schur decomposition, as described in Appendix B.

Table 1: Itinerary, period (T), phase shift (θ), Floquet multiplier (Λ), and Floquet exponent (λ) of the found two-modes relative periodic orbits with topological lengths up to $n = 5$, more (up to $n = 12$) available upon request.

Itinerary	T	θ	Λ	λ
1	3.64151221	0.08096967	-1.48372354	0.10834917
01	7.34594158	-2.94647181	-2.00054831	0.09439516
001	11.07967801	-5.64504385	-55.77844510	0.36295166
011	11.07958924	-2.50675871	54.16250810	0.36030117
0111	14.67951823	-2.74691247	-4.55966852	0.10335829
01011	18.39155417	-5.61529803	-30.00633820	0.18494406
01111	18.38741006	-2.48213868	28.41893870	0.18202976

We found the admissible cycles of the two-modes system up to the topological length 12. We listed binary itineraries of shortest 7 relative periodic orbits (with topological lengths up to 5), along with their periods, phase shifts, leading (expanding) Floquet multipliers, and corresponding Floquet exponents in Table 1. Remaining three Floquet multipliers of the relative periodic orbits are two marginal ones corresponding to continuous symmetry and velocity field directions and a strongly contracting one corresponding to the direction pointing outside the attractor. In Figure 12 (a) we show shortest 4 of the relative periodic orbits of the two-modes system within the first Fourier mode slice hyperplane. As seen from Figure 12 (a), trajectories of $\overline{001}$ (red) and $\overline{011}$ (cyan) almost overlap in a large region of the state space. This behavior is also manifested in the return map of Figure 10 (d), where we have shown cycles $\overline{001}$ and $\overline{011}$ with red and cyan respectively. This is a general property of the two-modes cycles with odd topological lengths: They come in pairs with almost equal leading (largest) Floquet exponents, see Figure 12 (b). Floquet exponents (λ_j) characterize the rate of expansion/contraction of nearby perturbations to the relative periodic orbits and are related to Floquet multipliers (Λ_j) by

$$\lambda_{\tilde{p},j} = \frac{1}{T_{\tilde{p}}} \ln |\Lambda_{\tilde{p},j}|\,, \quad j = 1, 2, \dots, d\,, \tag{174}$$

where the subscript $\tilde{p}$ associates $\lambda_{\tilde{p},j}$ and Λ_j with the 'prime relative periodic orbit' p and

its period $T_{\tilde{p}}$. Having computed periods, phase shifts, and Floquet multipliers of relative periodic orbits, we are now ready to calculate dynamical averages and other statistical moments of observables using cycle averaging formulas.

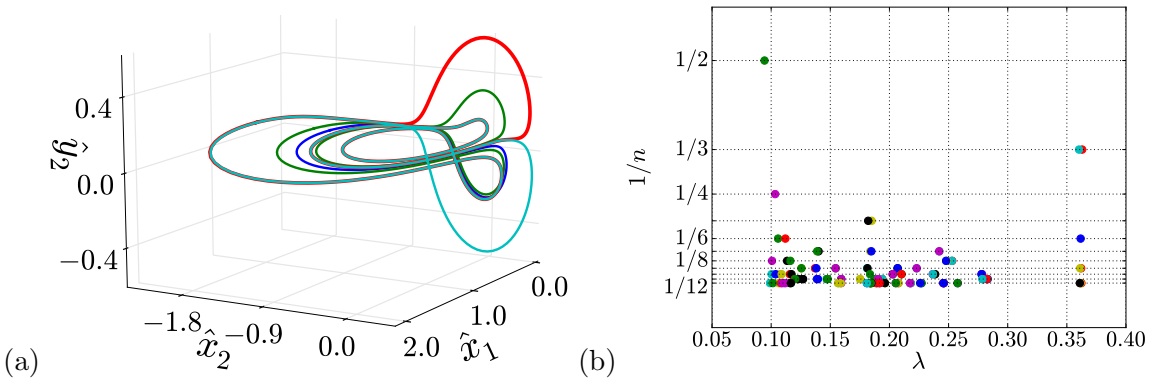

Figure 12: (a) The shortest four relative periodic orbits of the two-modes system: $\overline{1}$ (dark blue), $\overline{01}$ (green), $\overline{001}$ (red), $\overline{011}$ (cyan). Note that relative periodic orbits $\overline{001}$ and $\overline{011}$ almost overlap everywhere except $\hat{x}_1 \approx 0$ (b) Distribution of the expanding Floquet exponents of all two-modes cycles with topological lengths n from 2 to 12. .

4.3 Cycle Averages

We finished Chapter 2 by writing down the spectral determinant (62), zeros of which were located at the eigenvalues of the infinitesimal evolution operator $\mathcal{A}$. This formula consist of an exponential of sums of all periodic orbits of the system and their repeats and it is not obvious at all how can we evaluate it using our numerically found relative periodic orbits of the two-modes system. We begin this section by introducing the cycle expansions, which will tell us how to order terms in the spectral determinant.

4.3.1 Cycle expansions

In order to understand the convergence properties of the spectral determinant, we are going to make an approximation that greatly simplifies its form. The term $\left|\det\left(\mathbf{1}-M_p\right)\right|$ that appears in the spectral determinant can be expanded as follows

$$\begin{aligned}\left|\det\left(\mathbf{1}-M_p\right)\right| &= \left|(1-\Lambda_{e,1})(1-\Lambda_{e,2})...(1-\Lambda_{c,1})(1-\Lambda_{c,2})...\right| , \\ &= \left|\left(\prod_e \Lambda_e\right)(\Lambda_{e,1}^{-1}-1)(\Lambda_{e,2}^{-1}-1)...(1-\Lambda_{c,1})(1-\Lambda_{c,2})...\right| , \quad (175)\end{aligned}$$

where we labeled expending $|\Lambda_{e,k}| > 1$ and contracting $|\Lambda_{c,k}| < 1$ Floquet multipliers of the periodic orbit p with subscripts e, c and in the second line we rewrote the expansion by separating the product of expanding eigenvalues. Assuming that we do not have any near-marginal ($\Lambda \approx 1$) Floquet multipliers, all terms in (175) except the product are order $O(1)$ or smaller, hence the dominant term of this expansion is the product at the front. Defining $|\Lambda_p| \equiv \prod_e |\Lambda_e|$ we approximate (175) for periodic orbit p and its repeats as follows

$$\left|\det\left(\mathbf{1}-M_p^r\right)\right| \approx |\Lambda_p|^r . \quad (176)$$

The spectral determinant within this approximation is called *dynamical zeta function*

$$1/\zeta = \exp\left(-\sum_p \sum_{r=1}^{\infty} \frac{1}{r} \frac{e^{r(\beta\Omega_p - sT_p)}}{|\Lambda_p|^r}\right) . \tag{177}$$

Notice in (177) that the terms inside the sum are all powers of r divided by r. Defining $t_p \equiv e^{(\beta\Omega_p - sT_p)}/|\Lambda_p|$, inner sum becomes $\sum_{r=1}^{\infty} t_p^r/r = -\ln(1-t_p)$, hence the dynamical zeta function can be brought to the *Euler product* form

$$1/\zeta = \prod_p (1-t_p) \tag{178}$$

Cvitanović [20] realized that if one has complete binary symbolic dynamics, the Euler product (178) can be expanded in the following form

$$\begin{aligned} 1/\zeta &= 1 - t_0 - t_1 - (t_{01} - t_0 t_1) \qquad (179) \\ &\quad -[(t_{011} - t_{01}t_1) + (t_{001} - t_{01}t_0)] - ... \\ &= 1 - \sum_f t_f - \sum_n \hat{c}_n, \qquad (180) \end{aligned}$$

where we labeled each prime cycle by its binary symbol sequence. In (180) we separated the contributions to the zeta function into two groups: 'fundamental' contributions t_f and 'curvature' corrections c_n. The curvature correction terms are denoted explicitly by parentheses in (179) and correspond to 'shadowing' combinations where combinations of shorter cycle weights, also known as 'pseudocycle' weights, are subtracted from the weights of longer prime cycles. Since the cycle weights in (178) already decrease exponentially with increasing cycle period, the cycle expansion (179) converges even faster than exponentially when the terms corresponding to longer prime cycles are shadowed.

The cycle expansion (179) of the dynamical zeta function completes the theoretical exposition of Chapter 2 by telling us that we should order cycle contributions according to their topological lengths. Ref. [5] studied the properties of (180) in detail, and ref. [6] carried out cycle averages in several low-dimensional dynamical systems. These papers concluded that the cycle expansions is an effective method for computation of long term averages of dynamical systems if one has a good understanding of the topology (symbolic dynamics) and cycles are hyperbolic, i.e. they do not have marginal ($|\Lambda| = 1$) Floquet multipliers. Following refs. [5, 6], Rugh [99] showed that if the symbolic dynamics is a subshift of finite type, [24] with the grammar of admissible sequences described by a finite set of pruning rules, and the flow is uniformly hyperbolic, cycle expansions of spectral determinants are guaranteed to converge super-exponentially.

A generic unimodal map symbolic dynamics is not a subshift of finite type. However, we have shown in Sect. 4.2 that the Poincaré return map for the two-modes system (Figure 10 (d)) diverges at $s \approx 0.98$ and approximated it as if its tip was located at the furthest point visited by an ergodic trajectory. This brings the question of whether we can approximate the map in Figure 10 (d) in such a way that corresponding symbolic dynamics has a finite grammar of pruning rules? The answer is yes.

4.3.2 Finite grammar approximation

As shown in Figure 10 (d), the cycles $\overline{001}$ and $\overline{011}$ pass quite close to the tip of the cusp. Approximating the map as if its tip is located exactly at the point where $\overline{001}$ cuts gives us

what we are looking for: a single grammar rule, which says that the symbol sequence '00' is inadmissible. This can be made rigorous by the help of kneading theory, however, the simple result is easy to see from the return map in Figure 10 (d): Cover the parts of the return map, which are outside the borders set by the red dashed lines (the cycle $\overline{001}$) and then start any point to the left of the tip and look at images. You will always land on a point to the right of the tip, unless you start at the lower left corner, exactly on the cycle $\overline{001}$. As we will show, this 'finite grammar approximation' is reasonable since the orbits that visit outside the borders set by $\overline{001}$ are very unstable, and hence, less important for the description of invariant dynamics.

The binary grammar with only rule that forbids repeats of one of the symbols is known as the 'golden mean' shift, [24] because it has a topological entropy of $\ln\left(\left(1+\sqrt{5}\right)/2\right)$. Binary itineraries of golden mean cycles can be easily obtained from the complete binary symbolic dynamics by substitution $0 \to 01$ in the latter. Thus, we can write the dynamical zeta function for the golden mean pruned symbolic dynamics by replacing 0s in (179) by 01:

$$\begin{aligned} 1/\zeta &= 1 - t_{01} - t_1 - (t_{011} - t_{01}t_1) \\ &\quad -[(t_{0111} - t_{011}t_1) + (t_{01011} - t_{01}t_{011})] - \ldots \end{aligned} \tag{181}$$

Note that all the contributions longer than topological length 2 to the golden mean dynamical zeta function are in form of shadowing combinations. In Sect. 4.4.1, we will compare the convergence of the cycle averages with and without the finite grammar approximation, but before moving on to numerical results, we explain the remaining details of computation.

4.4 Cycle expansions the of spectral determinant

While dynamical zeta functions are useful for investigating the convergence properties, they are not exact, and their computational cost is same as that of exact spectral determinants. For this reason, we expand the spectral determinant (62) ordered in the topological length of cycles and pseudocycles. We start with the following form of the spectral determinant (62)

$$\det(s-\mathcal{A}) = \prod_p \exp\left(-\sum_{r=1}^{n_p r<N} \frac{1}{r}\frac{e^{r(\beta\Omega_p - sT_p)}}{\left|\det\left(\mathbf{1}-M_p^r\right)\right|} z^{n_p r}\right), \tag{182}$$

where the sum over the prime cycles in the exponential is taken out as product. We also inserted the order tracking term z, which we will set to 1 at the final step, and truncated the sum over cycle repeats at the expansion order N. For each prime cycle, we compute the sum in (182) and expand the exponential up to order N. We then multiply this expansion with the contributions from previous cycles and drop terms with order greater than N. This way, after setting $z=1$, we obtain the spectral determinant truncated to cycles and pseudo-cycles of topological length up to $n_p \le N$,

$$F_N(\beta, s) = 1 - \sum_{n=1}^{N} Q_n(\beta, s)\,, \tag{183}$$

where we denoted the Nth order spectral determinant by F_N and nth order term in its cycle expansion by Q_n. In what follows, we shall drop the subscript, $F_N \to F$, but actual calculations are always done for a range of finite truncation lengths N. Remember that we

are searching for the eigenvalues $s(\beta)$ of the operator $\mathcal{A}$ in order to compute the moments (50) and (54). These eigenvalues are located at the zeros of the spectral determinant, hence as function of β they satisfy the implicit equation

$$F(\beta, s(\beta)) = 0\,. \tag{184}$$

By taking derivative of (184) with respect to β and applying chain rule we obtain

$$\frac{ds}{d\beta} = -\frac{\partial F}{\partial \beta} \Big/ \frac{\partial F}{\partial s}\,. \tag{185}$$

Higher order derivatives can be evaluated similarly. Defining

$$\begin{aligned} \langle \Omega \rangle &= -\partial F/\partial \beta\,, \\ \langle T \rangle &= \partial F/\partial s\,, \qquad \langle T^2 \rangle = \partial^2 F/\partial s^2\,, \\ \langle \Omega^2 \rangle &= -\partial^2 F/\partial \beta^2\,, \qquad \langle \Omega T \rangle = \partial^2 F/\partial \beta \partial s\,, \end{aligned} \tag{186}$$

we write the cycle averaging formulas as

$$\langle \omega \rangle = \langle \Omega \rangle / \langle T \rangle\,, \tag{187}$$

$$\begin{aligned} \Delta &= \frac{1}{\langle T \rangle} \left(\langle \Omega^2 \rangle - 2 \frac{ds}{d\beta} \langle \Omega T \rangle + \left(\frac{ds}{d\beta} \right)^2 \langle T^2 \rangle \right) \\ &= \frac{1}{\langle T \rangle} \langle (\Omega - T \langle \omega \rangle)^2 \rangle\,, \end{aligned} \tag{188}$$

with everything evaluated at $\beta = 0$, $s = s(0)$.

By probability conservation, we expect that for an invariant measure $\rho_0(a)$, the eigenvalue $s(0)$ is 0. However, we did not make this substitution in cycle averaging formulas since, in practice, our approximations to the spectral determinant are always based on a finite number of periodic orbits, so that the solution of $F_N(0, s(0)) = 0$ is small, but not exactly 0. This eigenvalue has a special meaning: It indicates how well the periodic orbits cover the strange attractor. Following this interpretation, we define $\gamma = -s(0)$ as the 'escape rate': the rate at which the dynamics escape the region that is covered by the periodic orbits. Specifically, for our finite grammar approximation; the escape rate tells us how frequently the ergodic flow visits the part of the Poincaré map that we cut off by applying our finite grammar approximation.

We defined $\langle T \rangle$ in (186) as a shorthand for a partial derivative, however, we can also develop an interpretation for it by looking at the definitions of the dynamical zeta function (178) and the spectral determinant (62). In both series, the partial derivative with respect to s turns them into a sum weighted by the cycle periods; with this intuition, we define $\langle T \rangle$ as the 'mean cycle period'. We are now ready to present our numerical results and discuss their quality.

4.4.1 Numerical results

We constructed the spectral determinant (183) to different orders for two observables: phase velocity $\dot{\theta}$ and the leading Lyapunov exponent. Remember that Ω_p appearing in (182) is the integrated observable, so in order to obtain the moments of phase velocity and the leading Lyapunov exponent from (187) and (188), we respectively put in $\Omega_p = \theta_p$, the phase shift

Table 2: Cycle expansion estimates for the escape rate γ, average cycle period $\langle T\rangle$, Lyapunov exponent λ, average phase velocity $\langle\dot{\theta}\rangle$, and the diffusion coefficient D, using cycles up to length N in the golden mean approximation (181) of the symbolic dynamics.

N	γ	$\langle T\rangle$	λ	$\langle\dot{\theta}\rangle$	D
1	0.249829963	3.6415122	0.10834917	0.0222352	0.000000
2	-0.011597609	5.8967605	0.10302891	-0.1391709	0.143470
3	0.027446312	4.7271381	0.11849761	-0.1414933	0.168658
4	-0.004455525	6.2386572	0.10631066	-0.2141194	0.152201
5	0.000681027	5.8967424	0.11842700	-0.2120545	0.164757
6	0.000684898	5.8968762	0.11820050	-0.1986756	0.157124
7	0.000630426	5.9031596	0.11835159	-0.1997353	0.157345
8	0.000714870	5.8918832	0.11827581	-0.1982025	0.156001
9	0.000728657	5.8897511	0.11826873	-0.1982254	0.156091
10	0.000728070	5.8898549	0.11826788	-0.1982568	0.156217
11	0.000727891	5.8898903	0.11826778	-0.1982561	0.156218
12	0.000727889	5.8898908	0.11826780	-0.1982563	0.156220

of the prime cycle p, and $\Omega_p = \ln|\Lambda_{p,e}|$, the logarithm of its expanding Floquet multiplier of $\Lambda_{p,e}$.

In Sect. 4.1.5, we explained that SO(2) phase shifts correspond to the drifts in space. We define the corresponding diffusion coefficient as

$$D = \frac{1}{2d}\lim_{\tau\to\infty}\frac{1}{\tau}\langle\theta(\tau)^2 - \langle\theta(\tau)\rangle^2\rangle\,, \tag{189}$$

where $d = 1$ since the analogous physical space is one-dimensional.

Tables 2 and 3 respectively show the cycle averages of the escape rate γ, mean period $\langle T\rangle$, leading Lyapunov exponent λ, mean phase velocity $\langle\dot{\theta}\rangle$ and the diffusion coefficient D with and without the finite grammar approximation. In the latter, we input all the relative periodic orbits we have found into the expansion (182), whereas in the former, we discarded the cycles with symbol sequence '00'.

In Sect. 4.3.2, we motivated the finite grammar approximation by claiming that it would lead to faster convergence of dynamical averages due to the nearly exact shadowing combinations of the golden mean zeta function (181). This claim is supported by the data in Tables 2 and 3. Take, for example, the Lyapunov exponent. This converges to 7 digits for the 12^{th} order expansion when using the finite grammar approximation in Table 2, but only converges to 4 digits at this order in Table 3. Other observables compare similarly in terms of their convergence in both cases. Note, however, that the escape rate in Table 2 converges to $\gamma = 0.000727889$, whereas in Table 3 it gets smaller and smaller with an oscillatory behavior. This is due to the fact that in the finite grammar approximation, we threw out the part of attractor that corresponds to the cusp of the return map in Figure 10 (d) above the point cut by $\overline{001}$.

In order to compare with the cycle averages, we numerically estimated the leading Lyapunov exponent of the two-modes system using the method of Wolf *et al.* [119] This procedure was repeated 100 times for different initial conditions, yielding a numerical mean estimate of $\overline{\lambda} = 0.1198 \pm 0.0008$. While the finite grammar estimate $\lambda_{FG} = 0.1183$ is

Table 3: Cycle expansion estimates of the escape rate γ, average cycle period $\langle T \rangle$, Lyapunov exponent λ, average phase velocity $\langle \dot{\theta} \rangle$, and the diffusion coefficient D using all cycles found up to length N.

N	γ	$\langle T \rangle$	λ	$\langle \dot{\theta} \rangle$	D
1	0.249829963	3.6415122	0.10834917	0.0222352	0.000000
2	-0.011597609	5.8967605	0.10302891	-0.1391709	0.143470
3	0.022614694	4.8899587	0.13055574	-0.1594782	0.190922
4	-0.006065601	6.2482261	0.11086469	-0.2191881	0.157668
5	0.000912644	5.7771642	0.11812034	-0.2128347	0.168337
6	0.000262099	5.8364534	0.11948918	-0.2007615	0.160662
7	0.000017707	5.8638210	0.12058951	-0.2021046	0.160364
8	0.000113284	5.8511045	0.12028459	-0.2006143	0.159233
9	0.000064082	5.8587350	0.12045664	-0.2006756	0.158234
10	0.000093124	5.8536181	0.12035185	-0.2007018	0.158811
11	0.000153085	5.8417694	0.12014700	-0.2004520	0.158255
12	0.000135887	5.8455331	0.12019940	-0.2005299	0.158465

within 0.6% range of this value, the full cycle expansion agrees with the numerical estimate. This is not surprising since in the finite grammar approximation, we discard the most unstable cycles to obtain faster convergence, and so can expect a slight underestimate of the Lyapunov exponent.

4.5 Conclusions

In this chapter, we studied a simple dynamical system that exhibits chaos and is equivariant under SO(2) symmetry as the first application of first Fourier mode slice. Our presentation covers all steps that need to be taken in the study of equivariant systems: (1) reduction of symmetries, (2) understanding of qualitative dynamics on Poincaré maps, (3) finding exact coherent structures numerically using guesses from Poincaré maps, and (4) predicting dynamical averages using periodic orbit theory. Relative simplicity of the two-modes system's strange attractor allowed us to carry out steps (2-4) in a straightforward manner, and confirmed one of the main objectives of our approach: Relative periodic orbits can indeed be used to predict the long-time averages of observables in chaotic systems with continuous symmetries. Furthermore, improved convergence of cycle expansions within the finite grammar approximation of Sect. 4.3.2 demonstrated the strong relation between qualitative understanding of chaotic systems and quantitative predictions of their long term behavior.

CHAPTER V

KURAMOTO-SIVASHINSKY SYSTEM

In the previous chapter, we showed that the relative periodic orbits of a chaotic system with a continuous symmetry, can indeed be used to predict the long term behavior of the system. However, the four-dimensional two-modes system is very easy compared to the applications we have in mind and it also lacked the physical motivation for its study. Here, we take one step further, and as soon as we do, we face new difficulties.

Originally derived as a simplification of the complex Ginzburg-Landau equation [71] and in the study of flame fronts [103], the Kuramoto-Sivashinsky equation is perhaps the simplest spatially extended dynamical system that exhibits spatiotemporal chaos. Similar in form to the Navier-Stokes equation, but much easier computationally, the Kuramoto-Sivashinsky partial differential equation ([**pde??**]) is a convenient sandbox for developing intuition about turbulence [60].

In one space dimension with periodic boundary condition, the Kuramoto-Sivashinsky equation is equivariant under both discrete reflection and continuous translations. In order to avoid dealing with complications due to the continuous symmetry, a number of earlier papers [18, 72, 91–93] study the Kuramoto-Sivashinsky equation within the flow-invariant subspace of solutions antisymmetric under the reflection. However, such restrictions to flow-invariant subspaces miss the physics of the problem: any symmetry invariant subspace is of zero measure in the full state space, so a generic turbulent trajectory explores the state space *outside* of it. Lacking continuous-symmetry reduction schemes, earlier papers on the geometry of the Kuramoto-Sivashinsky flow in the full state space were restricted to the study of the smallest invariant structures: equilibria [49], their invariant stable/unstable manifolds, their heteroclinic connections [22], and their bifurcations under variations of the domain size [3, 68].

In this chapter, we are going to study the state space geometry of Kuramoto-Sivashinsky system in the symmetry reduced representation, which will enable us to study the invariant manifolds of the relative equilibria and relative periodic orbits. We begin by introducing the Kuramoto-Sivashinsky system.

5.1 Kuramoto-Sivashinsky system and its symmetries

We study the Kuramoto-Sivashinsky equation in one space dimension

$$u_\tau = -\tfrac{1}{2}(u^2)_x - u_{xx} - u_{xxxx}\,, \tag{190}$$

with periodic boundary condition $u(x,\tau) = u(x+L,\tau)$. The real field $u(x,\tau)$ is the "flame front" velocity [103]. The domain size L is the bifurcation parameter for the system, which exhibits spatiotemporal chaos for sufficiently large L: see Figure 13 (e) for a typical spatiotemporally chaotic trajectory of the system at $L = 22$.

We discretize the Kuramoto-Sivashinsky system by Fourier expanding the field $u(x,\tau) = \sum_k \tilde{u}_k(\tau) e^{iq_k x}$, and expressing (190) in terms of Fourier modes as an infinite set of ordinary

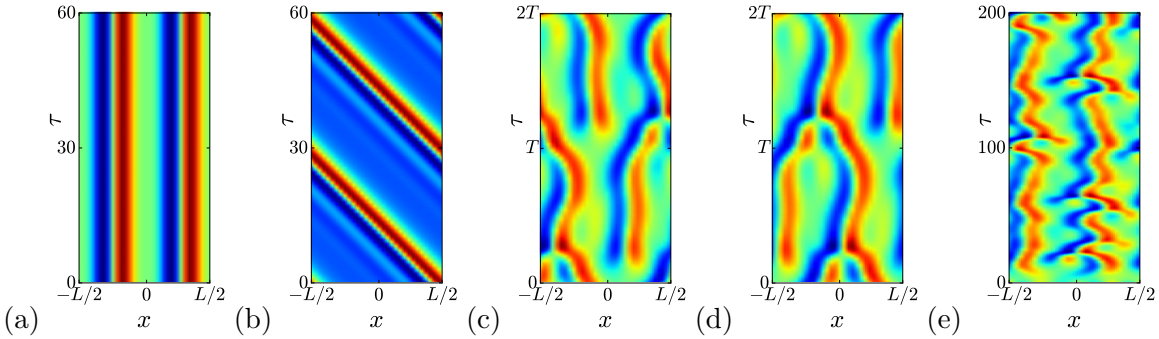

Figure 13: Examples of exact coherent structures in the Kuramoto-Sivashinsky system and the ergodic flow visualized as the color coded amplitude of the scalar field $u(x,\tau)$: (a) Equilibrium E_1, (b) Relative equilibrium TW_1, (c) Pre-periodic orbit with period $T = 32.4$, (d) Relative periodic orbit with period $T = 33.5$. (e) Ergodic flow. Horizontal and vertical axes correspond to space and time respectively. System size $L = 22$. The exact coherent structures and their labels are taken from ref. [22].

differential equations ([**ode??**]s)

$$\dot{\tilde{u}}_k = (q_k^2 - q_k^4)\,\tilde{u}_k - i\frac{q_k}{2}\sum_{m=-\infty}^{+\infty}\tilde{u}_m\tilde{u}_{k-m}\,, \quad q_k = \frac{2\pi k}{L}\,. \tag{191}$$

Kuramoto-Sivashinsky equation is *Galilean invariant*: if $u(x,\tau)$ is a solution, then $v + u(x - v\tau, \tau)$, with v an arbitrary constant velocity, is also a solution. In the Fourier representation (191), the Galilean invariance implies that the zeroth Fourier mode $\tilde{u}_0$ is decoupled from the rest and time-invariant. Hence, we set $\tilde{u}_0 = 0$[1] and exclude $\tilde{u}_0$ from the state space and represent a Kuramoto-Sivashinsky state $u = u(x,\tau)$ by the Fourier series truncated at $k = N$, i.e., a $2N$-dimensional real valued state space vector (69). One can rewrite (191) in terms of this real valued state space vector, and express the truncated set of equations compactly as

$$\dot{a} = v(a)\,. \tag{192}$$

In our numerical work we use a pseudo-spectral formulation of (192), as described in Appendix C.

Spatial translations $u(x,\tau) \to u(x + \delta x, \tau)$ correspond to SO(2) rotations $a \to g(\theta)\,a$ in the Kuramoto-Sivashinsky state space, with the matrix representation (70). The Kuramoto-Sivashinsky dynamics commutes with the action of (70), as can be verified by checking that (192) satisfies the equivariance relation (73). By the translation symmetry of the Kuramoto-Sivashinsky, each solution of [**pde??**] (190) has infinitely many dynamically equivalent copies that can be obtained by translations (70). Hence, Kuramoto-Sivashinsky system has relative exact coherent structures such as relative equilibria (79) and relative periodic orbits (83), examples of which are visualized in Figure 13 (b) and (d), respectively.

The Kuramoto-Sivashinsky equation (190) has no preferred direction, and is thus also equivariant under the *reflection* symmetry $u(x,\tau) \to -u(-x,\tau)$: for each solution drifting left, there is a reflection-equivalent solution which drifts right. In terms of Fourier components, the reflection σ acts as complex conjugation followed by a negation, whose action

[1] We do not loose generality by this choice since each solution with nonzero mean velocity v can be obtained from zero mean velocity ($\tilde{u}_0 = 0$) solution by transforming to the moving frame $x' = x - v\tau$.

on vectors in state space (69) is represented by the diagonal matrix which flips the real components b_i to $-b_i$,

$$\sigma = \mathrm{diag}\,[-1,\ 1,\ -1,\ 1,\ \ldots,\ -1,\ 1]\ . \tag{193}$$

Due to this reflection symmetry, the Kuramoto-Sivashinsky system also can also have strictly non-drifting equilibria and (pre-)periodic orbits. An *equilibrium* is a stationary solution $a_{eq}(\tau) = a_{eq}(0)$. A *periodic orbit* p is periodic with period T_p, $a_p(0) = a(T_p)$, and a *pre-periodic orbit* is a relative periodic orbit

$$a_{ppo}(0) = \sigma\, a_{ppo}(T_p) \tag{194}$$

which closes in the full state space after the second repeat, hence we refer to it as 'pre-periodic'.

In Figure 13 (a) we show equilibrium E_1 of Kuramoto-Sivashinsky equation (so labelled in ref. [22]). If we were to reflect Figure 13 (a) with respect to $x = 0$ line, and then interchange red and blue colors, we would obtain the same solution; all equilibria belong to the flow-invariant subspace of solutions invariant under the reflection symmetry of the Kuramoto-Sivashinsky equation. Figure 13 (b) shows a pre-periodic solution of the Kuramoto-Sivashinsky system: The dynamics of the second period can be obtained from the first one by reflecting it. Both equilibria and pre-periodic orbits have infinitely many copies that can be obtained by continuous translations, symmetric across the shifted symmetry line, $g(\theta)\sigma g(-\theta)$. Due to non-commutativity of reflection σ and translations $g(\theta)$, ($\sigma\, g(\theta) = -g(\theta)\,\sigma$, or, in terms of the generator of translations, the reflection reverses the direction of the translation, $\sigma\, T = -T\,\sigma$). Let $f^\tau(a)$ denote the finite time flow mapping induced by (192) and a_{ppo} belong to a pre-periodic orbit defined by (194). Then the dynamics of the shifted point $a'_{ppo} = g(\theta)\, a_{ppo}$ satisfies

$$f^{T_p}(a'_{ppo}) = g(\theta)\sigma g(-\theta)\, a'_{ppo}\ .$$

In contrast, a relative periodic orbit (83) also has a distinct reflected copy $a'_{rpo} = \sigma a_{rpo}$ with reversed phase shift:

$$a'_{rpo}(0) = g(\theta_p)\, a'_{rpo}(T_p)\ .$$

In order to carry out our analysis, we must first eliminate all these degeneracies. This we do by symmetry reduction, which we describe next.

5.2 Continuous symmetry reduction

Similar to the two-modes system of the previous chapter, we reduce the continuous SO(2) symmetry of the Kuramoto-Sivashinsky system by the choosing the first Fourier mode slice template $\hat{a}' = (1, 0, 0, \ldots, 0)^T$ (100), which implies the symmetry reduced dynamics

$$\hat{v}(\hat{a}) = v(\hat{a}) - \frac{\dot{c}_1}{\hat{b}_1} t(\hat{a}) \tag{195}$$

in the symmetry reduced state space

$$\hat{a} = (\hat{b}_1, 0, \hat{b}_2, \hat{c}_2, \ldots \hat{b}_N, \hat{c}_N)\ . \tag{196}$$

as we described in Sect. 3.3.3. The two-modes system had a flow invariant subspace $z_1 = 0$, $z_2 \neq 0$ (144), which prevented the flow from entering the slice border $x_1 = 0$ (97); hence

the first Fourier mode slice was guaranteed to be valid for generic trajectories. We have no such guarantee here, and in fact, when we reduce the SO(2) symmetry via first Fourier mode slice, the trajectories appear to be discontinuous.

In Sect. 3.3.3, we showed that the reduced velocity field (102) is singular if the amplitude of the first Fourier mode $\hat{b}_1$ vanishes and we proposed that this singularity can be regularized by rewriting symmetry reduced dynamics in terms of a rescaled slice time (103). As illustrated in Figure 14 for a traveling wave and an relative periodic orbit of the Kuramoto-Sivashinsky system at $L = 22$, apparent fast jumps of the symmetry reduced flow are well-resolved when the dynamics is sampled in slice time. Note also that when the symmetry is reduced, the relative equilibrium and the relative periodic orbit respectively becomes an equilibrium and a periodic orbit as expected.

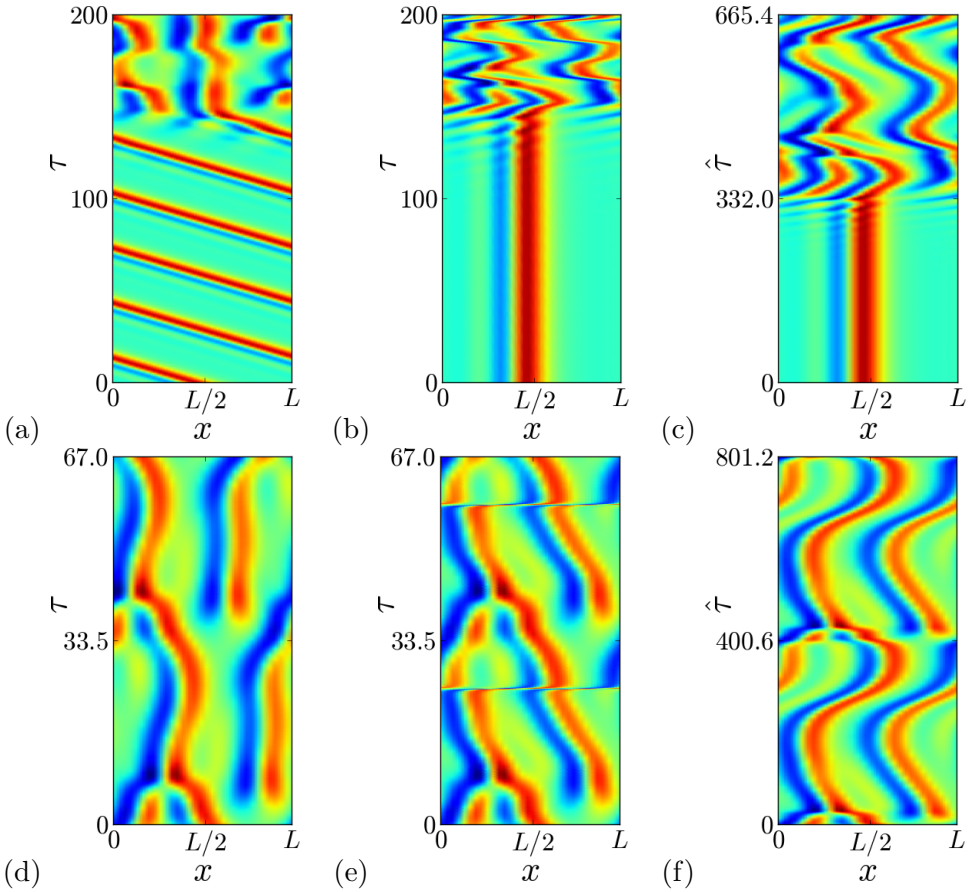

Figure 14: Traveling wave TW_1 with phase velocity $c = 0.737$: (a) the full state space solution, (b) symmetry-reduced solution with respect to the lab time, and (c) symmetry-reduced solution with respect to the slice time. Relative periodic orbit $T_p = 33.50$: (d) the full state space solution, (e) symmetry-reduced solution with respect to the lab time, and (f) symmetry-reduced solution with respect to the slice time. The exact coherent structures and their labels are taken from ref. [22].

5.2.1 State space visualization

While the physical space visualizations of spatiotemporal chaos such as Figure 13 and Figure 14 are intuitive, they do not tell much about the general organization of solutions in the state space. It is not obvious how to effectively visualize the infinite-dimensional state space of partial differential equations. Gibson *et al.* [45] addressed this problem for Plane-Couette flow, where they captured dynamics within the neighborhoods of equilibria by constructing projection frames from their stability eigenvectors. In this section, we are going to show that this approach can be extended to the relative equilibria within the first Fourier mode slice.

The exact coherent structure that we are going to study is TW_1 (Figure 14 (a-c)), found in ref. [22] for the system size $L = 22$. We compute the linear stability properties of TW_1 by computing eigenvalues and eigenvectors of $\hat{A}(\hat{a}_{\mathrm{TW}_1})$ (107). TW_1 has 4 stability eigenvalues with positive real parts

$$\lambda_{1,2} = 0.11562 \pm i0.81729\,, \quad \lambda_{3,4} = 0.03366 \pm i0.41891\,, \tag{197}$$

which renders its unstable manifold four-dimensional. However, since the real part of λ_1 is 3.4 times bigger than that of λ_3, we observed that the local expansion of dynamics nearby TW_1 is exponentially dominated in the directions of the stability eigenvector V_1 corresponding to λ_1. Complex eigenvalue λ_1 with positive real part tells us that the dynamics in the hyperplane spanned by real and imaginary parts of V_1 has spiral-out behavior within the linear approximation. Unstable manifolds of fixed points in nonlinear systems are in general curved objects, that are not confined to this hyperplane. However, Hartman-Grobman theorem [50] tells us that the linear and nonlinear unstable manifolds of a hyperbolic fixed point are topologically conjugate to each other, that is one can be smoothly deformed to the other. Furthermore, real unstable manifold converges to its linear approximation as one gets closer and closer to the fixed point. Therefore, if we start trajectories that cover the linear unstable manifold of the fixed point in close proximity to it, we expect to numerically resolve its real unstable manifold by integrating these trajectories forward in time. Let ϵ be a small number, n be an integer, $\mu_1 = \mathrm{Re}\,\lambda_1$, $\omega_1 = \mathrm{Im}\,\lambda_1$, and $\hat{e}_1 = \mathrm{Re}\,V_1$, perturbations

$$\hat{a}(\delta) = \hat{a}_{\mathrm{TW}_1} + \epsilon\, e^{\delta 2\pi\mu_1/\omega_1}\hat{e}_1\,, \quad \text{where} \quad \delta \in [0, 1)\,, \tag{198}$$

cover the two-dimensional subspace of the four-dimensional unstable manifold of TW_1 to the linear approximation, since after $2\pi/\omega_1$ (one return), $\hat{a}(0)$ comes to the initial location of $\hat{a}(1)$. We set $\epsilon = 10^{-6}$, took 20 equidistant values in $[0, 1)$ for δ and integrated these trajectories for $\tau_F = 115$ within the slice and the full state space and plotted the outcomes in Figure 15. The coordinate axes are projections (e_1, e_2, e_3) onto three orthonormal vectors $(\hat{e}_1, \hat{e}_2, \hat{e}_3)$ constructed from $\mathrm{Re}\,V_1$, $\mathrm{Im}\,V_1$, and $\mathrm{Re}\,V_3$ via Gram-Schmidt orthogonalization.

It is clear from Figure 15 that without continuous symmetry reduction, dynamics nearby TW_1 is dominated by the drifts in the symmetry direction, and thus the continuous symmetry reduction is crucial to extract the physical (symmetry invariant) part of the unstable manifold.

While the first Fourier mode slice eliminates infinitely many symmetry copies of the solutions, within the slice, we still have a reflection copy for each solution that is not invariant under it. We reduce this symmetry in the next section.

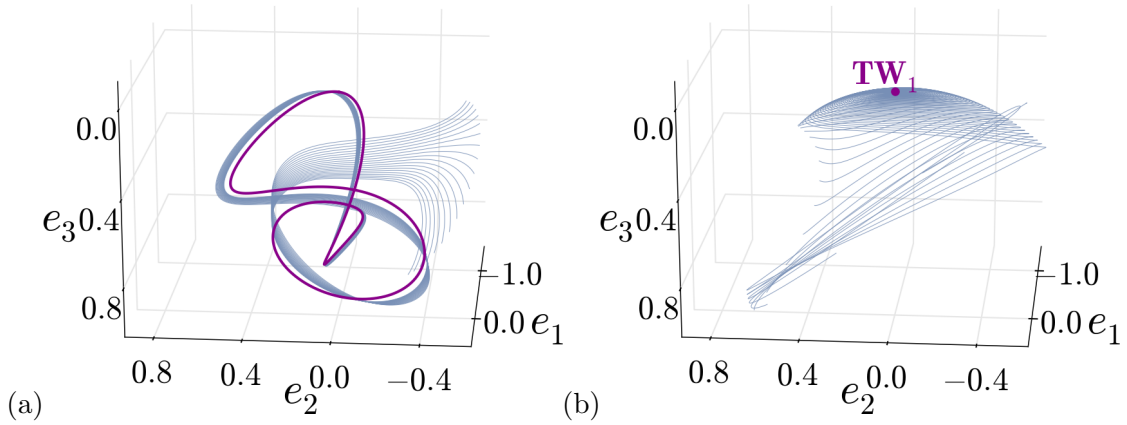

Figure 15: Kuramoto-Sivashinsky system (a) in the full state space: Group orbit (also the time orbit) of TW_1 (magenta) and its unstable manifold (blue) traced out by integrating nearby points given by (198) (b) In the symmetry reduced state space TW_1 is reduced to a single point, and the unstable manifold is a smooth 2D surface.

5.3 Discrete symmetry reduction

Our next challenge is to devise a transformation from (196) to discrete-symmetry reduced coordinates, where the equivariance under reflection is also reduced. Consider the action of reflection on the symmetry-reduced state space. In general, a slice is an arbitrarily oriented hyperplane, and action of the reflection σ can be rather complicated: it maps points within the slice hyperplane into points outside of it, which then have to be rotated into the slice.

Fortunately, the action of σ on the first Fourier mode slice is particularly simple. Action $\sigma\hat{a}$ of (193) on (196) flips the sign of the first element, i.e., makes the phase of the first Fourier mode π. Rotating back into the slice by (98), we find that the reflection within the first Fourier mode slice acts by alternating the signs of even (real part) and odd (imaginary part) Fourier modes:

$$\begin{aligned} \hat{\sigma} &= g(-\pi)\sigma \\ &= \mathrm{diag}\,[\,1,\,-1,\,-1,\,1,\,1,\,-1,\,-1,\,1,\,1,\,\ldots]\,. \end{aligned} \tag{199}$$

The action on the slice coordinates (where we for brevity omit all terms whose signs do not change under reflection) is

$$\hat{\sigma}(\hat{b}_2, \hat{c}_3, \hat{b}_4, \hat{c}_5, \hat{b}_6, \hat{c}_7, \ldots) = (-\hat{b}_2, -\hat{c}_3, -\hat{b}_4, -\hat{c}_5, -\hat{b}_6, -\hat{c}_7, \ldots)\,, \tag{200}$$

Our goal is to find a transformation from (196) to some new, reflection-invariant coordinates. We could declare a half of the symmetry-reduced state space to be a 'fundamental domain' [24], with segments of orbits that exit it brought back by reflection, but such symmetry reduction makes orbits appear discontinuous and hard to visualize.

Miranda and Stone [46, 80] reduction of the C_2 symmetry of the Lorenz system (or the 'the doubled-polar angle coordinates' of ref. [24]) into a smooth flow by a nonlinear coordinate transformation into an invariant polynomial basis suggests our next step. Squaring (or taking absolute value of) each sign-flipping coordinate in (200) is not an option, since such coordinates would be invariant under every individual sign change of these coordinates, and that is not a symmetry of the system. We are allowed to impose *only one* condition to

reduce the 2-element orbit of the discrete reflections subgroup of O(2). Here is our proposal: in order to achieve the desired 2−to−1 symmetry reduction, we construct the first coordinate from squares, and 'twine' the successive sign-flipping terms into a quadratic invariant polynomial basis set

$$\begin{aligned}&(p_2, p_3, p_4, p_5, \ldots)\\ &= (\hat{b}_2^2 - \hat{c}_3^2,\ \hat{b}_2\hat{c}_3,\ \hat{b}_4\hat{c}_3,\ \hat{b}_4\hat{c}_5,\ \ldots)\,.\end{aligned} \tag{201}$$

The original coordinates can be recovered recursively by the 1−to−2 inverse transformation

$$\begin{aligned} b_2 &= \pm\sqrt{\frac{p_2 + \sqrt{p_2^2 + 4p_3^2}}{2}} \\ c_3 &= p_3/b_2\,, \quad b_4 = p_4/c_3\,, \quad c_5 = p_5/b_4\,, \quad \cdots\,. \end{aligned}$$

To summarize: we first reduce the group orbits generated by the continuous SO(2) symmetry subgroup by implementing the first Fourier mode slice (95), and then reduce the group orbits of the discrete 2-element reflection subgroup by replacing the sign-changing coordinates (200) with the invariant polynomials (201). The final O(2) symmetry-reduced coordinates are

$$\tilde{a} = (\hat{b}_1, 0, \hat{b}_2^2 - \hat{c}_3^2, \hat{c}_2, \hat{b}_3, \hat{b}_2\hat{c}_3, \hat{b}_4\hat{c}_3, \hat{c}_4, \hat{b}_5, \ldots)\,. \tag{202}$$

Here pairs of orbits related by reflection σ are mapped into a single orbit, and $\hat{c}_1$ is identically set to 0 by continuous symmetry reduction, thus the symmetry-reduced state space has one dimension less than the full state space.

5.4 Kuramoto-Sivashinsky system at $L = 22$

In our initial studies of the Kuramoto-Sivashinsky system, we followed the work of ref. [22], where authors succeeded to find over 30000 relative periodic orbits of the Kuramoto-Sivashinsky system as well as 3 equilibria and 2 traveling waves at $L = 22.0$. In ref. [22], authors also find heteroclinic connections between equilibria by visualizing their unstable manifolds. With the symmetry reduction, we were able to study unstable manifolds of relative equilibria as we illustrated in Figure 15, however, we observed that these manifolds directly connect to the strange attractor. Furthermore, we have also searched for recurrent dynamics in these neighborhoods by studying them on local Poincaré sections, but we have not succeeded identifying such locally low dimensional dynamics.

In order to develop a better intuition about the problem, we decided to try a data driven approach for visualization of global dynamics. For this purpose, we adopted principal component analysis (**[pca??]**), a statistical method for extracting directions of the largest variations of a given data set.

PCA is widely used and has different names in different fields. In turbulence studies, it is usually referred to as "proper orthogonal decomposition" (POD) [60] or "Karhunen-Loève expansion" [96]. Here, we preferred to use the term PCA, because our application of the method is different from the general use in turbulence literature in one important aspect: POD basis is generally defined in L^2-space of the turbulent velocity field, where the L^2-norm of the velocity field (or l^2-norm of its Fourier modes) is the "energy norm". In our symmetry-reduced state space (202), while we still have entire physical information of the system, l^2-norm no longer corresponds to the energy of the state. We treat the ergodic flow in (202) as a statistical sample set, and hence we adopted the common terminology

in statistics. We refer the reader to ref. [60] for an introduction to POD in the turbulence context; for a general introduction to PCA, see ref. [118].

In order to obtain principal components P_i, we first generate the data set from a very long simulation ($t_{Final} = 2 \times 10^5$) of the Kuramoto-Sivashinsky equation sampled at every 0.1 time units, and transform the outcome to the reduced state space coordinates (202). P_i are the normalized eigenvectors of empirical covariance matrix $X^T X$, where X is the data matrix. Rows of X are the samples $a_k - \langle a \rangle$, where a_k are the data from the long simulation and $\langle a \rangle$ is their empirical mean. In computations, these eigenvectors are found by singular value decomposition

$$X = U \Sigma W^T , \tag{203}$$

where U is a unitary matrix, Σ is rectangular diagonal with singular values σ_i of X and columns of W are the principal components P_i. We utilized `pca` function of `MATLAB` for this calculation. Principal components P_i are ordered by decreasing principal component variances $\sigma_i^2 > \sigma_{i-1}^2, i = 1, 2, 3, \ldots$ Figure 16 (a) shows three projections of the ergodic data (gray) and 10 periodic orbits of the Kuramoto-Sivashinsky system onto the three leading principal components.

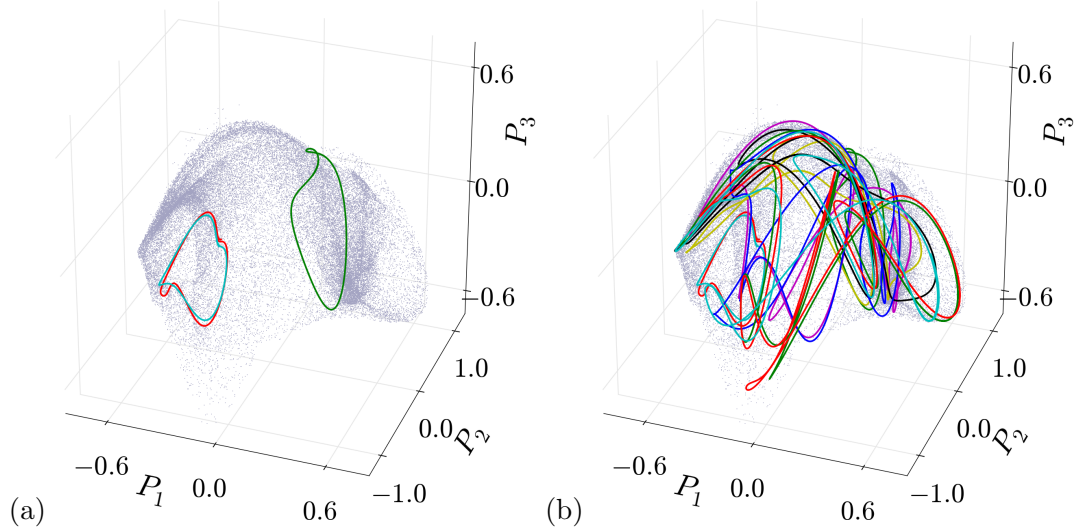

Figure 16: Samples (separated equally in time) from a long simulation (gray) with (a) the two shortest pre-perodic orbits (green and cyan) and the shortest relative periodic orbit(red) of the Kuramoto-Sivashinsky system, (b) the shortest 10 relative periodic orbits of the Kuramoto-Sivashinsky system, projected onto leading three principal components.

In Figure 16 (a), we show the two shortest pre-periodic orbits (green and cyan) and one relative periodic orbit (red) of the Kuramoto-Sivashinsky system along with the samples from ergodic trajectory (grey dots). Note the overlap of RPO_1 (red) and PPO_2 (cyan) in Figure 16 (a); this is an example of how symmetry reduction reveals relations between trajectories, which are otherwise very hard to detect. In Figure 16 (b), we show the shortest 10 periodic orbits (6 pre-periodic and 4 relative periodic orbitin full state space) of the Kuramoto-Sivashinsky system, which appear to be "filling out" the ergodic cloud.

Variations of the density of ergodic data in Figure 16 already reveal some qualitative properties of the chaotic attractor of Kuramoto-Sivashinsky system. In order to extract more detailed information, we construct a Poincaré section from the hyperplane condition

and the directional constraint

$$\langle \tilde{a} - \langle a \rangle, P_3 \rangle = 0 \quad \text{and} \quad \langle \tilde{v}(\tilde{a}), P_3 \rangle > 0 \,. \tag{204}$$

Figure 17 shows intersections of 479 periodic orbits (blue) and an ergodic trajectory (green) with the Poincaré section (204), projected onto the (P_1, P_2) plane. The blue and green dots appear to populate the same overlapping structures, indicating a surprisingly thin strange attractor whose "backbone' is formed by the relative periodic orbits.

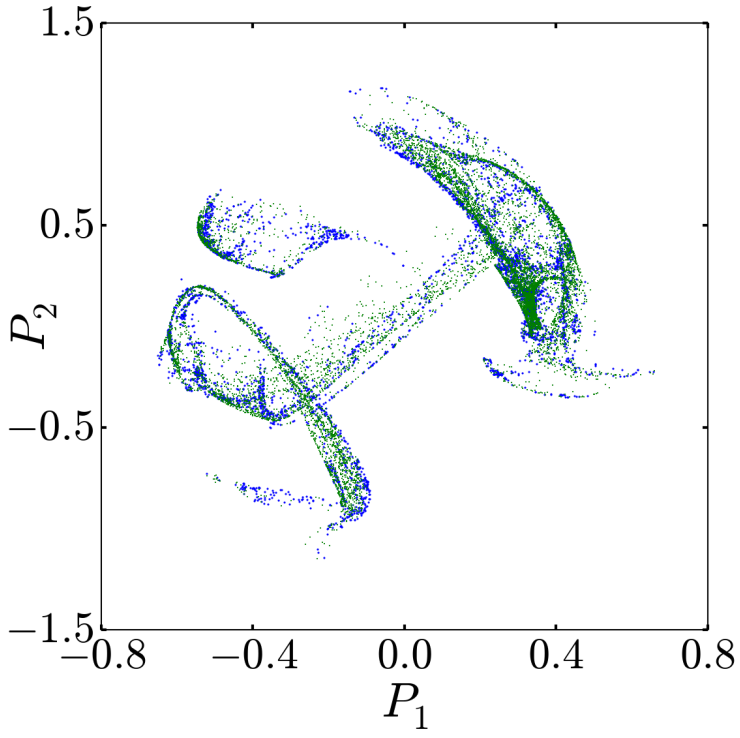

Figure 17: Intersections of the long ergodic trajectory (green) and 479 periodic orbits (blue) with the Poincaré section which contains the origin of the **[pca??]** coordinates (empirical mean) and is parallel to (P_1, P_2) plane.

Strikingly similar structures of ergodic trajectories and periodic orbits on the Poincaré section Figure 17 motivated us to study unstable manifolds of the periodic orbits. However, we have not succeeded in identifying one important relative periodic orbit (out of 479!) whose invariant manifolds form the shape of this attractor. For this reason, we decided to first investigate the system by varying its size and study its bifurcations, in order to see whether one of these orbits plays the key role in shaping the strange attractor.

5.5 Transition to chaos via torus breakdown

We now investigate the transition to chaos in the neighborhood of a short Kuramoto-Sivashinsky pre-periodic orbit, focusing on the system sizes $L \in [21.0, 21.48]$. Our method yields a symmetry-reduced velocity field $\tilde{v}(\tilde{a}) = \dot{\tilde{a}}$ and a time-forward flow $\tilde{f}^\tau(\tilde{a}(0)) = \tilde{a}(\tau)$ in the symmetry-reduced state space (202). Although we can obtain $\tilde{v}(\tilde{a})$ by chain rule, we find its numerical integration unstable, hence in practice we obtain $\tilde{v}(\tilde{a})$ and $\tilde{f}^\tau(\tilde{a})$ from

the first Fourier mode slice by applying the appropriate Jacobian matrices, as described in Appendix C.

At $L = 21.0$, we found that the Kuramoto-Sivashinsky system has a stable periodic orbit p_0 (pre-periodic in full state space), which satisfies $\tilde{a}_{p_0} = \tilde{f}^{T_{p_0}}(\tilde{a}_{p_0})$ for any point on the periodic orbit p_0. We have also observed that trajectories of random (outside an invariant subspace) initial conditions converge to this orbit after sufficiently long time; indicating that p_0 has a large basin of attraction at $L = 21.0$. Linear stability of a periodic orbit is described by the Floquet multipliers Λ_i and Floquet vectors $\tilde{V}_i$ which are the eigenvalues and eigenvectors of the Jacobian matrix $\tilde{J}_p$ of the time-forward flow $\tilde{f}^{T_p}(\tilde{a}_p)$

$$\tilde{J}_p \tilde{V}_i = \Lambda_i \tilde{V}_i \,.$$

Each periodic orbit has at least one Floquet multiplier $\Lambda_v = 1$ corresponding to the velocity field direction. When $L < 21.22$, all other Floquet multipliers of p_0 has absolute values less than 1. At $L \approx 21.22$, leading Floquet multiplier Λ_1 crosses the unit circle, and the corresponding eigenplane spanned by the real and imaginary parts of $\tilde{V}_1$ starts to have 'spiral out' dynamics that connects to a 2-torus, as illustrated in Figure 18 (b). In Figure 18 and the rest of the state space projections of this paper, projection bases are constructed as follows: Real and imaginary parts of the Floquet vector $\tilde{V}_1$ define an ellipse $\mathrm{Re}\,[\tilde{V}_1]\cos\phi + \mathrm{Im}\,[\tilde{V}_1]\sin\phi$ in the neighborhood of $\tilde{a}_{p_0}$, and we pick the principal axes of this ellipse as the first two projection-subspace spanning vectors. As the third vector we take the velocity field $\tilde{v}(\tilde{a}_{p_0})$, and the projection bases (e_1, e_2, e_3) are found by orthonormalization of these vectors via the Gram-Schmidt procedure. All state space projections are centered on $\tilde{a}_{p_0}$, i.e., $\tilde{a}_{p_0}$ is the origin of all Poincaré section projections.

In order to study dynamics within the neighborhood of p_0, we define a Poincaré section as the hyperplane of points in an open neighborhood of $\tilde{a}_{p_0}$, orthogonal to the tangent $\tilde{v}(\tilde{a}_{p_0})$ of the orbit at the intersection point,

$$\langle \tilde{a} - \tilde{a}_{p_0}, \tilde{v}(\tilde{a}_{p_0}) \rangle = 0 \quad \text{and} \quad ||\tilde{a} - \tilde{a}_{p_0}|| < \alpha \,, \tag{205}$$

where $||.||$ denotes the Euclidean (or $L2$) norm, and the threshold α is empirically set to $\alpha = 0.5$ throughout. From here on, we study the discrete time dynamics induced by the flow on this hyperplane, as visualized in Figure 18 (a). As an example, we follow a single trajectory starting from $\tilde{a}_{p_0} + 10^{-1}\mathrm{Re}\,[\tilde{V}_1]$ as it connects to the 2-torus surrounding the periodic orbit in Figure 18 (b). For system size $L = 21.25$ the magnitude of the complex unstable Floquet multiplier pair is nearly marginal, $|\Lambda_{1,2}| = 1.00636$, hence the spiral-out is very slow.

5.5.1 Interlude: Discrete time dynamical systems

As illustrated in Figure 18, continuous time flow in the state space induces discrete time dynamics on the Poincaré section. In order to be able to explain the unstable manifold calculations of the next section, we need to cover some basic results of the discrete time linear dynamical systems. For our purposes here, it is sufficient to describe the 1 and 2-dimensional cases. An autonomous discrete time linear system is defined by a difference equation

$$a[n+1] = A a[n] \,, \tag{206}$$

where A is a matrix, a is a state space vector and n is the integer time variable written in square brackets to imply its discreteness. For an initial condition $a[0] = a_0$, the solution is

$$a[n] = A^n a_0 \tag{207}$$

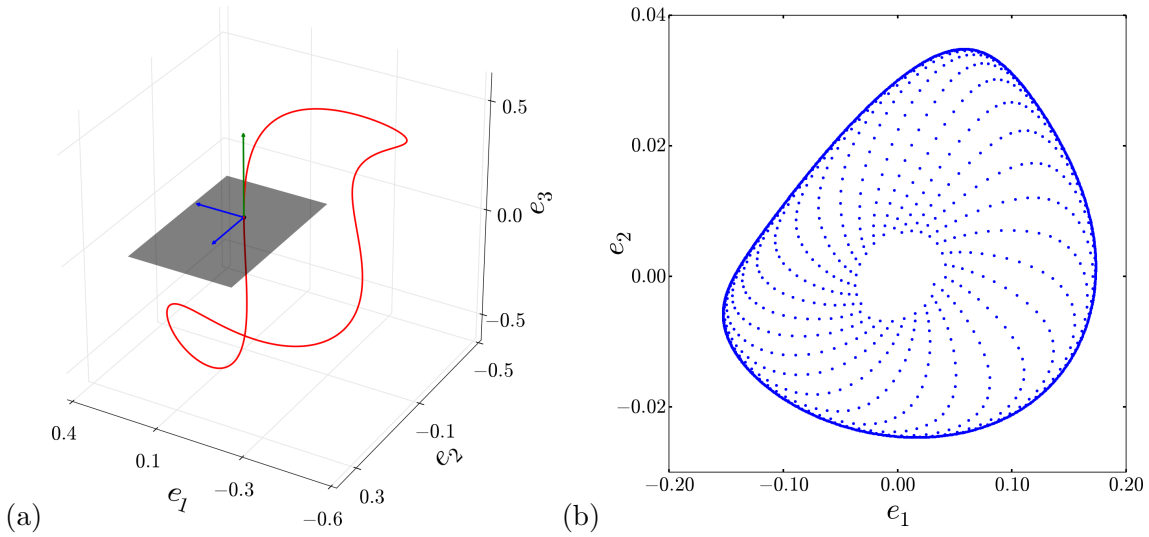

Figure 18: (a) Pre-periodic orbit p_0 (red), its velocity field $\tilde{v}(\tilde{a}_{p_0})$ at the starting point (green), orthogonal vectors that span the eigenplane corresponding to the leading Floquet vectors (blue) and the Poincaré section hyperplane (gray). (b) Spiral-out dynamics of a single trajectory in the Poincaré section projected onto (e_1, e_2) plane, system size $L = 21.25$.

and if the system is one-dimensional, then (207) is all one needs.

Now let us assume that A is 2×2, has complex eigenvalue/eigenvector pairs $\Lambda_{1,2} = |\Lambda_1| e^{\pm i \arg \Lambda_1}$ and $V_{1,2} = \mathrm{Re}\, V_1 \pm i \mathrm{Im}\, V_1$ and V_i are normalized, i.e. $|\mathrm{Re}\, V_1|^2 + |\mathrm{Im}\, V_1|^2 = 1$.

Since, $\mathrm{Re}\, V_1$ and $\mathrm{Im}\, V_1$ are linearly independent, an initial condition a_0 in the state space can be written as

$$a_0 = c_1 \mathrm{Re}\, V_1 + c_2 \mathrm{Im}\, V_1 \,, \tag{208}$$

and the corresponding solution is

$$\begin{aligned}
a[n] &= A^n a_0 \\
&= A^n \frac{c_1}{2} (V_1 + V_2) + A^n \frac{c_2}{2} (V_1 - V_2) \\
&= \frac{c_1 |\Lambda_1|^n}{2} \left(e^{in \arg \Lambda_1} V_1 + e^{-in \arg \Lambda_1} V_2 \right) + \frac{c_2 |\Lambda_1|^n}{2i} \left(e^{in \arg \Lambda_1} V_1 - e^{-in \arg \Lambda_1} V_2 \right) \,, \\
&= \frac{c_1 |\Lambda_1|^n}{2} \left[(V_1 + V_2) \cos(n \arg \Lambda_1) + i (V_1 - V_2) \sin(n \arg \Lambda_1) \right] \\
&\quad + \frac{c_2 |\Lambda_1|^n}{2i} \left[(V_1 - V_2) \cos(n \arg \Lambda_1) + i (V_1 + V_2) \sin(n \arg \Lambda_1) \right] \,, \\
&= c_1 |\Lambda_1|^n [\mathrm{Re}\, V_1 \cos(n \arg \Lambda_1) - \mathrm{Im}\, V_1 \sin(n \arg \Lambda_1)] \\
&\quad + c_2 |\Lambda_1|^n [\mathrm{Re}\, V_1 \sin(n \arg \Lambda_1) + \mathrm{Im}\, V_1 \cos(n \arg \Lambda_1)] \,.
\end{aligned} \tag{209}$$

It is instructive to re-express (209) compactly by defining a matrix $W = [\mathrm{Re}\, V_1, \mathrm{Im}\, V_1]$ with real and imaginary parts of V_1 on its columns, and a coefficient vector $c = (c_1, c_2)^T$. Then the solution (209) can be written compactly as

$$a[n] = |\Lambda_1|^n W R(-n \arg \Lambda_1) c \,, \tag{210}$$

where $R(\theta)$ is the 2×2 rotation matrix (71). Without loss of generality, we can also define $c^{(1)} = (1, 0)^T$ and express $c = r R(\theta) c^{(1)}$ and rewrite (210) as

$$a[n] = |\Lambda_1|^n r W R(\theta - n \arg \Lambda_1) c^{(1)} \,. \tag{211}$$

While $\mathrm{Re}\, V_1$ and $\mathrm{Im}\, V_1$ are linearly independent, they are not necessarily orthogonal. Hence, (211) describes elliptic trajectories, spiraling or steady, depending on $|\Lambda_1|$.

5.5.2 Unstable manifolds of periodic orbits

We are now ready to compute two-dimensional unstable manifold of p_0 on the Poincaré section (205). Assume that $\delta\tilde{a}(0)$ is a small perturbation to $\tilde{a}_{p_0}$ that lies in the plane spanned by $(\mathrm{Re}\,[\tilde{V}_1], \mathrm{Im}\,[\tilde{V}_1])$. As we explained in the previous section, we can express this initial condition as

$$\delta\tilde{a}(0) = \delta r W R(\theta) c^{(1)}\,, \tag{212}$$

where $W = [\mathrm{Re}\,[\tilde{V}_1], \mathrm{Im}\,[\tilde{V}_1]]$ has real and imaginary parts of the Floquet vector $\tilde{V}_1$ on its columns and δr is the magnitude of small perturbation. In the linear approximation, discrete time dynamics $\delta\tilde{a}(nT_{p_0})$ is given by

$$\delta\tilde{a}(nT_{p_0}) = |\Lambda_1|^n \delta r W R(\theta - n \arg\Lambda_1) c^{(1)}\,, \tag{213}$$

which can then be projected onto the Poincaré section (205) by acting from the left with the projection operator

$$\mathbb{P} = \mathbf{1} - \frac{\tilde{v}(\tilde{a}_{p_0}) \otimes \tilde{v}(\tilde{a}_{p_0})}{||\tilde{v}(\tilde{a}_{p_0})||^2}\,,$$

where $\otimes$ denotes the outer product. Defining $\tilde{a}_{\mathcal{P}} \equiv \mathbb{P}\tilde{a}$, discrete time dynamics of a perturbation $\delta\tilde{a}_{\mathcal{P}}$ in the Poincaré section is given by

$$\delta\tilde{a}_{\mathcal{P}}[n] = |\Lambda_1|^n \delta r W_{\mathcal{P}} R(\theta - n \arg\Lambda_1) c^{(1)}\,, \tag{214}$$

where $W_{\mathcal{P}} = [\mathrm{Re}\,[\tilde{V}_{1,\mathcal{P}}], \mathrm{Im}\,[\tilde{V}_{1,\mathcal{P}}]]$. On the Poincaré section, the solutions (214) define ellipses which expand and rotate by a factors of $|\Lambda_1|$ and $\arg\Lambda_1$ respectively at each return. In order to resolve the unstable manifold, we start trajectories on an elliptic band parameterized by (δ, ϕ), such that the starting point in the band comes to the end of it on the first return, hence totality of these points cover the unstable manifold in the linear approximation. Such set of perturbations are given by

$$\delta\tilde{a}_{\mathcal{P}}(\delta, \phi) = \epsilon |\Lambda_1|^{\delta} W_{\mathcal{P}} R(\phi) c^{(1)}\,, \quad \text{where } \delta \in [0, 1)\,,\ \phi \in [0, 2\pi)\,, \tag{215}$$

and ϵ is a small number. We set $\epsilon = 10^{-3}$ and discretize (215) by taking 12 equidistant points in $[0, 1)$ for δ and 36 equidistant points in $[0, 2\pi)$ for ϕ and integrate each $\tilde{a}_{p_0} + \delta\tilde{a}_{\mathcal{P}}(\delta, \phi)$ forward in time. Figure 19 (a) shows the unstable manifold of p_0 resolved by this procedure at system size $L = 21.30$, for which the torus surrounding p_0 appears to be unstable. In Figure 19 (b) we show initial points that go into the calculation, and their first three returns in order to illustrate the principle of the method.

As we continue increasing the system size, we find that at $L \approx 21.36$, the invariant torus is completely destroyed and two new periodic orbits p_1 and p_2 emerge in the neighborhood of p_0. Both of these orbits appear as period 3 cycles in the Poincaré map. While p_1 is unstable, p_2 is stable with a finite basin of attraction. The unstable manifold of p_0 connects heteroclinically to the stable manifolds of p_1 and p_2. As we show in Figure 20 (a), resolving the unstable manifold of p_0 enables us to locate these heteroclinic connections between the pre-periodic orbits. Note that one-dimensional stable manifold of p_1 separates the unstable manifold of p_0 in two pieces. Green and blue orbits in Figure 20 (a) appear to be at two

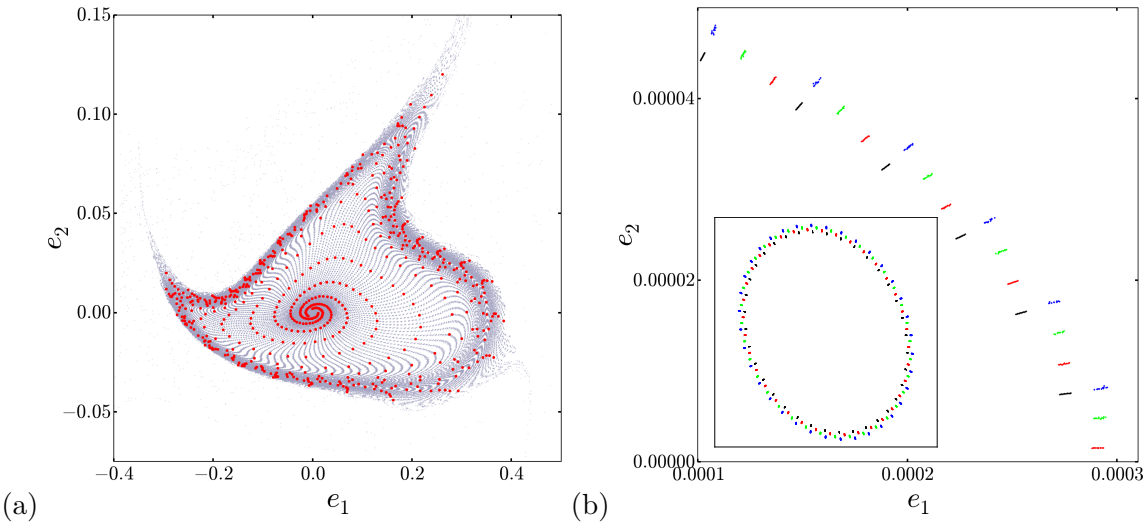

Figure 19: (a) Unstable manifold (gray) of p_0 on the Poincaré section (205) and an individual trajectory (red) within, system size $L = 21.30$. (b) Initial points (black) on the Poincaré section for unstable manifold computation and their first (red), second (green), and third (blue) returns. Inset: zoomed out view of the initial points and their first three returns.

sides of this invariant boundary, while one of them converges to p_2, the other leaves the neighborhood following the unstable manifold of p_1.

As the system size is increased, p_2 becomes unstable at $L \approx 21.38$. At $L \approx 21.477$ the two complex unstable Floquet multipliers collide on the real axis and at $L \approx 21.479$ one of them crosses the unit circle. After this bifurcation, we were no longer able to continue this orbit. At $L = 21.48$, the spreading of the p_0's unstable manifold becomes more dramatic, and its boundary is set by the one-dimensional unstable manifold of p_1, as shown in Figure 20 (b). We compute the unstable manifold of p_1 similar to (215) by integrating

$$\tilde{a}(\delta) = \tilde{a}_{p_1} \pm \epsilon \Lambda_1^{\delta} \tilde{V}_{1,\mathcal{P}} \,, \quad \text{where } \delta \in [0, 1) \,. \tag{216}$$

Λ_1 and $\tilde{V}_1$ in (216) are the unstable Floquet multiplier and the corresponding Floquet vector of $\tilde{a}_{p_1}$, and the initial conditions (216) similarly cover the unstable manifold of $\tilde{a}_{p_1}$ in the linear approximation.

5.6 Conclusions

In this chapter, we presented the first application of first Fourier mode slice on a **[pde??]**, Kuramoto-Sivashinsky equation in one space dimension under periodic boundary condition. We showed in Sect. 5.2 that the generic dynamics of this system can indeed come close to the border (97) of the first Fourier mode slice, and rescaling time as in (103) regularizes apparent discontinuities of the dynamics. In Sect. 5.2.1, we showed that continuous symmetry reduction allows us to visualize unstable manifolds of relative equilibria by canceling symmetry drifts of these solutions. In addition to the continuous translation symmetry, Kuramoto-Sivashinsky system was also equivariant under reflections and we reduced this symmetry by constructing polynomial invariants in Sect. 5.3. In Sect. 5.4, we described our attempts of studying invariant solutions found in ref. [22] in our symmetry-reduced representation, which suggested that periodic orbits (relative periodic orbits and pre-periodic

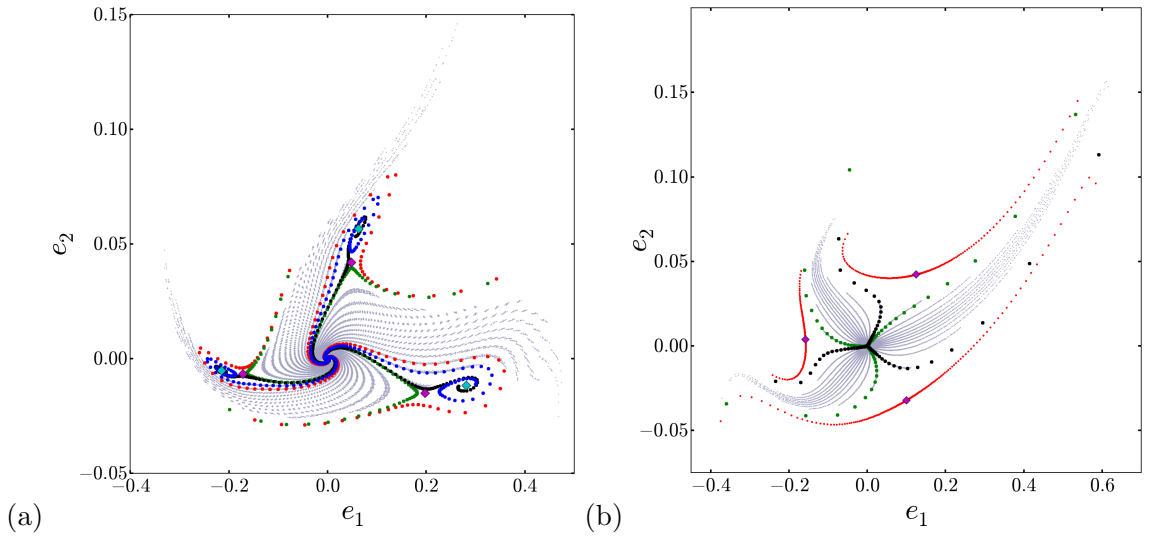

Figure 20: (a) Unstable manifold (gray) of p_0 on the Poincaré section (205) at $L = 21.36$. Colored dots correspond to different individual trajectories within the unstable manifold with qualitatively different properties. Diamond shaped markers correspond to the period-3 orbits p_1 (magenta) and p_2 (cyan). (b) Unstable manifold of p_0 (gray) and two orbits (black and green) within at $L = 21.48$. Red points lie on the one-dimensional unstable manifold of p_1.

orbits) are embedded in the strange attractor. In order to find which periodic orbits play important roles in shaping the chaotic attractor, we decided to reduce the system size to $L = 21.0$ and found a stable periodic orbit p_0 at this size. As we increase the system size, we found that this p_0 undergoes a torus bifurcation which gives birth to a stable torus in the periodic orbit's neighborhood, and the chaotic dynamics follow the breakdown of this torus as the system size is further increased. We visualized the unstable manifold of this periodic orbit, through this bifurcation sequence, which yielded the first dynamical relation between periodic orbits of the system: heteroclinic connections between p_0 and period-3 orbits p_1 and p_2 that emerge in its neighborhood.

We presented two new methods in this chapter: 1) a new method for reducing the O(2)-symmetry of PDEs, and 2) a symmetry-reduced state space Poincaré section visualization of 1- and 2-dimensional unstable manifolds of Kuramoto-Sivashinsky periodic orbits.

Our method for the computation of unstable manifolds is general and can find applications in many other **[ode??]** and **[pde??]** settings. The main idea here is a generalization of Gibson *et al.* [45] method for visualizations of the unstable manifolds of equilibria, originally applied to plane Couette flow, a setting much more complex then ours here. Our projections are 2-dimensional, but as all computations are carried out for the full Kuramoto-Sivashinsky equation (190), in 30 dimensions, it is remarkable how much information is captured by 2- and 3-dimensional projections of the O(2) symmetry-reduced Poincaré section - none of that structure is visible in the full state space.

Invariant polynomials similar to (201) can be constructed for any problem where the symmetry operation is the sign flip of a set of coordinates. Generalizations of this approach to richer discrete symmetries, such as dihedral groups, remains an open problem, with potential application to systems such as the Kolmogorov flow [85].

An interesting feature of the bifurcation scenario studied here is the apparent destabilization of the invariant torus before its breakdown. Note that in Figure 19 (a) the trajectories within the unstable manifold of p_0, diverge in normal direction from the region that was inhabited by a stable 2-torus for lower values of L. This suggest that the invariant torus has become normally hyperbolic [39]. This torus could be computed by the method of ref. [73], but that would be a new, technically demanding computation, beyond the scope of this thesis. Note also that the stable period-3 orbit p_2 in Figure 20 has a finite basin of attraction, and the trajectories which do not fall into it leave its neighborhood. In typical scenarios involving generation of stable - unstable pairs of periodic orbits within an invariant torus (see e.g. ref. [4]), the torus becomes a heteroclinic connection between the periodic orbit pair. Here the birth of the period-3 orbits appears to destroy the torus.

CHAPTER VI

PIPE FLOW

We now turn to the last, and the most challenging problem investigated in this thesis, the turbulent fluid flow in a circular pipe. This is a vastly complicated phenomenon that has been of experimental and theoretical interest for more than a century. From the standpoint of this thesis, pipe flow is a dynamical system that exhibits chaotic dynamics. However, it is worth noting that there many other reasons to study pipe flow, not least of which are real life applications in engineering settings.

Our strategy for studying pipe-flow is going to be similar to the preceding chapters: We are going to identify exact coherent structures and try to reveal their dynamical roles. However, in contrast to the two-modes and Kuramoto-Sivashinsky systems, it is believed that turbulent pipe flow does not have a strange attractor, but that it is organized around a strange repeller (or a chaotic saddle). Moreover, the conditions that cause the fluid flow to become turbulent are highly non-trivial and understanding them is crucially important for the study of pipe flow turbulence. Therefore, before diving into the mathematical description, we are going to review some well known facts of the turbulence transition in pipes.

6.0.1 Subcritical transition to turbulence

Parabolic velocity profile of the laminar flow in a circular pipe was identified experimentally by Hagen in 1839 [53] and Poiseuille in 1840 [87]. In his seminal 1894 experimental study [94], Osbourne Reynolds investigated the conditions at which the laminar flow in the pipe become "sinuous". He showed that the appearance of "eddies" is controlled by a single dimensionless parameter, which we now call the *Reynolds number*, $\mathrm{Re} = UD/\nu$, where U is the mean velocity, D is the pipe diameter, and ν is the kinematic viscosity. While Reynolds reported the critical value of the Re, above which the flow is inevitably turbulent, as 12000, he also mentioned that the eddies may appear way below this value ($\sim$2000) given that the incoming water has a sufficiently large disturbance. In modern experiments [84], laminar flow was maintained at Re as high as 10^5. These observations contradict a typical "linear instability of the laminar state" type of explanation for the transition to turbulence. As of this writing, there is no analytical proof of the linear stability of Hagen-Poiseuille flow for all Re. However, Meseguer and Trefethen [79] conclude on the basis of numerical computation of the eigenvalues of the linearized Navier-Stokes operator that the laminar state of the pipe flow is linearly stable for Re up to 10^7, i.e., for all practical cases that can be observed in laboratory experiments.

Linear stability of the laminar solution implies that the laminar-turbulent transition has to be triggered by a finite-amplitude perturbation [57, 77, 101]. In addition, both laboratory and numerical experiments suggest that the pipe flow turbulence is a transient phenomenon [59], namely, that regardless of the mean flow speed, turbulent fluid eventually relaminarize. These two results together suggest that turbulent and laminar regions of the state space are dynamically connected. This brings us to the first partitioning of the state space: (1) turbulent saddle, (2) basin of laminarization, and (3) something in between,

which goes by the name "edge of chaos".

6.0.2 Edge of chaos

Physical observables, such as dissipation rate, laminarization time, or pressure drop are completely different between laminar and turbulent flows. In order to identify the "edge of chaos" that separates laminar and turbulent regions of the state space, Skufca *et al.* [104] suggested tracking dependence of decay lifetimes on the amplitudes of perturbations to the laminar state as illustrated in the sketch of Figure 21. They proposed a numerical scheme for locating the edge states by bisecting between fast and slow laminarizing solutions with respect to perturbation amplitudes and demonstrated these ideas on a reduced order model. Skufca *et al.* computations also showed that the edge of chaos had a "folded" structure, that is one can find edges not only one threshold amplitude but also at larger amplitudes as sketched in Figure 21. Their methods were applied to the pipe flow by Schneider *et al.* [100], who observed that the edge of chaos is a chaotic set, unstable directions of which connect either to the laminar state, or to the turbulence. Duguet *et al.* [33] showed that relative equilibria (traveling waves) are embedded within the edge by combining Newton-Krylov searches with edge tracking methods. Moreover, they also showed that if the flow is restricted to azimuthally doubly symmetric subspace of solutions, then the edge of chaos can be a traveling wave, rather than a chaotic set.

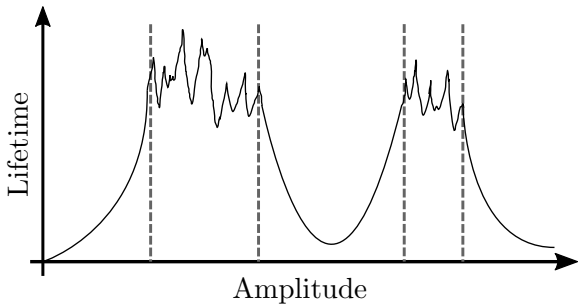

Figure 21: A sketch of dependence of decay lifetimes on the amplitude of perturbations. Dashed lines indicate the intervals where the perturbations appear to land on the edge of chaos.

6.0.3 Bifurcation scenario

Several earlier studies [34, 89, 90] of travelling waves in pipe flow found that some of these solutions come in pairs associated with a saddle-node bifurcation. The ones which have higher dissipation rates and physical properties similar to those of the turbulence are referred to as "upper branch" (UB) solutions, and their counterparts are referred to as "lower branch" (LB). Duguet *et al.* [33] travelling waves embedded in the edge of chaos belonged to the lower branch family. These developments had motivated detailed bifurcation studies of these solutions in both pipe [75, 76] and plane Couette flows [69]. Common findings of these studies can be summarized by the qualitative bifurcation diagram of Figure 22: Lower and upper branch solutions are born out of a saddle node bifurcation. While the UB is stable for an initial interval of Re values, it goes unstable through a set of period-doubling bifurcations [69], which give birth to a small attracting set. After further bifurcations, this set reaches the lower branch solution (boundary crisis), which connects it to the laminar

state; hence the chaotic set becomes transient. Thereafter, the only attracting object in the state space is presumed to be the laminar solution and the turbulence is a "chaotic saddle".

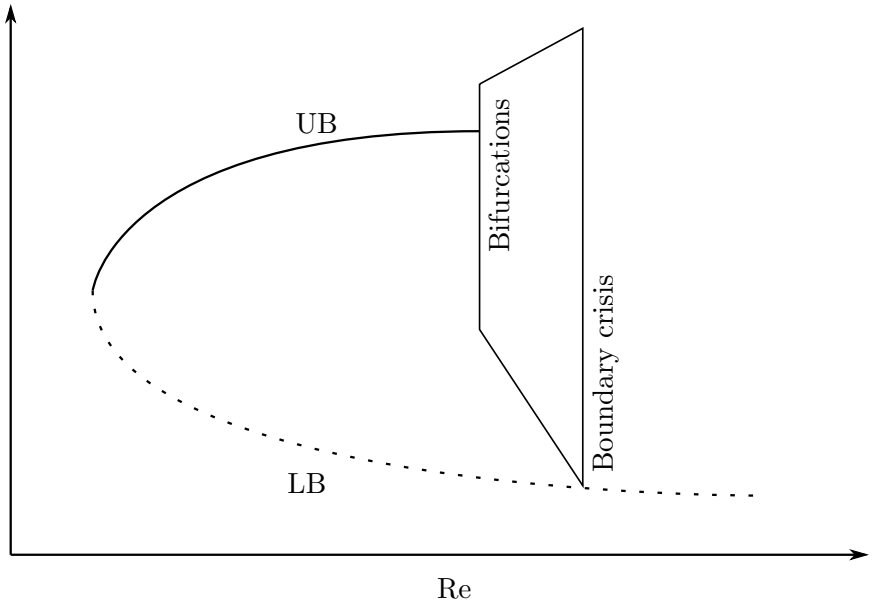

Figure 22: A sketch of the subcritical transition to turbulence through a saddle-node bifurcation with increasing Reynolds number.

Refs. [75, 76] studied pipe flow in small computational domains. Recently, Avila *et al.* [8] showed that when double periodicity in azimuthal direction and reflection invariance were imposed, localized solutions of a longer pipe also follow a similar bifurcation scenario, however, with roles of upper and lower branch solutions taken over by relative periodic orbits.

We should emphasize that bifurcation sequences of the sketch of Figure 22, with the edge states given by exact coherent structures, were obtained only when the pipe flow was restricted to symmetry invariant subspaces. We already know from refs. [33, 100] that if such a condition is not imposed, than the edge of chaos itself is chaotic. Thus, the actual transition scenario may have many more features not sketched in Figure 22. Nevertheless, this bifurcation scenario sketch gives an useful mental picture by providing us the first, and coarsest, partitioning of the state space. In the rest of this chapter, we are going to demonstrate that the relative periodic orbits embedded in the turbulent set represent its internal structure.

6.1 Problem formulation

We start by writing incompressible Navier-Stokes equation (1) without external forcing

$$\mathbf{u}_\tau + \mathbf{u}\cdot\nabla\mathbf{u} = -\frac{\nabla p}{\rho} + \nu\nabla^2\mathbf{u}\,, \qquad \nabla\cdot\mathbf{u} = 0\,. \tag{217}$$

Velocity field $\mathbf{u}$ vanishes at the pipe wall, and is periodic in azimuthal and axial directions:

$$\mathbf{u}(r=R,\theta,z) = 0\,, \tag{218}$$
$$\mathbf{u}(r,\theta+2\pi,z) = \mathbf{u}(r,\theta,z)\,, \tag{219}$$
$$\mathbf{u}(r,\theta,z+L) = \mathbf{u}(r,\theta,z)\,. \tag{220}$$

Let us denote radial, azimuthal, and axial components of velocity field $\mathbf{u}$ by u, v, and w respectively. Hagen-Poiseuille flow $\mathbf{u}_{HP}$ corresponds to a steady ($\partial\mathbf{u}_{HP}/\partial\tau = 0$) flow profile, drifting only in the axial direction ($u_{HP} = v_{HP} = 0$), and depending only on the radial coordinate ($\partial\mathbf{u}_{HP}/\partial z = \partial\mathbf{u}_{HP}/\partial\theta = 0$). Rewriting (217) with these assumptions

$$0 = -\frac{\nabla p}{\rho} + \nu\nabla^2\mathbf{u}_{HP}\,, \tag{221}$$

tells us that the pressure gradient ∇p may not have azimuthal and radial components. Writing partial derivatives explicitly we have

$$\nu\frac{1}{r}\frac{\partial}{\partial r}\left(r\frac{\partial w_{HP}}{\partial r}\right) = \frac{1}{\rho}\frac{\partial p}{\partial z}\,, \tag{222}$$

which we can integrate as

$$w_{HP}(r) = \frac{1}{4\rho\nu}\frac{\partial p}{\partial z}r^2 + c_1\ln r + c_2\,. \tag{223}$$

For the solutions to be finite at the pipe center, c_1 has to be 0. We find c_2 from the no-slip boundary condition (218) as $c_2 = -(4\rho\nu)^{-1}(\partial p/\partial z)R^2$, hence the axial velocity is given by

$$w_{HP}(r) = -\frac{1}{4\rho\nu}\frac{\partial p}{\partial z}\left(R^2 - r^2\right)\,, \tag{224}$$

which depends on the radial coordinate parabolically. As we can see from (224), in order to sustain the Hagen-Poiseuille flow we need a pressure gradient, which we will assume to be constant $-\Pi = \partial p/\partial z$. We can now compute the mean axial speed of the Hagen-Poiseuille flow

$$U = \frac{1}{\pi R^2}\int_0^R w_{HP}(r)2\pi r dr = \frac{\Pi R^2}{8\rho\nu}\,. \tag{225}$$

In summary, the base flow (Hagen-Poiseuille) solution of pipe flow is given by

$$\mathbf{u}_{HP}(r,\theta,z) = 2U\left(R^2 - r^2\right)\hat{\mathbf{z}}\,, \tag{226}$$

where U is the mean axial speed (225). We can now nondimensionalize quantities in (217) by picking a length scale as the diameter $D = 2R$ of the pipe and a time scale as D/U. Denoting dimensionless quantities with primes, we have

$$\mathbf{u}' = \mathbf{u}/U,\ \tau' = \tau(U/D),\ p' = (p/\rho)U^{-2}\,. \tag{227}$$

After substituting these definitions into (217) we obtain

$$\frac{U^2}{D}\mathbf{u}'_{\tau'} + \frac{U^2}{D}\mathbf{u}'\cdot\nabla'\mathbf{u}' = -\frac{U^2}{D}\nabla' p' + \nu\frac{U}{D^2}\nabla'^2\mathbf{u}'\,. \tag{228}$$

If we now multiply above equation by D/U^2, define the Reynolds number $\mathrm{Re} = DU/\nu$, and drop primes, we obtain

$$\mathbf{u}_\tau + \mathbf{u}\cdot\nabla\mathbf{u} = -\nabla p + \frac{1}{\mathrm{Re}}\nabla^2\mathbf{u}\,. \tag{229}$$

This result confirms Osbourne Reynolds' observation that the transition to turbulence in the pipe flow depends on the value of a single parameter, i.e., the Reynolds number. In the dimensionless variables, Hagen-Poisouille (226) flow becomes

$$\mathbf{u}_{HP}(r,\theta,z) = 2(1-(2r)^2)\hat{\mathbf{z}}\,. \tag{230}$$

Let us now express the velocity and pressure fields as sum of "base flow fields" and deviations

$$\mathbf{u} = \mathbf{u}_{HP} + \mathbf{u}'\,, \quad \nabla p = -\Pi\hat{\mathbf{z}} + \nabla p'\,, \tag{231}$$

and plug these into Navier-Stokes equation (229) to obtain

$$\mathbf{u}'_\tau + \mathbf{u}_{HP}\cdot\nabla\mathbf{u}' + \mathbf{u}'\cdot\nabla\mathbf{u}_{HP} + \mathbf{u}'\cdot\nabla\mathbf{u}' = -\nabla p' + \frac{1}{\mathrm{Re}}\nabla^2\mathbf{u}'\,. \tag{232}$$

When the flow becomes turbulent, it experiences pressure drops and mean mass flux decreases from its value for the laminar state. However, in experiments (see e.g. refs. [57, 81]), one typically controls the mean mass flux. In order to account for that, we add an additional axial pressure gradient and drop the primes again to obtain our final form of the Navier-Stokes equation for fluctuations from the base flow

$$\mathbf{u}_\tau + \mathbf{u}_{HP}\cdot\nabla\mathbf{u} + \mathbf{u}\cdot\nabla\mathbf{u}_{HP} + \mathbf{u}\cdot\nabla\mathbf{u} = -\nabla p + 32\frac{\beta}{\mathrm{Re}}\hat{\mathbf{z}} + \frac{1}{\mathrm{Re}}\nabla^2\mathbf{u}\,, \tag{233}$$

where $\beta = \beta(\tau)$ is a time dependent parameter to be adjusted to ensure the mean mass flux is equal to that of the Hagen-Poiseuille flow (230).

In (233) and hereafter, velocity field $\mathbf{u} = [u,v,w](r,\theta,z)$ and the pressure $p = p(r,\theta,z)$ correspond to their deviations from their base flow values (230). We use a primitive variable version of the `Openpipeflow.org` [114] for numerical integration of $\mathbf{u}(r,\theta,z)$. Details of this implementation is outside the scope of this thesis, however, before moving onto presenting our results, we need to explain the representation of data in this implementation, and norms to be used in the numerical results of the following sections.

6.1.1 Discretization and the state space

For the Kuramoto-Sivashinsky system in one space dimension under periodic boundary condition, Chapter 5.1, discretization of the flow field as a Fourier series was the obvious choice. However, we now have a three dimensional vector field defined over a three dimensional space and time. `Openpipeflow` discretizes flow fields in Fourier series in periodic directions (axial and azimuthal) and uses finite difference methods for the radial direction,

$$\mathbf{u}(r_n,\theta,z) = \sum_{|k|<K}\sum_{|m|<M}\mathbf{u}_{nkm}e^{i(\alpha kz+m_0m\theta)}\,, \tag{234}$$

where $\alpha = 2\pi/L$ is the axial wave number, $m_0 = 1,2,3,\ldots$ imposes a higher azimuthal periodicity condition if its value is other than 1, and indices n, k and m respectively denote elements in radial, axial, and azimuthal discretizations. Decomposition (234) corresponds to the values of flow fields u,v,w at a particular radial position r_n ($n = 0,\,1,\,\ldots,N$). To

develop a sense for the dimension of the state space, let us make a rough estimate. If we were to pick $N = 2M + 1 = 2K + 1 = 10$, we would need to store 3×10^3 data points to represent each state. This is a large number and this fact by itself makes this problem orders of magnitude harder than the examples we studied in previous chapters.

While (234) is in fact how the data is represented in our integrator, we can still think of the state of a fluid $\mathbf{u}(\mathbf{x}, \tau)$ at the time instant τ as a vector $a(\tau)$ in the state space. For the most parts of the following sections, we are going to use state space notation for presenting our results, however, the reader should keep in mind that a state space vector corresponds to the N velocity fields (234). Most of our results are going to be in terms of inner products in this state space, which we describe next.

6.1.2 Inner products and norms

As we have visualized for several examples in the previous two chapters, strange sets have complex geometries and "closeness" of two points in a given projection of the state space can be very misleading. Take, for example, the return map Figure 10 of the two-modes system and consider two points on left and right hand sides of its cusp. These points are very close to each other in the Euclidean distance that was used to parametrize the arclengths in the Poincaré section, yet, their forward time dynamics are completely different. However, given the difficulty of the current problem, our choices are limited and inevitably, norms will appear in our calculations and visualizations. In this section we introduce the norms that we will use here and explain the motivations for our particular choices. In the following sections, we will try to avoid the dangers associated with using a given norm by presenting our results in different norms and visualizations.

Let a_1 and a_2 denote state vectors that correspond to velocity fields $\mathbf{u}_1$ and $\mathbf{u}_2$ respectively, we define the $L2$ distance between these vectors by the inner product

$$\langle a_1,\, a_2 \rangle_{L2} = \frac{1}{2E_{HP}} \int_V \mathbf{u}_1 \cdot \mathbf{u}_2 \, dV \,, \tag{235}$$

$$= \frac{1}{E_{HP}} \int_0^{1/2} r dr \sum_{k,m} \mathbf{u}^*{}_{1,km}(r) \cdot \mathbf{u}_{2,km}(r) \,, \tag{236}$$

where V is the volume of the pipe and E_{HP} is the kinetic energy of the Hagen-Poiseuille flow. In (236), we wrote the integral explicitly in terms of Fourier modes and radial integration, which in practice is approximated numerically. The factor $1/2$ in (235) is included so that the norm square of a state in $L2$ metric yields its kinetic energy

$$E(a) = \|a\|_{L2}^2 = \langle a, a \rangle \,. \tag{237}$$

Hence in literature, the $L2$ norm is frequently referred to as the "energy" norm.

As we will illustrate in our numerical results, we found that it is sometimes informative to use a metric that emphasizes larger scale structures in continuous symmetry directions. For this reason, we define the "low pass" metric, where we penalize the higher Fourier modes (short wavelengths) as follows

$$\langle a_1,\, a_2 \rangle_{LP} = \frac{1}{V} \int_0^{1/2} r dr \sum_{k,m} \frac{1}{1 + (\alpha k)^2 + (m_0 m)^2} \, \mathbf{u}^*{}_{1,km}(r) \cdot \mathbf{u}_{2,km}(r) \,. \tag{238}$$

In the axial and azimuthal directions this is a variant of a Sobolev H^{-1} norm [1, 15, 107]: the weights are smaller for larger values of k and m, hence shorter wavelengths are de-emphasized.

6.2 *Symmetries of the pipe flow*

In infinite space, Navier-Stokes equation (1) are equivariant under translations, rotations, and reflections [42]. Pipe walls disallow translations in radial direction and permit rotations only in azimuthal direction. Moreover, the net pressure gradient in the axial direction breaks $z \to -z$ reflection symmetry, and thus the remaining symmetries are translations in axial direction and rotations and reflections about the pipe axis. We are going to denote continuous symmetries by $g(\phi, \ell)$ and reflection by σ; their actions on flow fields are

$$\begin{aligned} g(\phi,\ell)\,[u,v,w,p](r,\theta,z) &= [u,v,w,p](r,\theta-\phi,z-\ell)\,, \\ \sigma\,[u,v,w,p](r,\theta,z) &= [u,-v,w,p](r,-\theta,z)\,. \end{aligned} \tag{239}$$

The symmetry group of stream-wise periodic pipe flow is thus $\mathrm{SO}(2)_z \times \mathrm{O}(2)_\theta$: a generic state of fluid (no symmetry) has infinitely many copies with respect to both translations and rotations. In this thesis, we are not going to tackle this problem in full, but will for pedagogical reasons focus on dynamics restricted to a flow-invariant subspace of $\mathrm{SO}(2)_z$ solutions with no drift in the azimuthal direction.

6.2.1 Shift-and-reflect invariant subspace

There are many ways one can construct a flow-invariant subspace using symmetries of the pipe flow. Our choice is the so-called "shift-and-reflect subspace" of flow fields invariant under a half domain axial translation and the reflection

$$a = \sigma g(0, L/2) a\,, \tag{240}$$

$$[u,v,w,p](r,\theta,z) = [u,-v,w,p](r,-\theta,z-L/2)\,. \tag{241}$$

While restriction of dynamics is to this subspace is not physical in the sense that it cannot be realized experimentally, all solutions that satisfy (240) are also solutions of the full Navier-Stokes equation, and laboratory experiments [58] observe flow fields rather similar to the traveling wave solutions found in this subspace [34].

We are now going to show that the solutions satisfying (240) define a flow-invariant subspace of Navier-Stokes equation (217). Let us denote the shift-and-reflect operation by $\bar\sigma = \sigma g(0, L/2)$. Since azimuthal reflections and axial shifts commute, $\bar\sigma$ is its own inverse $1 = \bar\sigma^2$. Therefore we can define projection operators

$$P^\pm = \frac{1}{2}(1 \pm \bar\sigma)\,, \tag{242}$$

with which we can decompose velocity fields $\mathbf{u}$ into symmetric and antisymmetric parts as

$$\mathbf{u}^\pm = P^\pm \mathbf{u}\,. \tag{243}$$

Note that each velocity field can be expressed as sum of its symmetric and antisymmetric parts

$$\mathbf{u} = \mathbf{u}^+ + \mathbf{u}^- \tag{244}$$

and the action of $\bar\sigma$ on symmetric and antisymmetric fields is

$$\bar\sigma \mathbf{u}^\pm = \pm \mathbf{u}^\pm\,. \tag{245}$$

We can decompose the pressure field similarly and express each term in Navier-Stokes equation (217) in terms of sum of their symmetric and anti-symmetric parts. With this

separation, each term will separate into the sum of two components, except the nonlinear term $\mathbf{u}\cdot\nabla\mathbf{u}$

$$\begin{aligned}\mathbf{u}\cdot\nabla\mathbf{u} &= (\mathbf{u}^+ + \mathbf{u}^-)\cdot\nabla(\mathbf{u}^+ + \mathbf{u}^-) \\ &= \mathbf{u}^+\cdot\nabla\mathbf{u}^+ + \mathbf{u}^+\cdot\nabla\mathbf{u}^- + \mathbf{u}^-\cdot\nabla\mathbf{u}^+ + \mathbf{u}^-\cdot\nabla\mathbf{u}^- \,. \end{aligned} \tag{246}$$

Action of $P^\pm$ on the nonlinear term (246) yields

$$\begin{aligned}P^\pm(\mathbf{u}\cdot\nabla\mathbf{u}) &= \frac{1}{2}\big[\mathbf{u}^+\cdot\nabla\mathbf{u}^+ + \mathbf{u}^+\cdot\nabla\mathbf{u}^- + \mathbf{u}^-\cdot\nabla\mathbf{u}^+ + \mathbf{u}^-\cdot\nabla\mathbf{u}^- \\ &\quad \pm\mathbf{u}^+\cdot\nabla\mathbf{u}^+ \mp \mathbf{u}^+\cdot\nabla\mathbf{u}^- \mp \mathbf{u}^-\cdot\nabla\mathbf{u}^+ \pm \mathbf{u}^-\cdot\nabla\mathbf{u}^-\big] \,. \end{aligned} \tag{247}$$

If we now act Navier-Stokes equation (217) from the left with $P^\pm$, we obtain the following decomposition

$$\mathbf{u}^+_\tau = -(\mathbf{u}^+\cdot\nabla\mathbf{u}^+ + \mathbf{u}^-\cdot\nabla\mathbf{u}^-) - \nabla p^+ + \frac{1}{\mathrm{Re}}\nabla^2\mathbf{u}^+ \,. \tag{248}$$

$$\mathbf{u}^-_\tau = -(\mathbf{u}^+\cdot\nabla\mathbf{u}^- + \mathbf{u}^-\cdot\nabla\mathbf{u}^+) - \nabla p^- + \frac{1}{\mathrm{Re}}\nabla^2\mathbf{u}^- \,. \tag{249}$$

If we set $\mathbf{u}^- = \nabla p^- = 0$, then all terms on RHS of (249) vanish, and an initial condition in the shift-and-reflect symmetric subspace $\mathbf{u}^+$ stays within it; the subspace is flow-invariant. Setting $\mathbf{u}^+ = \nabla p^+ = 0$, however, does not keep $\mathbf{u}$ within the shift-and-reflect antisymmetric subspace $\mathbf{u}^-$.

We next show that the shift-and-reflect invariance (240) fixes the azimuthal rotation symmetry to discrete rotations by π. Consider the rotated solution

$$a' = g(\phi,0)a \,, \tag{250}$$

$$[u,v,w,p]'(r,\theta,z) = [u,v,w,p](r,\theta-\phi,z) \tag{251}$$

where a satisfies (240) and is thus in shift-and-reflect subspace. If we require (251) to satisfy (241), we get

$$\begin{aligned}[u,-v,w,p]'(r,-\theta,z-L/2) &= [u,v,w,p]'(r,\theta,z) \,, \\ [u,-v,w,p](r,-\theta-\phi,z-L/2) &= [u,v,w,p](r,\theta-\phi,z) \,. \end{aligned} \tag{252}$$

Now the question of which azimuthal shifts are allowed becomes which values ϕ can take, such that (252) is satisfied given (241). We can simplify the notation as follows. Given (i) $f(\theta) = f(-\theta)$, (ii) $f(\theta + n2\pi) = f(\theta)\,, n\in\mathbb{Z}$, and (iii) $\theta\in\mathbb{R}$, what values can ϕ take for $f(\theta-\phi) = f(-\theta-\phi)$ to be true? Since θ is arbitrary we can shift it as $\theta\to\theta+\phi$, then the condition becomes $f(\theta) = f(-\theta-2\phi)$, and from (i) and (ii) we find

$$\phi = n\pi \,. \tag{253}$$

In other words, shift-and-reflect invariance (240) allows for azimuthal rotations only by π. We illustrate this property in Figure 23.

To summarize, the symmetry group G of the pipe flow in the shift-and-reflect subspace is

$$G = \{g_\theta, g_z(l)\} \,, \tag{254}$$

where $g_\theta = g(\pi,0)$ and $g_z(l) = g(0,l)$.

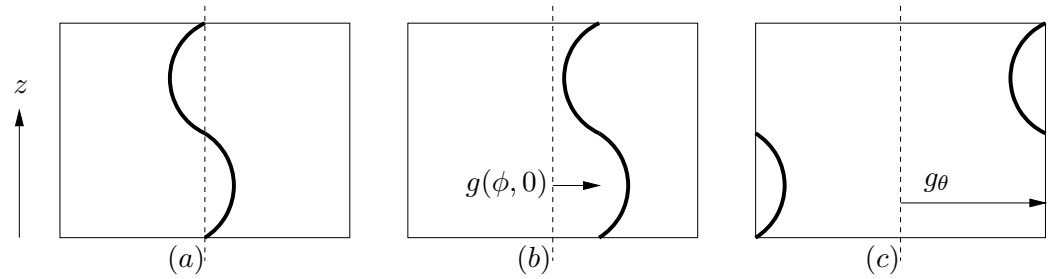

Figure 23: (a) Sketch of a shift-and-reflect symmetric state on $(\theta, z) \in [-\pi, \pi] \times [0, L]$. (b) If the state in (a) is rotated by an angle ϕ other than π, the shift-and-reflect symmetry is broken. (c) State in (a) rotated by π, hence shift-and-reflect symmetric.

Before moving on, we should state what shift-and-reflect invariance implies for our data representation (234). Action of shift-and-reflect operation (241) on flow fields u, w, p are same, while v picks up an extra minus. Consider the shift-and-reflect invariant flow field, $u(r_n, \theta, z) = u(r_n, -\theta, z - L/2)$, in the computational basis:

$$\begin{aligned}
\sum_{|k|<K} \sum_{|m|<M} u_{nkm} e^{i\left(\frac{2\pi}{L} kz + m_0 m\theta\right)} &= \sum_{|k|<K} \sum_{|m|<M} u_{nkm} e^{i\left(\frac{2\pi}{L} k(z-L/2) - m_0 m\theta\right)} , \\
\sum_{|k|<K} \sum_{|m|<M} u_{nkm} e^{i\left(\frac{2\pi}{L} kz + m_0 m\theta\right)} &= \sum_{|k|<K} \sum_{|m|<M} u_{nkm} e^{i\left(\frac{2\pi}{L} kz - \pi k - m_0 m\theta\right)} , \\
\sum_{|k|<K} \sum_{|m|<M} u_{nkm} e^{i\left(\frac{2\pi}{L} kz + m_0 m\theta\right)} &= \sum_{|k|<K} \sum_{|m|<M} (-1)^k u_{nkm} e^{i\left(\frac{2\pi}{L} kz - m_0 m\theta\right)} , \\
\sum_{|k|<K} \sum_{|m|<M} u_{nkm} e^{i\left(\frac{2\pi}{L} kz + m_0 m\theta\right)} &= \sum_{|k|<K} \sum_{|m|<M} (-1)^k u_{nk(-m)} e^{i\left(\frac{2\pi}{L} kz + m_0 m\theta\right)} ,
\end{aligned} \tag{255}$$

where in the last step we replaced m with $-m$ on the right hand side, which we are allowed to, as m is summed over. Since the Fourier modes are orthogonal, (255) implies that $[u, v, w, p]_{nkm}$ in shift-and-reflect invariant subspace has to satisfy

$$\begin{aligned}
[u, w, p]_{nkm} &= (-1)^k [u, w, p]_{nk(-m)} , \\
v_{nkm} &= (-1)^{k+1} v_{nk(-m)} ,
\end{aligned} \tag{256}$$

where we have an extra minus sign for v, as v picks up extra minus sign under the shift-and-reflect operation.

6.2.2 Exact coherent structures

Since all solutions of the pipe flow drift in the axial direction, the simplest exact coherent structures are relative equilibria (traveling waves)

$$a_{TW}(\tau) = g_z(c_{TW}\, \tau) a_{TW}(0) , \tag{257}$$

whose sole dynamics is drifting along the axial direction with constant phase speed c_{TW}.

Given the symmetry group (254), we are allowed to have two types of relative periodic orbits: those recur after one period with a stream-wise shift l_{RPO},

$$a_{RPO}(T_{RPO}) = g_z(-l_{RPO})\, a_{RPO}(0) , \tag{258}$$

and those recur after one period with a stream-wise shift by l_{RPO} and azimuthal rotation by π

$$a_{RPO}(T_{RPO}) = g_\theta\, g_z(-l_{RPO})\, a_{RPO}(0)\,. \tag{259}$$

6.3 Turbulent pipe flow

We are now ready to present results of our turbulent pipe flow collaboration [117]. Ashley Willis is the author of the `Openpipeflow.org` code used in all our numerical Navier-Stokes calculations [114]. Kimberly Short had determined most of the exact coherent structures listed in Table 4; several were contributed by Ashley Willis and Mohammad Farazmand. As a result, some of the implementation details are skipped in this chapter and appropriate references are provided. Emphasis is on the results contributed by the author of this thesis, presented in Sect. 6.3.1 and Sects. 6.3.4 to 6.3.6.

We have explained in Sect. 6.2.1 that the solutions we are going to present belong to the shift-and-reflect invariant subspace, with only one continuous symmetry in the system. In addition, we also set $m_0 = 4$ in (234), thus all states we are going to study will be azimuthally 4-fold symmetric. Other parameters that go into simulations are the wave number $\alpha = 1.7$ and $\mathrm{Re} = 2500$, which corresponds to a periodic pipe of length $L = \pi/\alpha = 1.85\,D$ with empirical turbulent lifetimes that can go up to $1000\,D/U$. In simulations, Fourier expansions (234) were truncated at $K = 17$ in stream-wise and $M = 11$ in azimuthal directions; and $N = 64$ points were used for radial discretization, which corresponds to a $3 \times (2 \times 17 + 1) \times (11 + 1) \times 64 = 80640$-dimensional state space. Here modes with $m < 0$ are excluded from the state space since $\mathbf{u}_{nkm} = \mathbf{u}^*_{n-k-m}$.

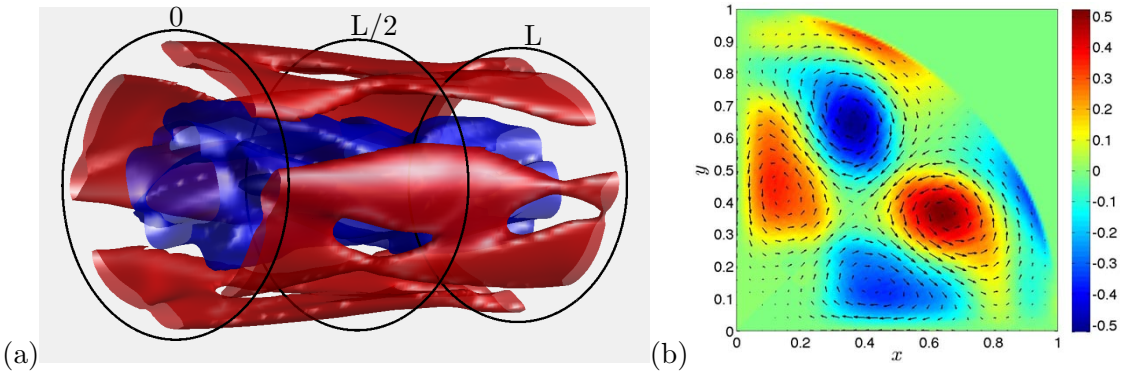

Figure 24: (a) A snapshot of a turbulent state in a pipe flow simulation. Red and blue respectively correspond to fast ($0.1U$) and slow ($-0.1U$) stream-wise velocity isosurfaces. (b) $\mathrm{TW}_{2.04}$, the grandmother relative equilibrium of the 'first family' (see Figure 28). The color shows the averaged streamwise vorticity $\bar{\omega}_z$. The arrows show $(\bar{u}_r, \bar{u}_\theta)$ where $\bar{u}_r$ and $\bar{u}_\theta$ are averaged radial and azimuthal velocities, respectively. Only a quarter of the tube is shown.

In this setting, a typical turbulent state looks like Figure 24 (a), where we visualized the slow ($-0.1U$) and fast ($0.1U$) stream-wise velocity isosurfaces of the flow (relative to the base flow). Note also that fast structures are closer to the pipe walls, while slower ones concentrated in the middle; this is a typical feature of the pipe flow turbulence. As we have imposed $m_0 = 4$ symmetry, the flow structures come in four identical copies in the pipe cross section. In addition, due to the imposed shift-and-reflect symmetry (254), the fundamental domain is restricted to $z \in [0, L/2]$ and is thus 1/8 of the computational

cell. For example, this tiling by 8 copies of a fundamental tile is manifest in the streamwise averages of any solution we consider, such as the relative equilibrium of Figure 24 (b).

The reader my wonder: surely 1/8th of a very stubby, periodic cylinder has nothing to do with generic turbulence in a pipe of infinite length? And the reader is right. It is just that with the existing methods we are not able to find sets of physically important exact coherent structures even in only a slightly longer pipe [115], with $L = 2.5$, with all the same imposed symmetries. Our purpose here is more modest, but apparently still computationally challenging: to show that we can triangulate the state space of *any* variant of pipe flow in terms of exact coherent structures and their invariant manifolds.

6.3.1 Continuous symmetry reduction

One can approach symmetry reduction from two radically different points of view: global, group-theoretical viewpoint, or local, dynamical 'moving frame' viewpoint. Neither is perfect. In the group-theoretical viewpoint, since the symmetry and dynamics commute, the reduction of the full state space stratification by group orbits to a symmetry-reduced state space, where each orbit is a point, is a purely group theoretic exercise, to be solved without any reference to the dynamics. An example is the invariant polynomials approach of the Hilbert-Weyl theorem 3.1, beautiful, but due to proliferation of invariant polynomials and the syzygies relating them, useless for the problem at hand. That was realized almost immediately by Cartan [16] who took a local, differential geometry point of view. Unlike the invariant polynomials approach, here the symmetry-reduced state space has one dimension less for every continuous parameter, and remains embedded in the original state space. For a fluid dynamicist, Cartan's notion of 'moving frames' is very intuitive: if the flow has a travelling wave solution, one immediately uses the continuous symmetry to change coordinates to the co-moving frame, and bring the study of the bifurcations (infinitesimal neighborhood of the solution) to the standard equilibrium setting. That goes by the name 'the Equivariant Branching Lemma' [47, 62]. The method of slices then takes the particular, physically important solution as a 'template' [9, 96] and then tries to extend its neighborhood to as large a set as possible of nearby solutions that qualitatively resemble the template. In general, one expects that a slice covering the dynamically interesting region of the state space ('inertial manifold') requires a set of overlapping charts [23] whose construction appears to be largely a dark art.

Our first Fourier mode slice (handcrafted to fit only SO(2) and its abelian extensions) is a happy combination of the two approaches: it is purely group-theoretical, based on the eigenfunctions of the symmetry (Fourier modes), but prefered dynamically, by establishing that the border of the corresponding slice is optimal, in the sense that a generic dynamical orbit does not cross it. It comes at its own price, by distorting the dynamics close to the slice border. In Sect. 3.3.5 we outlined the procedure for extending the first Fourier mode slice to higher-dimensional settings, which included three-dimensional vector fields that are equivariant under $\mathrm{SO}(2) \times \mathrm{SO}(2)$, i.e. the case of pipe and plane Couette flows.

The pipe flow project had started in 2009 and in its first phase [115] symmetry reduction was implemented by the method of slices, with as many as 12 templates needed to capture one relative periodic orbit. That has since been brought down to a single, judiciously chosen template [117]. The second phase [116] was a hybrid, based on implementing our first Fourier mode slice [14] in the axial direction, but using a 'generic' turbulent state template in the azimuthal direction. As a consequence, implementation of the first Fourier mode slice for the axial SO(2) symmetry of the pipe flow that we used in results to be presented in

upcoming sections is slightly different from our prescription in Sect. 3.3.5. Before describing this approach, we will show how extend the first Fourier mode slice method to the current problem, as defined in Sect. 3.3.5.

6.3.1.1 A first Fourier mode slice template from geometry

We begin by rewriting the slice templates (139) required for reducing $\mathrm{SO}(2)\times\mathrm{SO}(2)$ for the pipe geometry

$$\begin{aligned} \mathbf{u}'_z(\mathbf{x}) &= \mathbf{f}(r)\cos(2\pi z/L)\,, && (260)\\ \mathbf{u}'_\theta(\mathbf{x}) &= \mathbf{g}(r)\cos(2\pi\theta)\,. && (261) \end{aligned}$$

Our problem is now to find an $\mathbf{f}(r)$, such that the flow does not visit the slice border. In Sect. 6.2.1, we found the conditions (256) that flow fields in the shift-and-reflect invariant subspace must satisfy. We also know that $\mathbf{u}_{nkm} = \mathbf{u}^*_{n(-k)(-m)}$ since $\mathbf{u}$ is real valued. If we rewrite (256) using this property, we obtain

$$\begin{aligned} [u,w,p]_{nkm} &= (-1)^k [u,w,p]^*_{n(-k)m}\,,\\ v_{nkm} &= (-1)^{k+1} v^*_{n(-k)m}\,. \end{aligned} \qquad (262)$$

The template (260) corresponds to Fourier modes with $(k=1, m=0)$. If we write (262) explicitly for these modes, we obtain

$$\begin{aligned} [u,w,p]_{n10} &= -[u,w,p]^*_{n(-1)0}\,,\\ v_{n10} &= v^*_{n(-1)0}\,. \end{aligned} \qquad (263)$$

From the property of $\mathbf{u}$ being real valued, we also now that $(k=1, m=0)$ modes should satisfy

$$[u,v,w,p]_{n10} = [u,v,w,p]^*_{n(-1)0}\,. \qquad (264)$$

Hence, from (263) and (264), we conclude that $[u,w,p]_{n10}=0$. This leaves us with only one choice among the flow fields, namely v-component, for constructing a first Fourier mode slice template (260).

We still need to determine the r-dependence of our template. Motivated by the fact that the Bessel functions are eigenfunctions of Laplacian in polar coordinates, we decided to try the following slice template

$$\begin{aligned} v'(\mathbf{x}) &= J_0(2\alpha_1 r)\cos(2\pi z/L)\,, && (265)\\ \left[u',w',p'\right](\mathbf{x}) &= 0\,, \end{aligned}$$

where J_0 is the 0^{th} Bessel function of the first kind and $\alpha_1 = 2.4048$ is the first root of J_0, thus (265) satisfies the no-slip boundary condition (218) on the pipe wall $r=1/2$.

With the slice template $\hat{a}'$ corresponding to the flow fields (265), for each state a finding the slice-fixing shifts accounts to computing

$$\ell(\tau) = L\frac{\arg\left(\langle a(\tau),\,\hat{a}'\rangle_{L2} + i\langle a(\tau))\,,\,g_z(L/4)\hat{a}'\rangle_{L2}\right)}{2\pi}\,, \qquad (266)$$

and the axial translation symmetry reduced state $\hat{a}$ can be found by

$$\hat{a}(\tau) = g_z(-l)a(\tau)\,. \qquad (267)$$

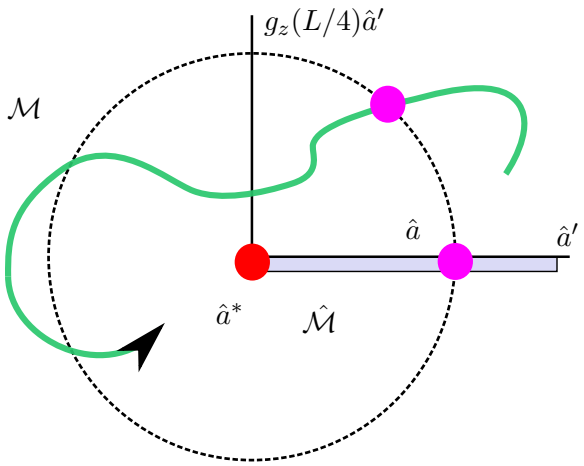

Figure 25: Group orbit (dashed line) of a state a projected on the hyperplane spanned by the slice template $\hat{a}'$ and its quarter-domain translation $g_z(L/4)\hat{a}'$. A similar group orbit exists for every point on the orbit (green) of a, unless it intersects the slice border $\hat{a}^*$ (red dot). In this 2-dimensional projection the entire symmetry-reduced state space projects onto the horizontal half-line, and the slice border projects onto the origin. Adapted from ref. [116].

as illustrated in Figure 25.

In order to test this approach, we ran two numerical experiments. We applied the symmetry reduction method to a relative periodic orbit $\mathrm{RPO}_{26.06}$ to verify that it becomes a periodic orbit within the slice. Figure 26(a) shows one period of the $\mathrm{RPO}_{26.06}$ orbit within the slice defined by the template (265) (projected on arbitrary basis, details of which are irrelevant for the current discussion). The symmetry-reduced relative periodic orbit closes onto itself after one period, as it should. The second thing we need to check is whether ergodic trajectories cross the slice border. As we explained in Sect. 3.3.2, if a trajectory visits the slice border (97), the phase velocity (96) diverges. For this reason, we reduced the translation symmetry of an ergodic trajectory for 200 time units using the template (265) and measured $d\ell/d\tau$. Figure 26(b) shows the result of this experiment, where time sampling points of simulation are marked with red + signs. While we do see two peaks in Figure 26, these instances are still well resolved, and corresponding trajectory segments do not appear discontinuous.

For the chronological reasons we mentioned in the beginning of this section, results we show in Figure 26 are the only ones in this thesis that uses (265) as the slice template. However, since validation of this approach is crucial for the extendibility of the first Fourier mode slice method to direct products of SO(2), we decided to present this treatment here.

6.3.1.2 A first Fourier mode slice template from dynamics

We shall now explain the adaptation of first Fourier mode slice in ref. [116], which we used in the results of the remaining of this chapter. Prior to the work presented in the previous two chapters of this thesis, Willis *et al.* [115] used method of slices in pipe flow by setting multiple slices and transition rules between them, such that individual slice borders are avoided by the symmetry reduced flow. These slice templates were typically found in state space regions corresponding to low energy solutions, motivated by the experimental

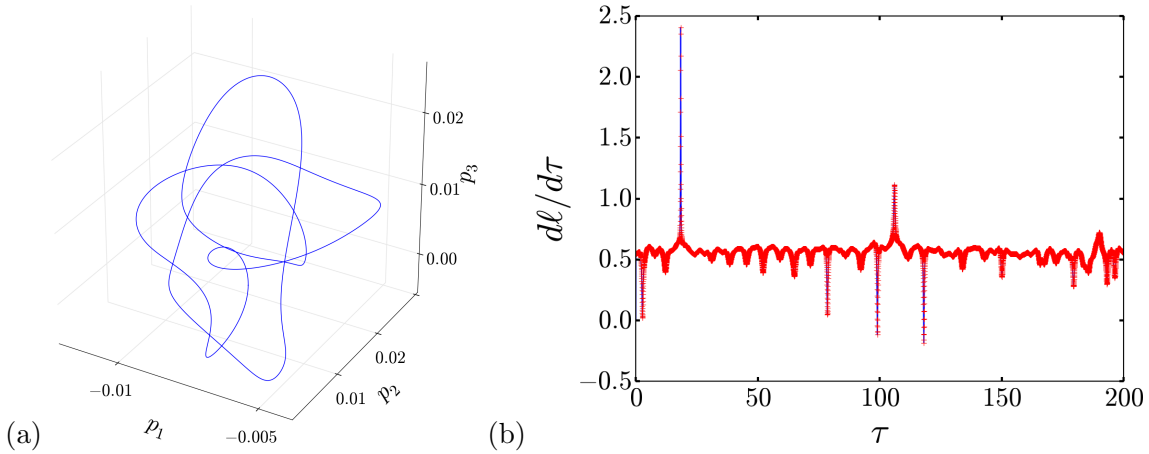

Figure 26: (a) In the first Fourier mode slice Relative periodic orbit $\mathrm{RPO}_{26.06}$ becomes a periodic orbit. (b) A numerical experiment showing time derivative of the slice fixing shifts for a long ergodic trajectory.

observation that such slices had larger region of applicability. This approach was also followed at the early stages of this project. After we formulated first Fourier mode slice in ref. [14] , Willis *et al.* [116] adopted our method to the pipe flow by taking one of the slice templates of the previous approach, and setting all of its discretization elements (234), except the real parts of the ones with $k = \pm 1$. Such a construction corresponds to a flow field of the following form

$$\mathbf{u}'(r, \theta, z) = \mathbf{f}(r, \theta) \cos(2\pi z/L) \,. \tag{268}$$

For the shift-and-reflect invariant case at hand, the flow field (268) is a valid first Fourier mode slice template, and procedure of finding slice fixing shifts (266) and reducing streamwise translation symmetry (267) is exactly same as we described earlier in this section. The weakness of this approach is if we use a slice template in the form of (268) without shift-and-reflect restriction, then the azimuthal rotation operation might take translation symmetry-reduced states outside the slice, since f in (268) depends on θ. Therefore, it is hard to imagine the extendibility of this approach to the case of two commuting continuous symmetries. Nevertheless, at the current stage, we use this slice template to present our results. Applicability of this method was demonstrated in ref. [116] where the authors carried out numerical experiments, similar to ours in Figure 26(b), which showed that the flow rarely visits the vicinity of the slice border constructed this way.

6.3.2 Traveling waves and relative periodic orbits

In Chapter 4, we found all relative periodic orbits of the two-modes system by guessing their locations from a Poincaré return map. For the Kuramoto-Sivashinsky system, in Chapter 5, we had a globally stable relative periodic orbit for small system sizes, and we numerically followed this orbits' bifurcations and found longer orbits. Strategy adopted here is completely different, which we will summarize in this section.

Our starting hypothesis was "the state space of turbulence is shaped by the exact coherent structures". Assuming this is correct, then one would expect to see similarities in the behavior of turbulent trajectories if they are in the vicinity of an exact coherent structures.

For example, if a trajectory visits neighborhood of an equilibrium, then we would expect it to slow down, or if it visits neighborhood of a periodic orbit of period T, then we would expect it to approximately repeat itself after T. Such information is encoded in recurrence function

$$f(\tau, \tau_R) = \frac{\|\hat{a}(\tau) - \hat{a}(\tau - \tau_R)\|}{\|\hat{a}(\tau)\|} \tag{269}$$

for relative equilibria and relative periodic orbits since they respectively become equilibria and periodic orbits after continuous symmetry reduction. Willis *et al.* [116] found guesses for relative periodic orbits and relative equilibria from the minima of (269) obtained from turbulent trajectories $\hat{a}(\tau)$. These guesses were fed into a Newton-Krylov-hook step solver [110], which yielded the discovery of 8 relative equilibria and 38 relative periodic orbits of the pipe flow. In addition, by picking points on the unstable manifolds of different short relative periodic orbits and feeding them into multi point shooting Newton solver, 8 new relative periodic orbits were found [117]. Finally, the $m_0 = 4$ upper/lower branch (N4U/L) traveling waves of ref. [33] are numerically continued to the current domain, adding two more exact coherent structures to the list. A summary of the currently known exact coherent structures and their properties is given in Table 4.

6.3.3 Global visualizations - Principal Component Analysis

Arguably, the biggest difficulty in the study of infinite-dimensional the systems is the mere fact that humans can see only three dimensions at once. It is therefore crucial to have well-thought visualization methods. In Chapter 5, visualizing the unstable manifold of a relative periodic orbit enabled us to extract important dynamical information about the flow, and to find longer periodic orbits. Here, we take, again, an experimental approach to find coordinates where most of the dynamical information is contained using principal component analysis ([**pca??**]), which we already introduced in Sect. 5.4.

Here, the principal components p_i are found by the following procedure: We first generate $N = 2000$ data points a_i from different simulations of the turbulent dynamics; and then we take their discrete symmetry copies $g_\theta a_i$ and reduce their continuous symmetry as described in Sect. 6.3.1 to obtain the data set $\hat{a}_k$. Consider the data matrix X with $\hat{a}_k - \langle \hat{a} \rangle$ on its rows, where $\langle \hat{a} \rangle$ is the empirical mean of the data, then X has a singular value decomposition

$$X = U \Sigma W^T \,, \tag{270}$$

where U is a unitary matrix, Σ is rectangular diagonal with singular values σ_i of X and columns of W are the principal components p_i. p_i are ordered in decreasing principal component variances $\sigma_i^2 > \sigma_{i-1}^2, i = 1, 2, 3, \ldots$, therefore, they align at directions where the variance of the data is largest. A solutions is then projected on these coordinates by

$$\hat{a}_{p_i}(\tau) = \langle \hat{a}(\tau) - \langle \hat{a} \rangle, \, p_i \rangle_{L2} \,. \tag{271}$$

Projection of the relative periodic orbits, 5 traveling waves, and an ergodic trajectory found onto the first three principal components is shown in Figure 27. The reason we avoided showing remaining 5 traveling waves in these figures is because they appear to sit far from the turbulent set and relative periodic orbits, and make it harder to see the relevant orbits if included. First thing to note in Figure 27 is that there appears to be two clouds where relative periodic orbits are located. Ergodic trajectory spends most of its time in one of them, occasionally switching to the other; 4 times in the example shown from a simulation

Table 4: Summary of the exact coherent structures found so far. Travelling waves are labeled by their dissipation rates and relative periodic orbits labeled by their period T. Average rate of dissipation $\bar{D}$, average down-stream phase velocity $\bar{c}$, dimension of the unstable manifold d_U, real part of the largest stability eigenvalue / Floquet exponent μ^{max} is shown. Last column corresponds to the imaginary part ω of the leading stability eigenvalue for travelling waves and phase θ of the leading Floquet multiplier for relative periodic orbits. The family of relative periodic orbits which appear to have similar physical properties are grouped together and labeled with subscript F.

	$\bar{D}$	$\bar{c}$	d_U	$\mu^{\max}$	ω or θ		$\bar{D}$	$\bar{c}$	d_U	$\mu^{\max}$	ω or θ
$\mathrm{TW}_{N4l/1.38}$	1.38	1.238	3	0.1809	0	$\mathrm{TW}_{1.578}$	1.578	1.108	9	0.2877	0
$\mathrm{TW}_{2.039}$	2.039	1.091	7	0.1159	0	$\mathrm{TW}_{1.845}$	1.845	1.039	11	0.5166	0.891
$\mathrm{TW}_{1.968}$	1.968	1.105	9	0.1549	0.259	$\mathrm{TW}_{1.783}$	1.783	1.035	8	0.323	1.119
$\mathrm{TW}_{1.885}$	1.885	1.073	8	0.4568	0.206	$\mathrm{TW}_{2.041}$	2.041	1.095	8	0.1608	0
$\mathrm{TW}_{N4U/3.28}$	3.279	1.051	30	0.9932	1.89	$\mathrm{TW}_{1.926}$	1.926	1.096	8	0.2504	0.414
$\mathrm{RPO}_{F/6.668}$	1.805	1.12	3	0.0534	1.69	$\mathrm{RPO}_{F/33.81}$	1.805	1.128	5	0.0471	1.727
$\mathrm{RPO}_{F/13.195}$	1.839	1.117	5	0.0581	2.038	$\mathrm{RPO}_{F/33.968}$	1.806	1.127	5	0.0588	1.671
$\mathrm{RPO}_{F/20.427}$	1.809	1.128	5	0.0771	0	$\mathrm{RPO}_{F/40.609}$	1.814	1.125	5	0.0505	0.315
$\mathrm{RPO}_{F/26.861}$	1.84	1.121	5	0.0679	π	$\mathrm{RPO}_{F/47.449}$	1.826	1.126	5	0.0586	π
$\mathrm{RPO}_{F/26.964}$	1.826	1.124	6	0.0493	0.986	$\mathrm{RPO}_{F/53.876}$	1.83	1.124	6	0.0457	1.253
$\mathrm{RPO}_{F/27.299}$	1.815	1.126	4	0.0678	0.961						
$\mathrm{RPO}_{4.954}$	2.015	1.084	3	0.1509	1.643	$\mathrm{RPO}_{14.045}$	1.903	1.107	6	0.1403	π
$\mathrm{RPO}_{5.468}$	2.003	1.091	6	0.1452	1.351	$\mathrm{RPO}_{14.544}$	2.015	1.102	6	0.1846	0
$\mathrm{RPO}_{6.119}$	1.875	1.081	7	0.1912	0	$\mathrm{RPO}_{14.646}$	1.776	1.133	5	0.1473	π
$\mathrm{RPO}_{6.134}$	1.86	1.086	7	0.1596	0	$\mathrm{RPO}_{15.081}$	2.06	1.081	8	0.1392	0
$\mathrm{RPO}_{6.18}$	1.865	1.091	5	0.211	0	$\mathrm{RPO}_{15.46}$	1.781	1.146	7	0.1166	0
$\mathrm{RPO}_{6.359}$	1.769	1.054	11	0.2614	0	$\mathrm{RPO}_{15.798}$	1.869	1.125	6	0.1089	π
$\mathrm{RPO}_{6.458}$	2.117	1.074	7	0.2055	0	$\mathrm{RPO}_{15.915}$	1.951	1.106	8	0.1547	π
$\mathrm{RPO}_{7.246}$	1.982	1.105	5	0.209	0	$\mathrm{RPO}_{15.972}$	1.956	1.097	7	0.1473	π
$\mathrm{RPO}_{7.272}$	2.015	1.1	5	0.1852	0	$\mathrm{RPO}_{16.271}$	1.978	1.09	7	0.1454	1.977
$\mathrm{RPO}_{7.423}$	1.838	1.109	6	0.1195	0.387	$\mathrm{RPO}_{16.878}$	1.969	1.099	5	0.1219	π
$\mathrm{RPO}_{7.741}$	1.707	1.138	5	0.0983	0	$\mathrm{RPO}_{17.21}$	1.999	1.098	7	0.1523	π
$\mathrm{RPO}_{9.735}$	2.05	1.086	7	0.1872	π	$\mathrm{RPO}_{17.46}$	1.917	1.121	6	0.0842	0.205
$\mathrm{RPO}_{11.696}$	1.961	1.108	9	0.1129	π	$\mathrm{RPO}_{21.704}$	1.868	1.12	7	0.0951	π
$\mathrm{RPO}_{12.026}$	2.09	1.088	6	0.1476	0	$\mathrm{RPO}_{22.063}$	2.032	1.101	7	0.1352	1.723
$\mathrm{RPO}_{12.566}$	2.053	1.083	10	0.1677	π	$\mathrm{RPO}_{23.047}$	1.874	1.12	6	0.1848	0
$\mathrm{RPO}_{12.706}$	2.156	1.07	6	0.1692	1.083	$\mathrm{RPO}_{23.356}$	1.98	1.112	6	0.101	1.249
$\mathrm{RPO}_{13.592}$	1.987	1.099	7	0.1072	0	$\mathrm{RPO}_{26.049}$	2.028	1.097	8	0.1635	π

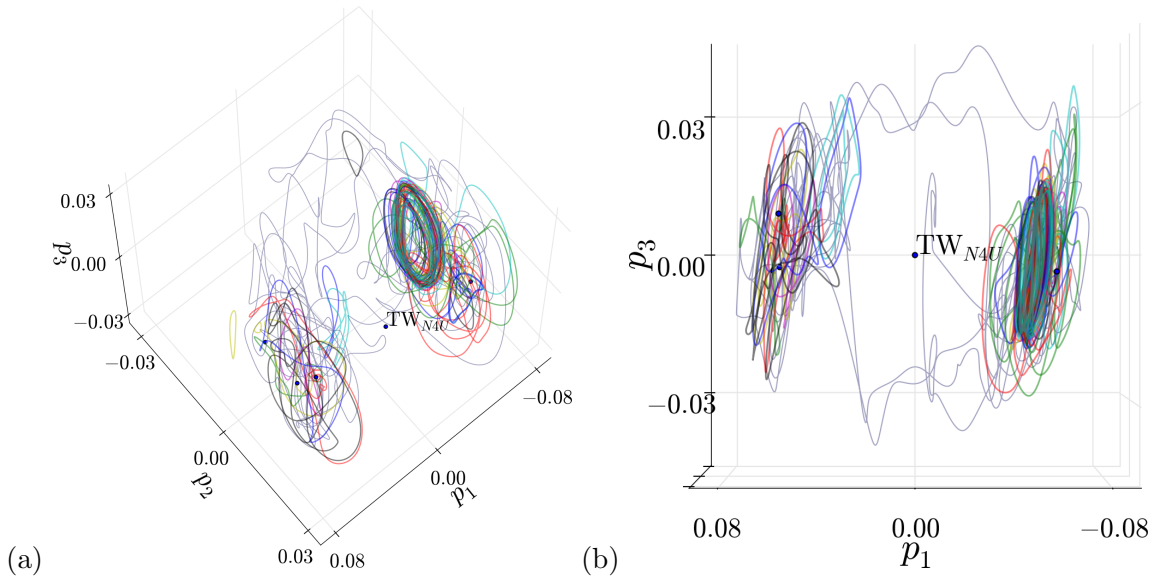

Figure 27: Relative periodic orbits and 5 traveling waves (marked with black dots) and an ergodic trajectory (gray, $\tau_F = 360$) of the pipe flow projected onto first three principal components from two different viewing angles.

of 360 time units. This is not a coincidence and two clouds are related by the discrete g_θ symmetry of the system. While, we show all relative periodic orbits and traveling waves on the side where they were numerically found; each of them have g_θ symmetry copies on the other side of the cloud, except the upper branch traveling wave $\mathrm{TW}_{N4U/3.28}$. The reason that $\mathrm{TW}_{N4U/3.28}$ does not have a g_θ-copy is because it is invariant under it; we emphasize this in the viewing angle of Figure 27 (b), where $\mathrm{TW}_{N4U/3.28}$ is located at $p_1 = p_3 = 0$.

Our motivation for using [**pca??**] for visualizations was to capture as much dynamical information as we can in three dimensions, but we ended up finding 2 out of 3 principal components aligned in the symmetry plane. This, of course, is not a good deal, and thus our next step is discrete symmetry reduction.

6.3.4 Fundamental domain

In Chapter 5, after SO(2) symmetry reduction, we reduced the remaining discrete symmetry of the system by introducing invariant polynomials. In principle, we can take a similar approach here, and first find the representation of discrete symmetry within the slice, and then transform to new coordinates that are invariant. However, we would have to face several difficulties in the process: Firstly, the representation of azimuthal half-rotation within the slice is not simple. Since the slice template is experimentally picked from a turbulent simulation, one would expect the action of g_θ to break the slice condition and the transformation that would bring the state back to the slice is presumably non-trivial. We could have overcome this by revising our slicing scheme, and picking a rotation-invariant slice template, which would then make the representation of rotations within the slice same as in the full state space. Second difficulty has to do with our representation of data (234) in `Openpipeflow`, where we have finite difference points in radial direction. If we produced polynomial invariants just as we did in Chapter 5 by multiplying adjacent state space coordinates directly, then the resulting polynomials would correspond to our specific

representation of data, which would not be reproducible by other researchers, unless they use the same computational scheme. The last difficulty we should mention is that most of our results in this chapter depend on particular norms, which we have some physical interpretation for. These insights would have been lost if we produced quadratic polynomials from our Fourier modes. For these reasons, we take a different approach in this sections that has its own issues, which are easier to overlook.

As it is clearly seen from Figure 27, $p_1 = 0$ hyperplane separates two discrete symmetry related halves of the state space. We define $p_1 > 0$ half of the state space as the *fundamental domain* [21] and bring all of our traveling wave, relative periodic orbit, and ergodic solution data to this region by transforming each state with $p_1 < 0$ by acting on them with g_θ. Using the same procedure we described in the previous section, we compute principal components from the data in the fundamental domain, and use these bases for visualizations.

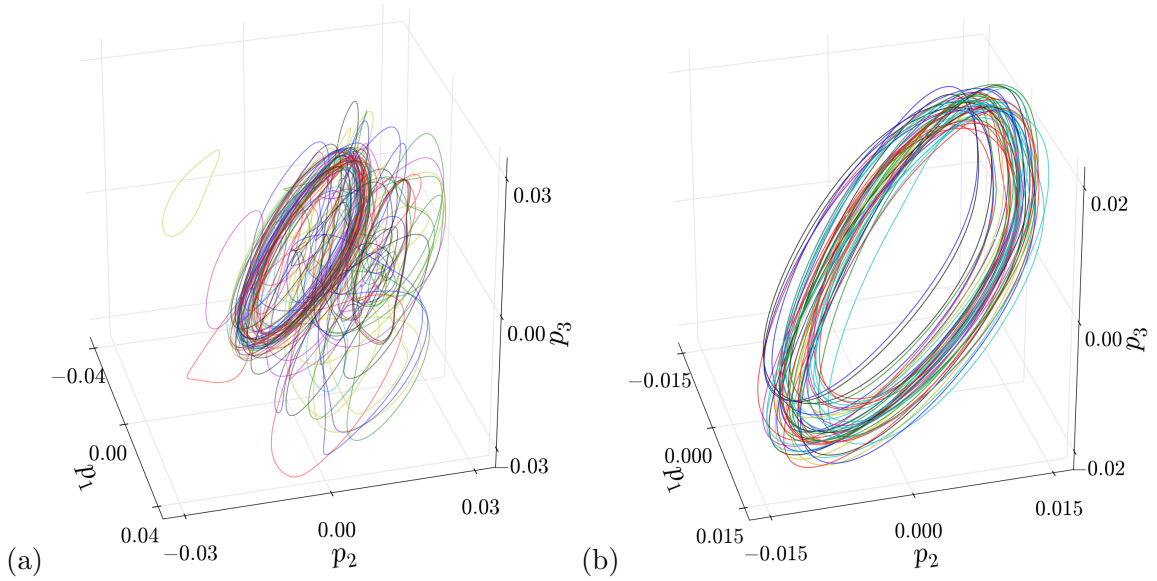

Figure 28: (a) Relative periodic orbits projected onto first three fundamental domain principal components. (b) 11 orbits, which appear to fill out a region of the state space.

Figure 28 (a) shows 45 relative periodic orbits listed on Table 4 in fundamental domain, projected onto first three principal components computed within the fundamental domain. Notice that in Figure 28 (a) a subset of orbits appear very close to each other; we show these 11 orbits in Figure 28. We listed these in Table 4 separate from the rest with a subscript F, which stands for 'first family'. Besides their striking similarities in the state space projections, these orbits also have similar physical properties such as the mean rate of dissipation and mean drift speeds. Moreover, their leading Floquet exponent is roughly an order of magnitude smaller then the rest of the relative periodic orbits, suggesting that these orbits may have a significant influence on the turbulent dynamics. We are going to present more results involving these orbits in the upcoming sections.

Before moving on, we should explain the shortcoming of the present discrete symmetry reduction scheme. Since g_θ is a discrete transformation, when the trajectories that cross $p_1 = 0$ hyperplane are brought back to the fundamental domain $p_1 > 0$, they become discontinuous. For the particular case at hand, we ignore this problem, since the switchings of ergodic trajectories between symmetry related saddles are rare, see Figure 27 (b). In

addition, since we have not found any (259) type relative periodic orbit that connects one cloud to the other, we do not need to worry about discontinuities that they will have either. We should emphasize that the fact that we could not find any relative periodic orbits that satisfies (259) does not mean that they do not exist. In fact, it is merely a consequence of our experimental approach of searching orbits nearby close recurrences. Since switchings between two symmetry-related saddles are quite rare, we did not have any seeds to search for relative periodic orbits in these occurrences.

6.3.5 Numerical experiments

We have found quite a few exact coherent structures, but what are they good for? In this section, we present results of simple numerical experiments to further develop our intuition about dynamical roles of exact coherent structures in the pipe flow turbulence. For this purpose, we are ran a long ergodic trajectory, until it laminarizes at the final time $\tau_F = 681.0\, D/U$. We then computed its minimum distance to all exact coherent structures for its lifetime. Let $\tilde{a}(\tau)$ and $\tilde{a}_c(\tau')$ respectively denote the ergodic trajectory and an exact coherent structure in the fundamental domain; then the minimum distance function is

$$d(\tau) = \min_{\tau'} \|\tilde{a}(\tau) - \tilde{a}_c(\tau')\| \,. \tag{272}$$

In (272), we did not specify, which metric we are going to use in computing the distances because we are going to use both $L2$ and low pass norms which we introduced in Sect. 6.1.2.

6.3.5.1 Switchings between symmetry copies

Within the shift-and-reflect invariant subspace, once the continuous symmetry is quotiened, the turbulent pipe flow consist of two chaotic saddles that are related to each other by a discrete half-domain rotation about the pipe axis. All the relative periodic orbits and the relative equilibria we found by searching nearby the close recurrences of the flow belonged one of these two saddles and had a symmetry copy on the other. Upper and lower branch traveling waves $\mathrm{TW}_{N4U/1.38}$ and $\mathrm{TW}_{N4L/3.28}$ are exceptions to this description. They were found as upper and lower branch solutions in a ref. [33] with an extra azimuthal half-rotation symmetry and numerically continued to the current domain. Therefore, they are invariant under rotation symmetry that relates two chaotic saddles and located in between them.

In order to investigate possible dynamical roles of these orbits, we computed the minimum distance (272) of ergodic trajectories from these orbits and the results are shown in Figure 29. For the most parts, these orbits are further away from the ergodic trajectory than relative periodic orbits; compare typical numbers to Figure 30. However, at certain instances, there are dips and/or bumps in the distances; which are more pronounced in the low pass norm. We found that these events coincide with episodes, in which ergodic trajectory leaves the fundamental domain and brought back by the discrete symmetry operation. We marked these instances with vertical dashed lines in Figure 30. Moreover, note at $\tau > 600$ in Figure 29, distance from the upper branch is very large, but the lower branch has a dip. This is because this is right before the laminarization of the system, which is mediated by the unstable manifold of the edge, to which the lower branch solution belongs.

6.3.5.2 Minimum distance from relative periodic orbits

Let us now turn our attention to the relative periodic orbits . We expect them to play an important role in describing turbulent dynamics, as they should be embedded in the

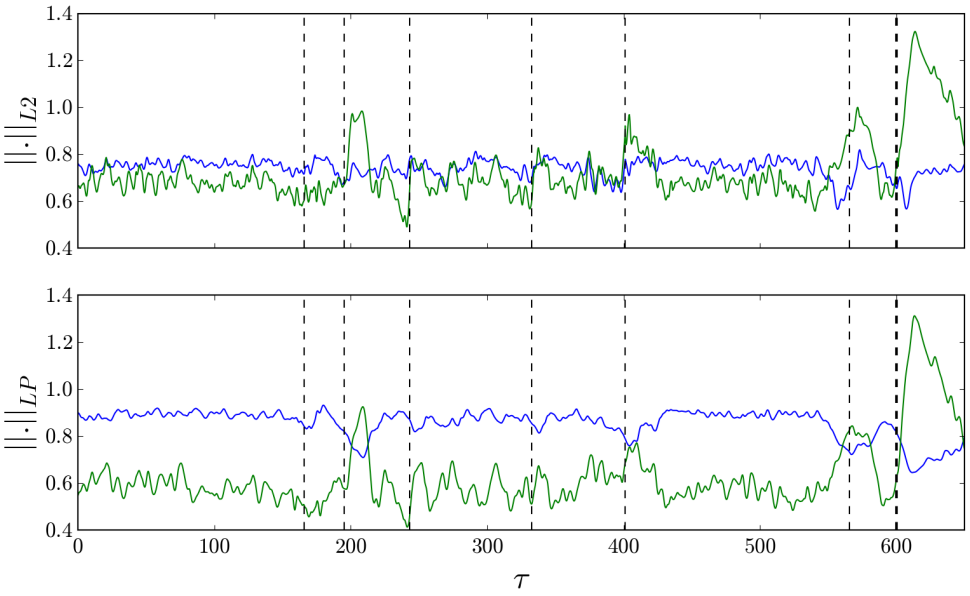

Figure 29: Distances from $\mathrm{TW}_{N4L/3.28}$ (blue) $\mathrm{TW}_{N4U/1.38}$ (green) and instances corresponding to the switchings between symmetry copies marked with vertical dashed lines.

chaotic set. However, when we look at the distances from all found relative periodic orbits for the lifetime of an ergodic trajectory, the outcome (Figure 30) is not very informative. The distance between the ergodic trajectory and almost all relative periodic orbits peaks at the same instances, which is against the description of chaotic dynamics as transient visits to the neighborhoods of different orbits. Notice, however, that the peaks that dominate the axes scales in Figure 30 corresponds to instances, at which the ergodic trajectory travels from one chaotic saddle to its symmetry copy. As we mentioned earlier, these excursions could have been captured by relative periodic orbits, which satisfies (259); however we do not have such a solution. Therefore, the peaks in Figure 30 corresponds to flow behavior, that is not captured any of the found relative periodic orbits .

Since we know that our relative periodic orbits are unable to capture dynamics that connects two chaotic saddles, we decided to restrict our attention to an episode, during which the dynamics stays within one. Figure 31 (a) shows 8 relative periodic orbits of the pipe flow and the ergodic trajectory for $\tau \in [0, 165] D/U$ projected onto fundamental domain principal components and Figure 31 (b) shows the minimum distances from these orbits. Figure 31 is too crowded to make a detailed observation, however, note that in Figure 31 (b), curves with different colors have minima at different instances throughout the evolution of turbulent dynamics. This suggests that the flow may indeed be bouncing between the neighborhoods of relative periodic orbits .

Our final example correspond to a much shorter time segment $\tau \in [135, 165]$, which illustrates a striking example of "shadowing". In Figure 32 (a), we show $\mathrm{RPO}_{F/6.668}$, $\mathrm{RPO}_{6.458}$, and the ergodic trajectory segment; and in Figure 32 (b) we show the minimum distance of ergodic trajectory from the relative periodic orbits shown. While the distance from $\mathrm{RPO}_{6.458}$ is initially larger than that from $\mathrm{RPO}_{6.668}$, this changes at about $\tau \approx 150$ and the ergodic trajectory appears to enter to the neighborhood of $\mathrm{RPO}_{6.458}$. Notice also the similarities between the ergodic trajectory and $\mathrm{RPO}_{6.458}$ on Figure 32 (a) after time 150,

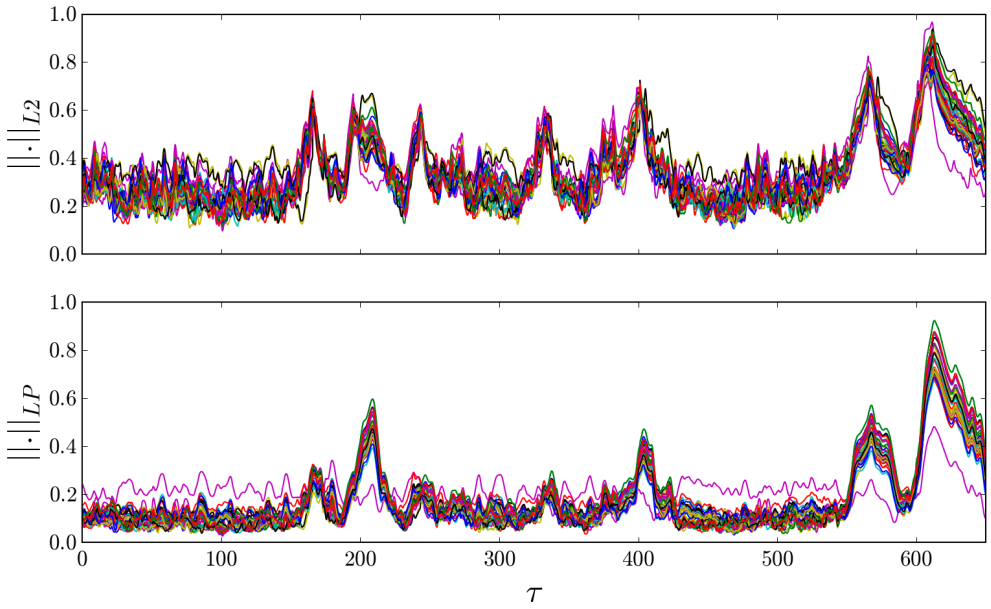

Figure 30: Minimum distance between ergodic trajectory and relative periodic orbits .

which is an indication of shadowing of ergodic trajectory by $\text{RPO}_{6.458}$.

Results of the numerical experiments presented in this section suggest that as long as flow stays in one of the symmetry related chaotic saddles, the relative periodic orbits within that saddle captures some portion of that dynamics. However, we should emphasize that these observations should be taken no serious than being suggestive. As we have mentioned in Sect. 6.1.2, the "distance" in any metric in the state space of a chaotic system might be very misleading.

Finally, we would like to make a general remark about the difference between $L2$ and low pass norms. Notice that in all distance figures of this section, $L2$ distances have more fluctuations compared to their low pass counterparts. Assuming that the small scale flow structures fluctuate more than the larger ones, this observation is consistent with our definition of the low pass metric (238), where large wave numbers (small wavelengths) are penalized. Note also that the differences between distances from traveling waves are more pronounced in the low pass norm in Figure 29, while in Figure 33 it appears to be the other way around. These, at first glance, might seem as two conflicting observations; however, they are in fact consistent with the definitions of norms. Upper and lower branch solutions, from which the distances are shown in Figure 29 have completely different physical properties, see Table 4, hence they are likely to have large scale differences. On the other hand, relative periodic orbits shown in Figure 32 have relatively similar physical properties, therefore their differences are more emphasized in $L2$ norm, in which the small scale structures are not suppressed.

6.3.6 Periodic orbit theory

In Chapter 4, we explained that the convergence of cycle expansions heavily relies on the topological organizations of cycles and grammar rules of symbolic dynamics. For the two-modes system, we obtained this information from a Poincaré return map, and showed that

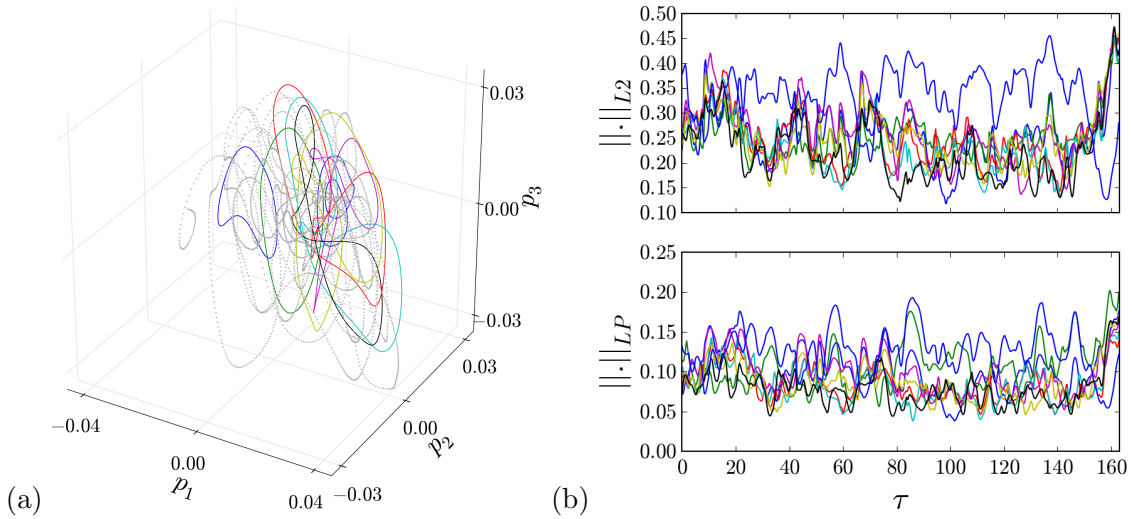

Figure 31: (a) Ergodic trajectory (gray dots) and 8 different relative periodic orbits (various colors) of the pipe flow projected on to the fundamental domain principal components. (b) Minimum distance of ergodic trajectory from the relative periodic orbits shown in (a).

symbolic dynamics with finite grammar rules yields quickly converging spectral determinants.

In the present problem, we do not have a Poincaré section that captures topological properties of periodic orbits, or a return map that yields grammar rules. We do not even now whether we have found all periodic orbits up to a certain period or not. However, we do have a set of orbits, namely the first family, which appear close by in visualizations of Figure 28 and have very similar physical properties as can be seen at Table 4. Having periods that are approximately integer multiples of the smallest 6.7, these orbits seem to belong to a fractal set that may be result of a local Smale horseshoe [105]. Motivated with these observations we propose the following: Sets of exact coherent structures such as the first family describe certain regions that has similar physical properties in the state space of turbulence. Each such family has to be a strange repeller, possibly connected to other families via longer relative periodic orbits .

An important quantity in the proposed description is rate of escape from strange repellers and we can use periodic orbit theory to predict this. In fact, we have already computed an escape rate for the two-modes system in Sect. 4.4.1. In the finite grammar approximation Sect. 4.3.2, we considered a subset of two-modes periodic orbits that had golden mean symbolic dynamics; and in Sect. 4.4.1, we found a finite escape rate for the state space region represented by these orbits.

In order to compute cycle expansions without knowing the topological ordering of the periodic orbits, we are going to adopt the *stability ordering* method. This was introduced by Dahlqvist and Russberg in studies of classical [25] and quantum [26] billiards. Dettmann and Morriss [29] used stability ordering for cycle expansions of strong-field Lorentz gas and Dettmann and Cvitanović [28] used the method to investigate intermittent diffusion. We start with rewriting (178) as a power series

$$1/\zeta = \prod_p (1 - t_p) = 1 - \sum_{p_1,p_2,\ldots p_k} (-1)^{k+1} t_{p_1} t_{p_1} \ldots t_{p_k} \,, \tag{273}$$

where the sum is carried over all distinct combinations of prime (non-repeating) cycles p_i.

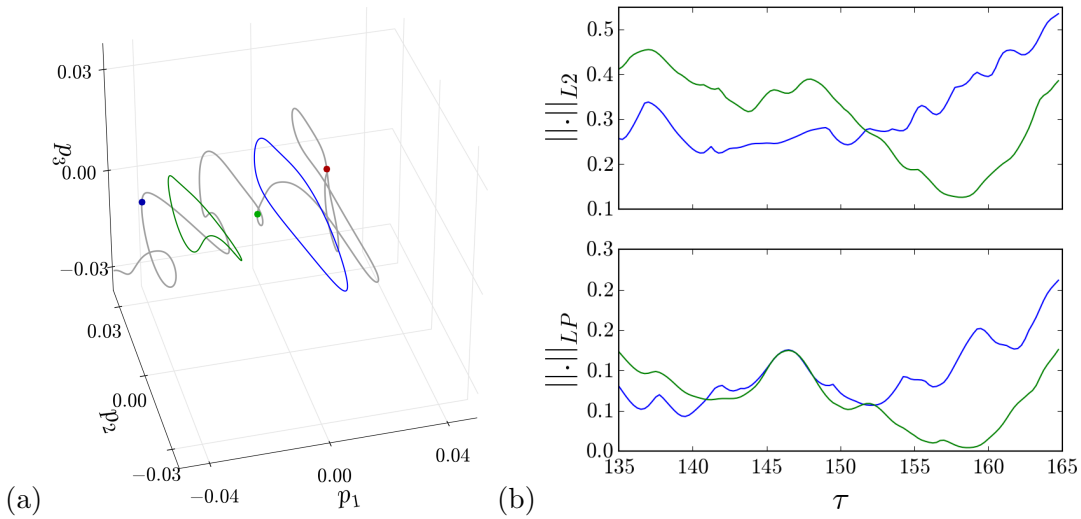

Figure 32: (a) Ergodic trajectory (gray), $\text{RPO}_{6.668}$ (blue), and $\text{RPO}_{6.458}$ (green) of the pipe flow projected on to the fundamental domain principal components. Instances $\tau = 140, 150, 160$ are marked on the ergodic trajectory with red, green, and blue respectively to indicate the direction of the flow. (b) Minimum distance of ergodic trajectory from the relative periodic orbits shown in (a).

We define each such combination as a *pseudo-cycle* with label $\pi = p_1 + p_2 + \ldots + p_k$ and pseudo-cycle weights

$$t_\pi = (-1)^{k+1} \frac{e^{(\beta\Omega_\pi - sT_\pi)}}{|\Lambda_\pi|}\,, \tag{274}$$

where

$$\begin{aligned} \Lambda_\pi &= \Lambda_{p_1}\Lambda_{p_2}\ldots\Lambda_{p_k}\,, \\ T_\pi &= T_{p_1} + T_{p_2}\ldots + T_{p_k}\,, \\ \Omega_\pi &= \Omega_{p_1} + \Omega_{p_2}\ldots + \Omega_{p_k}\,. \end{aligned} \tag{275}$$

With the definition (274), we can now express the dynamical zeta function (273) compactly as

$$1/\zeta = 1 - \sum_\pi t_\pi\,. \tag{276}$$

In stability ordering, one orders the terms in dynamical zeta function (276) in increasing $|\Lambda_\pi|$ and discards terms with $|\Lambda_\pi| > \Lambda_C$

$$1/\zeta = 1 - \sum_{|\Lambda_\pi|<\Lambda_C} (-1)^{k+1} \frac{e^{(\beta\Omega_\pi - sT_\pi)}}{|\Lambda_\pi|}\,. \tag{277}$$

Physical motivation behind the stability ordered zeta function (277) is the emphasis on the cycles that are less unstable. For example, if a system has a highly-unstable short cycle, the flow is unlikely to stay within its neighborhood, hence it will appear as a higher order correction in (277).

We computed the stability ordered cycle expansions (277) with the first family relative periodic orbits listed in Table 4 for $\Lambda_C \in [10, 10^3]$. We find the leading zero of the zeta

function by solving

$$1/\zeta(\beta = 0, s_0) = 0\,. \tag{278}$$

Figure 33 (a) shows the cycle expansion estimates of the escape rate $\gamma = -s_0$ against the stability cut-off Λ_C. All members of the first family except $\mathrm{RPO}_{F/53.876}$, enters into the zeta function at $\Lambda_C = 10^3$. Up to this value, escape rate have a converging trend around $\gamma \approx 0.095$. For larger values of Λ_C, we observed large fluctuations of γ, which indicates that we are missing cycles with $|\Lambda_p| > 10^3$.

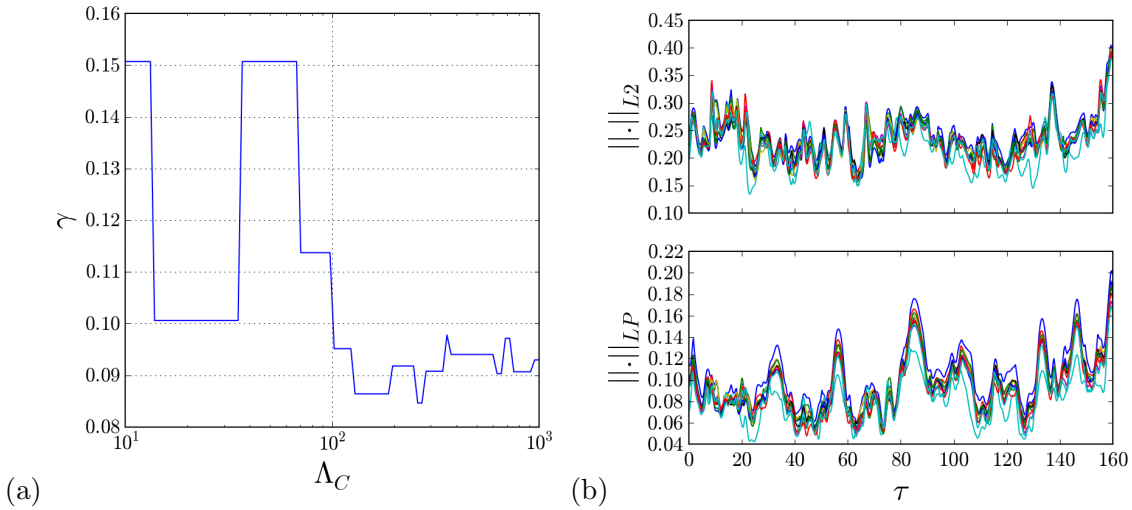

Figure 33: (a) Cycle expansion estimates of the escape rate γ from the neighborhood of the first family. (b) Minimum distances from first family relative periodic orbits.

An escape rate of $\gamma \approx 0.095$ tells us that turbulent trajectories within the neighborhood of the first family leaves this region of the state space after $\gamma^{-1} \approx 10.5D/U$. However, it is not clear how to test this number, since it is not obvious how to determine a boundary in the state space that sets the borders of the neighborhood of these orbits. To have an indicative, we turn our attention back to the minimum distance experiments. In Figure 33(b), we show the minimum distance of the ergodic trajectory to the first family relative periodic orbits in $L2$ and low pass norms for $\tau \in [0, 160]$. In order to have a time scale for the oscillations in the minimum distance experiments, we took Fourier transform of these measurements, which we show in Figure 34.

We see from Figure 34 that both time-dependent minimum distance measurements that in both metrics, highest-amplitude oscillations lie within the frequency range $f \in (0, 0.2)(U/D)$, which contains our escape rate prediction $\gamma \approx 0.095$. We should stress that this is just a sanity check, based on a single, non-exhaustive numerical experiment.

6.4 Conclusions

In this chapter, we presented a study of the turbulent pipe flow, with shift-and-reflect symmetry, which disallows for continuous rotations in the azimuthal direction. As we have mentioned earlier, the results we presented was part of a collaborative effort, and we tried to emphasize our own contributions to the project. These were analysis of the system's discrete symmetry in Sect. 6.2.1, applying fundamental domain method for reduction of this symmetry in Sect. 6.3.4, and tests of several hypotheses by numerical experiments in

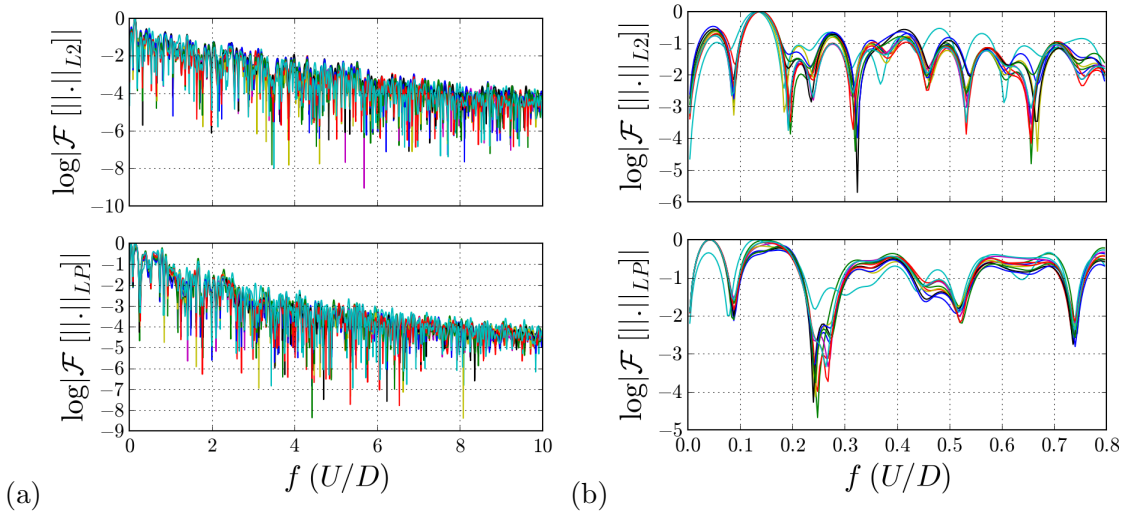

Figure 34: Fourier transforms of the time-dependent distance measurements shown in Figure 33(b) shown for $f \in (0, 10)U/D$ (a) and $f \in (0, 0.8)U/D$ (b).

Sect. 6.3.5 and by a periodic orbit theory calculation in Sect. 6.3.6. In addition to these, we have also shown in Sect. 6.3.1 that the first Fourier mode slice can be applied to the pipe flow by setting a slice template with a Bessel function dependence in the radial direction.

With our symmetry analysis, and **[pca??]** visualizations in Sect. 6.3.3, we understood that the turbulent pipe flow in the shift-and-reflect subspace has two chaotic saddles that are related by azimuthal rotation by π. Our numerical experiments in Sect. 6.3.5 showed some indication that as long as the ergodic trajectory stays in one of these chaotic saddles, relative periodic orbits embedded in the chaotic set influences the dynamics. Finally, in Sect. 6.3.6, we carried out a periodic orbit theory calculation with a subset of relative periodic orbits that appear to have similar physical properties, and predicted an escape rate for their neighborhood. Since, as of now, we do not have a way of designing an experiment to test this calculation, all we could do to make a sanity check of the predicted escape rate verified that it falls into the timescales that are observed in the system. We would like to emphasize that this calculation is only suggestive and the reason we presented it in this thesis is not to draw a strong conclusion from it, but to suggest new directions for turbulence research.

CHAPTER VII

CONCLUSION AND FUTURE DIRECTIONS

In this thesis, we asked the following question: Can we understand spatiotemporal chaos by studying exact coherent structures embedded in the chaotic sets? While we do not have a certain answer yet, we are optimistic. We believe the methods we presented in this thesis can help towards a deeper understanding of fluid turbulence and ultimately establishing a theory of turbulence with predictive power.

7.1 Summary of findings

Developments we presented in this thesis lie within the ongoing research program of studies of spatiotemporal chaos in terms of exact coherent structures. The contributions of the work presented in this thesis to the existing literature are:

- We developed first Fourier mode slice method for reducing SO(2) symmetry and its direct products, which are present when **[pde??]**s are studied in periodic domains.
- In our study of the two-modes system, we verified that periodic orbit theory extends to the systems with continuous symmetries when relative periodic orbits are used in calculations.
- For Kuramoto-Sivashinsky system, we combined invariant polynomials with the first Fourier mode slice to reduce the O(2) symmetry.
- We computed and visualized 1- and 2-dimensional unstable manifolds of periodic orbits in the symmetry reduced state space of the Kuramoto-Sivashinsky system.
- We applied the first Fourier mode slice to the pipe flow in a minimal computational cell and presented analysis that suggests relative periodic orbits play an important role in shaping the state space geometry of the turbulence.

The main message to be taken from the results of all three applications in this thesis is that the symmetry reduction is absolutely necessary for understanding the state space geometry of chaotic systems with continuous symmetries. The first Fourier mode slice can be used for this purpose when the symmetry group is SO(2).

7.2 Future work

Throughout this thesis, we applied first Fourier mode slice problems with only one continuous symmetry. For pipe flow, this meant the study of system in an invariant subspace, such that continuous symmetry in azimuthal direction is restricted to discrete rotations by π. While this study thought us many interesting aspects of the problem, this construction has little experimental relevance due to the fact that laboratory experiments cannot be designed in invariant subspaces. Therefore, a natural next step for our research is the simultaneous reduction of $\mathrm{SO}(2)_z \times \mathrm{O}(2)_\theta$ symmetry of the pipe flow. We have described how one can reduce axial and azimuthal symmetries $\mathrm{SO}(2)_z \times \mathrm{SO}(2)_\theta$ simultaneously in

Sect. 3.3.5, and reduced the axial translation symmetry of the shift-and-reflect symmetric pipe flow in Sect. 6.3.1.

For the remaining reflection symmetry, we can try to construct polynomial invariants for the pipe flow just as we did for the Kuramoto-Sivashinsky system in (201). However, since we multiply adjacent sign changing elements while constructing our invariants, such polynomials would depend on our particular discretization of the problem, and hard to reproduce in different numerical schemes. Therefore, before determining invariant polynomials, it makes sense to represent the data in a fully spectral form, such as

$$\mathbf{u}(r,\theta,z) = \sum_{n,k,m} \mathbf{u}_{nkm} s_n(r) e^{i(\alpha k z + m\theta)} \,, \tag{279}$$

where $s_n(r)$ are some functions that form a complete orthonormal basis for the radial expansion, satisfying pipe's boundary condition $s_n(1/2) = 0$. As it is irrelevant for the present discussion, we do not specify $s_n(r)$, but candidates are solenoidal (divergence-free) functions [78] or Bessel functions. One can convert data to the form (279) by post processing regardless of their numerical scheme.

Let us now write down the action of σ on discretization elements explicitly

$$\begin{aligned} \sigma[u,v,w](r,\theta,z) &= \sum_{n,k,m} [u,-v,w]_{nkm} g_n(r) e^{i(\alpha k z - m\theta)} \,, \\ &= \sum_{n,k,m} [u,-v,w]_{nk-m} g_n(r) e^{i(\alpha k z + m\theta)} \,, \end{aligned} \tag{280}$$

where in the second line, we replaced $m \to -m$ since it is summed over. This gives us the action of reflection in spectral representation as

$$\sigma[u,v,w]_{nkm} = [u,-v,w]_{nk-m} \,, \tag{281}$$

which is different than sign changes that we had in the Kuramoto-Sivashinsky system. As of this writing, finding an invariant basis for (281) remains an open problem.

7.3 Potential applications

We believe that the techniques we developed in this thesis can find applications in various studies of spatiotemporal chaos. The most obvious one is the continuous symmetry reduction in studies of **[pde??]** s under periodic boundary conditions. An important application that is not immediately obvious is the symmetry reduction of experimental data as it is uncommon to have experiments with periodic boundary conditions.

In ref. [35] Fedele, Abessi, and Roberts applied the first Fourier mode slice and another continuous symmetry reduction method based on fixing phase of a higher Fourier mode to the turbulent pipe flow experiments. They measured the fluid velocity in a finite region of the pipe in one dimension and took Fourier transform of their data and demonstrated that the symmetry reduction cancels stream-wise drifts of the turbulent structures. This approach can be extended to the three-dimensional velocity measurements to investigate roles of exact coherent structures in turbulence.

Bifurcation scenarios similar to that of the Kuramoto-Sivashinsky system that we studied in Sect. 5.5 are ubiquitous in high-dimensional systems. For example, Zammert and Eckhardt's study of the plane Poiseuille flow [121] and Avila *et al.* [8] study of transition to turbulence in pipe flow, both report torus bifurcations of relative periodic orbits along

transitions to chaos. Avila *et al.* [8] also showed that a localized, reflection invariant relative periodic orbit of the pipe flow has strikingly similar features to turbulent puffs. In the reflection-invariant subspace, this localized relative periodic orbit is initially stable, then undergoes a torus bifurcation, followed by chaotic dynamics as the Reynolds number is increased. Methods of Sect. 5.5 combined with the symmetry reduction of the pipe flow can lead to a detailed understanding of the state space geometry of turbulent puffs. Hence, we are planning to study these solutions in near future.

APPENDIX A

MULTIPLE SHOOTING METHOD FOR FINDING RELATIVE PERIODIC ORBITS OF THE TWO-MODES SYSTEM

Let us assume that we have a set of good guesses for a set of state space points, flight times and $1D$ symmetry group parameter increments $\{a_i^{(0)}\,,\,\tau_i^{(0)}\,,\,\phi_i^{(0)}\}$ such that the points $\{a_i^{(0)}\}$ lie close to the relative periodic orbit p such that

$$a_{i+1}^{(0)} \approx g(-\phi_i^{(0)}) f^{\tau_i^{(0)}}(a_i^{(0)}) \quad \text{cyclic in } i = 1, ..., n\,. \tag{282}$$

Here, the period and the shift of the relative periodic orbit p are $T_p \approx \sum \tau_i$, and $\phi_p \approx \sum \phi_i$. The Lagrangian description of the flow is then $a(\tau) = f^\tau(a(0))$. We want to determine corrections $(\Delta a_i\,,\,\Delta\tau_i\,,\,\Delta\phi_i)$ so that

$$\begin{aligned} a_{i+1} + \Delta a_{i+1} &= g(-\phi_i - \Delta\phi_i) f^{\tau_i + \Delta\tau_i}(a_i + \Delta a_i) \\ &\quad \text{cyclic in } i = 1, ..., n\,. \end{aligned} \tag{283}$$

To linear order in

$$\begin{aligned} &(\Delta a_i^{(m+1)}\,,\,\Delta\tau_i^{(m+1)}\,,\,\Delta\phi_i^{(m+1)}) \\ &= (a_i^{(m+1)} - a_i^{(m)}\,,\,\tau_i^{(m+1)} - \tau_i^{(m)}\,,\,\phi_i^{(m+1)} - \phi_i^{(m)}) \end{aligned} \tag{284}$$

the improved Newton guess $(a_i^{(m+1)}\,,\,\tau_i^{(m+1)}\,,\,\phi_i^{(m+1)})$ is obtained by minimizing the effect of perturbations along the spatial, time, and phase directions,

$$\begin{aligned} &a_{i+1}^{'} - g_{i+1} f^{\tau_i}(a_i) \\ &= g_{i+1}\left(J_{i+1}\Delta a_i + v_{i+1}\Delta\tau_i - t_{i+1}\Delta\phi_i\right)\,, \end{aligned} \tag{285}$$

where, for brevity, $a_i^{(m+1)} = a_i^{(m)} + \Delta a_i^{(m)} = a_i^{'}$, $a_i^{(m)} = a_i$, $g(-\phi_i) = g_{i+1}$, $v(a_i(\tau_i)) = v_{i+1}$, $J^{\tau_i}(a_i) = J_{i+1}$, $t(a_i(\tau_i)) = Ta_i(\tau_i) = t_{i+1}$, etc. For sufficiently good initial guesses, the improved values converge under Newton iterations to the exact values $(\Delta a_i\,,\,\Delta\tau_i\,,\,\Delta\phi_i)$ $= (\Delta a_i^{(\infty)}\,,\,\Delta\tau_i^{(\infty)}\,,\,\Delta\phi_i^{(\infty)})$ at a super-exponential rate.

In order to deal with the marginal multipliers along the time and group orbit directions, one needs to apply a pair of constraints, which eliminate variations along the marginal directions on the relative periodic orbit's $2D$ torus. These can be formulated as a local Poincaré section orthogonal to the flow and a local slice orthogonal to the group orbit at each point along the orbit,

$$\langle v(a_i), \Delta a_i\rangle = 0\,, \qquad \langle t(a_i), \Delta a_i\rangle = 0\,. \tag{286}$$

We can rewrite everything as one matrix equation:

$$A\Delta = E\,, \tag{287}$$

where

$$A = \begin{pmatrix} g_2 J_2 & g_2 v_2 & -T g_2 f^{\tau_1}(a_1) & \mathbf{-1} & 0 & 0 & 0 & \cdots & 0 & 0 & 0 \\ v(a_1) & 0 & 0 & 0 & 0 & 0 & 0 & \cdots & 0 & 0 & 0 \\ t(a_1) & 0 & 0 & 0 & 0 & 0 & 0 & \cdots & 0 & 0 & 0 \\ 0 & 0 & 0 & g_3 J_3 & g_3 v_3 & -T g_3 f^{\tau_2}(a_2) & \mathbf{-1} & \cdots & 0 & 0 & 0 \\ 0 & 0 & 0 & v(a_2) & 0 & 0 & 0 & \cdots & 0 & 0 & 0 \\ 0 & 0 & 0 & t(a_2) & 0 & 0 & 0 & \cdots & 0 & 0 & 0 \\ \vdots & \vdots & \vdots & \vdots & \vdots & \vdots & \vdots & \ddots & \vdots & \vdots & \vdots \\ \mathbf{-1} & 0 & 0 & 0 & 0 & 0 & 0 & \cdots & g_1 J_1 & g_1 v_1 & -T g_1 f^{\tau_1}(a_1) \\ 0 & 0 & 0 & 0 & 0 & 0 & 0 & \cdots & v(a_n) & 0 & 0 \\ 0 & 0 & 0 & 0 & 0 & 0 & 0 & \cdots & t(a_n) & 0 & 0 \end{pmatrix}, \tag{288}$$

$$\Delta = (\Delta a_1, \Delta\tau_1, \Delta\phi_1, \Delta a_2, \Delta\tau_2, \Delta\phi_2, \ldots, \Delta a_n, \Delta\tau_n, \Delta\phi_n)^T, \tag{289}$$

$$E = (a_2 - g_2 f^{\tau_1}(a_1), 0, 0, a_3 - g_3 f^{\tau_2}(a_2), 0, 0, \ldots, a_1 - g_1 f^{\tau_n}(a_n), 0, 0)^T. \tag{290}$$

We then solve (287) for Δ and update our initial guess by adding the vector of the computed Δ values to it and iterate.

APPENDIX B

PERIODIC SCHUR DECOMPOSITION

Here, we briefly summarize the periodic eigendecomposition [31] needed for the evaluation of Floquet multipliers for two-modes periodic orbits. Due to the non-hyperbolicity of the return map of Figure 10 (d), Floquet multipliers can easily differ by 100s of orders of magnitude even in a model as simple as the two-modes system.

We obtain the Jacobian of the relative periodic orbit as a multiplication of short-time Jacobians from the multiple shooting computation of Appendix A, so that

$$\hat{J} = g_n J_n g_{n-1} J_{n-1} \dots g_1 J_1 \;=\; \hat{J}_n \hat{J}_{n-1} \dots \hat{J}_1 \tag{291}$$

where $\hat{J}_i = g_i J_i \in \mathbb{R}^{4\times 4}, \quad i = 1, 2, ..., n$. This Jacobian is the same as the definition in (85) since J_i and g_i commute with each other and are multiplicative in time and phase, respectively. In order to determine the eigenvalues of $\hat{J}$, we bring each term appearing in the product (291) into periodic, real Schur form as follows:

$$\hat{J}_i = Q_i R_i Q_{i-1}^T \,, \tag{292}$$

where Q_i are orthogonal matrices that satisfy the cyclic property: $Q_0 = Q_n$. After this similarity transformation, we can define $R = R_k R_{k-1} ... R_1$ and re-write the Jacobian as:

$$\hat{J} = Q_n R Q_n^T \,. \tag{293}$$

The matrix R is, in general, block-diagonal with 1×1 blocks for real eigenvalues and 2×2 blocks for the complex pairs. It also has the same eigenvalues as $\hat{J}$. In our case, it is diagonal since all Floquet multipliers are real for relative periodic orbits of the two-modes system. For each relative periodic orbit, we have two marginal Floquet multipliers corresponding to the time evolution direction and the continuous symmetry direction, as well as one expanding and one contracting eigenvalue.

APPENDIX C

NUMERICAL INTEGRATION OF KURAMOTO-SIVASHINSKY SYSTEM

Throughout Chapter 5, we used the 16 Fourier mode truncation of Kuramoto-Sivashinsky equation (191), which renders the state space 30-dimensional. Sufficiency of this truncation was demonstrated for $L = 22$ in ref. [22]. In order to avoid the computational complexity of the discrete convolution, we rewrite (191) as

$$\dot{\tilde{u}}_k = (q_k^2 - q_k^4)\,\tilde{u}_k - i\frac{q_k}{2}\mathcal{F}[(\mathcal{F}^{-1}[\tilde{u}])^2]_k\,, \tag{294}$$

where $\mathcal{F}$ and $\mathcal{F}^{-1}$ denotes forward and backward Fourier transformations. We then find the elements of 30-dimensional velocity field as (192) as

$$v_{2k-1} = \mathrm{Re}\,\dot{\tilde{u}}_k\,, \quad v_{2k} = \mathrm{Im}\,\dot{\tilde{u}}_k\,, \quad k = 1, 2, \ldots, 15. \tag{295}$$

We compute stability matrix A (9) from partial derivatives of this velocity function.

For the results of Sect. 5.2, we numerically integrated (192) and (102) for Kuramoto-Sivashinsky equation using Exponential Time Differencing fourth-order Runge-Kutta (ETDRK4) method of ref. [66]. The `MATLAB/Octave` code is openly available at ref. [12].

In Sect. 5.5, we integrate (102) and its gradients (107) numerically, using a general purpose adaptive integrator `odeint` from `scipy.integrate` [65], which is a wrapper of `lsoda` from `ODEPACK` library [56].

Transformation of trajectories and tangent vectors to the fully symmetry-reduced state space (202) is applied as post-processing. For a trajectory $\hat{a}(\tau)$, we simply apply the reflection reducing transformation to obtain the trajectory as $\tilde{a}(\tau) = \tilde{a}(\hat{a}(\tau))$. Velocity field (95) transforms to (202) by acting with the Jacobian matrix

$$\tilde{v}(\tilde{a}) = \frac{d\tilde{a}(\hat{a})}{d\hat{a}}\hat{v}(\hat{a})\,.$$

Floquet vectors transform to the fully symmetry-reduced state space similarly, however, their computations in the first Fourier mode slice requires some care. Remember that the reflection symmetry remains after the continuous symmetry reduction, and its action is represented by (199). Thus, denoting finite time flow induced by (95) by $\hat{f}^\tau(\hat{a})$, pre-periodic orbit within the slice satisfies

$$\hat{a}_{ppo} = \hat{\sigma}\hat{f}^{T_p}(\hat{a}_{ppo})\,,$$

with its linear stability given by the spectrum of the Jacobian matrix

$$\hat{J}_{ppo} = \hat{\sigma}\hat{J}^{T_p}(\hat{a}_{ppo})\,,$$

where $\hat{J}^{T_p}(\hat{a}_{ppo})$ is the Jacobian matrix of the flow function $\hat{f}^{T_p}(\hat{a}_{ppo})$. Thus, in order to find the Floquet vectors in fully symmetry-reduced representation, we first find the eigenvectors $\hat{V}$ of the Jacobian matrix $\hat{J}_{ppo}$ and then transform them as $\tilde{V}(\tilde{a}) = d\tilde{a}(\hat{a}_{ppo})/d\hat{a}\,\hat{V}(\hat{a})$.

References

[1] R. A. Adams and J. J. F. Fournier, *Sobolev Spaces*, 2nd ed. (Academic, New York, 2003).

[2] D. Armbruster, J. Guckenheimer, and P. Holmes, "Heteroclinic cycles and modulated travelling waves in systems with O(2) symmetry", Physica D **29**, 257–282 (1988).

[3] D. Armbruster, J. Guckenheimer, and P. Holmes, "Kuramoto-Sivashinsky dynamics on the center-unstable manifold", SIAM J. Appl. Math. **49**, 676–691 (1989).

[4] V. I. Arnol'd, *Geometrical Methods in the Theory of Ordinary Differential Equations* (Springer, Berlin, 1982).

[5] R. Artuso, E. Aurell, and P. Cvitanović, "Recycling of strange sets: I. Cycle expansions", Nonlinearity **3**, 325–359 (1990).

[6] R. Artuso, E. Aurell, and P. Cvitanović, "Recycling of strange sets: II. Applications", Nonlinearity **3**, 361–386 (1990).

[7] P. Ashwin and I. Melbourne, "Noncompact drift for relative equilibria and relative periodic orbits", Nonlinearity **10**, 595–616 (1997).

[8] M. Avila, F. Mellibovsky, N. Roland, and B. Hof, "Streamwise-localized solutions at the onset of turbulence in pipe flow", Phys. Rev. Lett. **110**, 224502 (2013).

[9] W.-J. Beyn and V. Thümmler, "Freezing solutions of equivariant evolution equations", SIAM J. Appl. Dyn. Syst. **3**, 85–116 (2004).

[10] G. D. Birkhoff, "Proof of the Ergodic Theorem", Proc. Natl. Acad. Sci. USA **17**, 656–660 (1931).

[11] R. Bowen, *Equilibrium States and the Ergodic Theory of Anosov Diffeomorphisms* (Springer, Berlin, 1975).

[12] N. B. Budanur, FFM Slice, GitHub.com/burakbudanur/ffmSlice, 2014.

[13] N. B. Budanur, D. Borrero-Echeverry, and P. Cvitanović, "Periodic orbit analysis of a system with continuous symmetry - A tutorial", Chaos **25**, 073112 (2015).

[14] N. B. Budanur, P. Cvitanović, R. L. Davidchack, and E. Siminos, "Reduction of the SO(2) symmetry for spatially extended dynamical systems", Phys. Rev. Lett. **114**, 084102 (2015).

[15] M. Budišić and I. Mezić, "Geometry of the ergodic quotient reveals coherent structures in flows", Physica D **241**, 1255–1269 (2012), http://arXiv.org/abs/1204.2050.

[16] E. Cartan, *La méthode du repère mobile, la théorie des groupes continus, et les espaces généralisés*, Vol. 5, Exposés de Géométrie (Hermann, Paris, 1935).

[17] A. Chenciner, "A note by Poincaré", Regul. Chaotic Dyn. **10**, 119–128 (2005).

[18] F. Christiansen, P. Cvitanović, and V. Putkaradze, "Spatiotemporal chaos in terms of unstable recurrent patterns", Nonlinearity **10**, 55–70 (1997).

[19] R. H. Cushman and L. M. Bates, *Global Aspects of Classical Integrable Systems* (Birkhäuser, Boston, 1997).

[20] P. Cvitanović, "Invariant measurement of strange sets in terms of cycles", Phys. Rev. Lett. **61**, 2729–2732 (1988).

[21] P. Cvitanović and B. Eckhardt, "Symmetry decomposition of chaotic dynamics", Nonlinearity **6**, 277–311 (1993), http://arXiv.org/abs/chao-dyn/9303016.

[22] P. Cvitanović, R. L. Davidchack, and E. Siminos, "On the state space geometry of the Kuramoto-Sivashinsky flow in a periodic domain", SIAM J. Appl. Dyn. Syst. **9**, 1–33 (2010).

[23] P. Cvitanović, D. Borrero-Echeverry, K. Carroll, B. Robbins, and E. Siminos, "Cartography of high-dimensional flows: A visual guide to sections and slices", Chaos **22**, 047506 (2012).

[24] P. Cvitanović, R. Artuso, R. Mainieri, G. Tanner, and G. Vattay, *Chaos: Classical and Quantum* (Niels Bohr Inst., Copenhagen, 2017).

[25] P. Dahlqvist, "Determination of resonance spectra for bound chaotic systems", J. Phys. A **27**, 763–785 (1994).

[26] P. Dahlqvist and G. Russberg, "Periodic orbit quantization of bound chaotic systems", J. Phys. A **24**, 4763–4778 (1991).

[27] G. Dangelmayr, "Steady-state mode interactions in the presence of O(2)-symmetry", Dyn. Sys. **1**, 159–185 (1986).

[28] C. P. Dettmann and P. Cvitanović, "Cycle expansions for intermittent diffusion", Phys. Rev. E **56**, 6687 (1997).

[29] C. P. Dettmann and G. P. Morriss, "Stability ordering of cycle expansions", Phys. Rev. Lett. **78**, 4201–4204 (1997).

[30] R. L. Devaney, *An Introduction to Chaotic Dynamical systems*, 2nd ed. (Westview Press, 2008).

[31] X. Ding and P. Cvitanović, "Periodic eigendecomposition and its application in Kuramoto-Sivashinsky system", SIAM J. Appl. Dyn. Syst. **15**, 1434–1454 (2016).

[32] Y. Duguet, C. C. T. Pringle, and R. R. Kerswell, "Relative periodic orbits in transitional pipe flow", Phys. Fluids **20**, 114102 (2008).

[33] Y. Duguet, A. P. Willis, and R. R. Kerswell, "Transition in pipe flow: the saddle structure on the boundary of turbulence", J. Fluid Mech. **613**, 255–274 (2008).

[34] H. Faisst and B. Eckhardt, "Traveling waves in pipe flow", Phys. Rev. Lett. **91**, 224502 (2003).

[35] F. Fedele, O. Abessi, and P. J. Roberts, "Symmetry reduction of turbulent pipe flows", J. Fluid Mech. **779**, 390–410 (2015).

[36] C. L. Fefferman, Existence and smoothness of the Navier-Stokes equation, 2000.

[37] M. Fels and P. J. Olver, "Moving coframes: I. A practical algorithm", Acta Appl. Math. **51**, 161–213 (1998).

[38] M. Fels and P. J. Olver, "Moving coframes: II. Regularization and theoretical foundations", Acta Appl. Math. **55**, 127–208 (1999).

[39] N. Fenichel, "Persistence and smoothness of invariant manifolds for flows", Indiana Univ. Math. J. **21**, 193–226 (1971).

[40] M. Field, "Equivariant dynamical systems", Bull. Amer. Math. Soc. **76**, 1314–1318 (1970).

[41] M. J. Field, "Equivariant dynamical systems", Trans. Amer. Math. Soc. **259**, 185–205 (1980).

[42] U. Frisch, *Turbulence* (Cambridge Univ. Press, Cambridge, 1996).

[43] S. Froehlich and P. Cvitanović, "Reduction of continuous symmetries of chaotic flows by the method of slices", Commun. Nonlinear Sci. Numer. Simul. **17**, 2074–2084 (2012), http://arXiv.org/abs/1101.3037.

[44] K. Gatermann, *Computer Algebra Methods for Equivariant Dynamical Systems* (Springer, New York, 2000).

[45] J. F. Gibson, J. Halcrow, and P. Cvitanović, "Visualizing the geometry of state-space in plane Couette flow", J. Fluid Mech. **611**, 107–130 (2008).

[46] R. Gilmore and C. Letellier, *The Symmetry of Chaos* (Oxford Univ. Press, Oxford, 2007).

[47] M. Golubitsky and I. Stewart, *The Symmetry Perspective* (Birkhäuser, Boston, 2002).

[48] M. Golubitsky, I. Stewart, and D. G. Schaeffer, *Singularities and Groups in Bifurcation Theory*, Vol. 2 (Springer, New York, 1988).

[49] J. M. Greene and J.-S. Kim, "The steady states of the Kuramoto-Sivashinsky equation", Physica D **33**, 99–120 (1988).

[50] J. Guckenheimer and P. Holmes, *Nonlinear Oscillations, Dynamical Systems, and Bifurcations of Vector Fields* (Springer, New York, 1983).

[51] M. C. Gutzwiller, "Phase-integral approximation in momentum space and the bound states of an atom", J. Math. Phys. **8**, 1979–2000 (1967).

[52] M. C. Gutzwiller, "Phase-integral approximation in momentum space and the bound states of an atom. II", J. Math. Phys. **10**, 1004–1020 (1969).

[53] G. Hagen, "Über die bewegung des wassers in engen cylindrischen röhren", Ann. Phys. **122**, 423–442 (1839).

[54] G. Haller and I. Mezić, "Reduction of three-dimensional, volume-preserving flows with symmetry", Nonlinearity **11**, 319–339 (1998).

[55] M. Hénon, "A two-dimensional mapping with a strange attractor", Commun. Math. Phys. **50**, 94–102 (1976).

[56] A. C. Hindmarsh, "ODEPACK, a systematized collection of ODE solvers", in *Scientific Computing*, Vol. 1, edited by R. S. Stepleman (North-Holland, Amsterdam, 1983), pp. 55–64.

[57] B. Hof, A. Juel, and T. Mullin, "Scaling of the turbulence transition threshold in a pipe", Phys. Rev. Lett. **91**, 244502 (2003).

[58] B. Hof, C. W. H. van Doorne, J. Westerweel, F. T. M. Nieuwstadt, H. Faisst, B. Eckhardt, H. Wedin, R. R. Kerswell, and F. Waleffe, "Experimental observation of nonlinear traveling waves in turbulent pipe flow", Science **305**, 1594–1598 (2004).

[59] B. Hof, J. Westerweel, T. M. Schneider, and B. Eckhardt, "Finite lifetime of turbulence in shear flows", Nature **443**, 59–62 (2006).

[60] P. Holmes, J. L. Lumley, and G. Berkooz, *Turbulence, Coherent Structures, Dynamical Systems and Symmetry* (Cambridge Univ. Press, Cambridge, 1996).

[61] E. Hopf, "A mathematical example displaying features of turbulence", Commun. Pure Appl. Math. **1**, 303–322 (1948).

[62] R. Hoyle, *Pattern Formation: An Introduction to Methods* (Cambridge Univ. Press, Cambridge, 2006).

[63] C. Huygens, *L'Horloge à Pendule* (Swets & Zeitlinger, Amsterdam, 1673).

[64] C. A. Jones and M. R. E. Proctor, "Strong spatial resonance and travelling waves in Benard convection", Phys. Lett. A **121**, 224–228 (1987).

[65] E. Jones, T. Oliphant, P. Peterson, et al., SciPy: Open source scientific tools for Python, 2001.

[66] A.-K. Kassam and L. N. Trefethen, "Fourth-order time-stepping for stiff PDEs", SIAM J. Sci. Comput. **26**, 1214–1233 (2005).

[67] G. Kawahara and S. Kida, "Periodic motion embedded in plane Couette turbulence: Regeneration cycle and burst", J. Fluid Mech. **449**, 291 (2001).

[68] I. G. Kevrekidis, B. Nicolaenko, and J. C. Scovel, "Back in the saddle again: a computer assisted study of the Kuramoto-Sivashinsky equation", SIAM J. Appl. Math. **50**, 760–790 (1990).

[69] T. Kreilos and B. Eckhardt, "Periodic orbits near onset of chaos in plane Couette flow", Chaos **22**, 047505 (2012).

[70] M. Krupa, "Bifurcations of relative equilibria", SIAM J. Math. Anal. **21**, 1453–1486 (1990).

[71] Y. Kuramoto and T. Tsuzuki, "On the formation of dissipative structures in reaction–diffusion systems", Progr. Theor. Phys. **54**, 687–699 (1975).

[72] Y. Lan and P. Cvitanović, "Unstable recurrent patterns in Kuramoto-Sivashinsky dynamics", Phys. Rev. E **78**, 026208 (2008).

[73] Y. Lan, C. Chandre, and P. Cvitanović, "Variational method for locating invariant tori", Phys. Rev. E **74**, 046206 (2006).

[74] E. N. Lorenz, "Deterministic nonperiodic flow", J. Atmos. Sci. **20**, 130–141 (1963).

[75] F. Mellibovsky and B. Eckhardt, "Takens–Bogdanov bifurcation of travelling-wave solutions in pipe flow", J. Fluid Mech. **670**, 96–129 (2011).

[76] F. Mellibovsky and B. Eckhardt, "From travelling waves to mild chaos: A supercritical bifurcation cascade in pipe flow", J. Fluid Mech. **709**, 149–190 (2012).

[77] A. Meseguer, "Streak breakdown instability in pipe Poiseuille flow", Phys. Fluids **15**, 1203–1213 (2003).

[78] A. Meseguer and F. Mellibovsky, "On a solenoidal Fourier-Chebyshev spectral method for stability analysis of the Hagen–Poiseuille flow", Appl. Numer. Math. **57**, 920–938 (2007).

[79] Á. Meseguer and L. N. Trefethen, "Linearized pipe flow to Reynolds number 10^7", J. Comput. Phys. **186**, 178–197 (2003).

[80] R. Miranda and E. Stone, "The proto-Lorenz system", Phys. Lett. A **178**, 105–113 (1993).

[81] T. Mullin and J. Peixinho, "Recent observations of the transition to turbulence in a pipe", in *IUTAM Symposium on Laminar-Turbulent Transition*, Vol. 78, edited by R. Govindarajan, Fluid Mechanics and Its Applications (Springer, New York, 2006), pp. 45–55.

[82] M. Nagata, "Three-dimensional finite-amplitude solutions in plane Couette flow: bifurcation from infinity", J. Fluid Mech. **217**, 519–527 (1990).

[83] M. Nagata, "Three-dimensional traveling-wave solutions in plane Couette flow", Phys. Rev. E **55**, 2023–2025 (1997).

[84] W. Pfenninger, "Transition in the inlet length of tubes at high reynolds numbers", in *Boundary layer and flow control*, edited by G. V. Lachmann (Pergamon, Oxford, UK, 1961), pp. 970–980.

[85] N. Platt, L. Sirovich, and N. Fitzmaurice, "An investigation of chaotic Kolmogorov flows", Phys. Fluids A **3**, 681–696 (1991).

[86] H. Poincaré, "Sur les solutions périodiques et le principe de moindre action", C. R. Acad. Sci. Paris **123**, 915–918 (1896).

[87] J. L. Poiseuille, "Recherches expérimentales sur le mouvement des liquides dans les tubes de très-petits diamètres", C. R. Acad. Sci. Paris **11**, 961 (1840).

[88] J. Porter and E. Knobloch, "Dynamics in the 1:2 spatial resonance with broken reflection symmetry", Physica D **201**, 318–344 (2005).

[89] C. C. T. Pringle and R. R. Kerswell, "Asymmetric, helical, and mirror-symmetric traveling waves in pipe flow", Phys. Rev. Lett. **99**, 074502 (2007).

[90] C. C. T. Pringle, Y. Duguet, and R. Kerswell, "Highly symmetric travelling waves in pipe flow", Philos. Trans. R. Soc. A **367**, 457–472 (2009).

[91] E. L. Rempel and A. C. Chian, "Intermittency induced by attractor-merging crisis in the Kuramoto-Sivashinsky equation", Phys. Rev. E **71**, 016203 (2005).

[92] E. L. Rempel, A. C. Chian, E. E. Macau, and R. R. Rosa, "Analysis of chaotic saddles in high-dimensional dynamical systems: the Kuramoto-Sivashinsky equation", Chaos **14**, 545–56 (2004).

[93] E. L. Rempel, A. C. Chian, and R. A. Miranda, "Chaotic saddles at the onset of intermittent spatiotemporal chaos", Phys. Rev. E **76**, 056217 (2007).

[94] O. Reynolds, "On the dynamical theory of incompressible viscous flows and the determination of the criterion", Proc. Roy. Soc. Lond. Ser. A **56**, 40–45 (1894).

[95] O. E. Rössler, "An equation for continuous chaos", Phys. Lett. A **57**, 397–398 (1976).

[96] C. W. Rowley and J. E. Marsden, "Reconstruction equations and the Karhunen-Loéve expansion for systems with symmetry", Physica D **142**, 1–19 (2000).

[97] D. Ruelle, "Bifurcations in presence of a symmetry group", Arch. Rational Mech. Anal. **51**, 136–152 (1973).

[98] D. Ruelle, *Thermodynamic formalism: the mathematical structure of equilibrium statistical mechanics*, 2nd (Cambridge Univ. Press, Cambridge, 2004).

[99] H. H. Rugh, "The correlation spectrum for hyperbolic analytic maps", Nonlinearity **5**, 1237 (1992).

[100] T. M. Schneider, B. Eckhardt, and J. Yorke, "Turbulence, transition, and the edge of chaos in pipe flow", Phys. Rev. Lett. **99**, 034502 (2007).

[101] H. Shan, Z. Zhang, and F. Nieuwstadt, "Direct numerical simulation of transition in pipe flow under the influence of wall disturbances", Int. J. Heat Fluid Flow **19**, 320–325 (1998).

[102] Y. G. Sinai, "Gibbs measures in ergodic theory", Russian Math. Surveys **27**, 21 (1972).

[103] G. I. Sivashinsky, "Nonlinear analysis of hydrodynamical instability in laminar flames - I. Derivation of basic equations", Acta Astronaut. **4**, 1177–1206 (1977).

[104] J. D. Skufca, J. A. Yorke, and B. Eckhardt, "Edge of Chaos in a parallel shear flow", Phys. Rev. Lett. **96**, 174101 (2006).

[105] S. Smale, "Differentiable dynamical systems", Bull. Amer. Math. Soc. **73**, 747–817 (1967).

[106] S. Smale, "Topology and mechanics, I." Inv. Math. **10**, 305–331 (1970).

[107] J.-L. Thiffeault, "Using multiscale norms to quantify mixing and transport", Nonlinearity **25**, 1–44 (2012), http://arXiv.org/abs/1105.1101.

[108] A. Vierkandt, "Über gleitende und rollende bewegung", Monatshefte für Math. und Phys. **III**, 31–54 (1892).

[109] D. Viswanath, "Symbolic dynamics and periodic orbits of the Lorenz attractor", Nonlinearity **16**, 1035–1056 (2003).

[110] D. Viswanath, "Recurrent motions within plane Couette turbulence", J. Fluid Mech. **580**, 339–358 (2007).

[111] F. Waleffe, "Three-dimensional coherent states in plane shear flows", Phys. Rev. Lett. **81**, 4140–4148 (1998).

[112] F. Waleffe, "Exact coherent structures in channel flow", J. Fluid Mech. **435**, 93–102 (2001).

[113] H. Wedin and R. R. Kerswell, "Exact coherent structures in pipe flow", J. Fluid Mech. **508**, 333–371 (2004).

[114] A. P. Willis and R. R. Kerswell, "Turbulent dynamics of pipe flow captured in a reduced model: puff relaminarisation and localised edge states", J. Fluid Mec. **619**, 213–233 (2009).

[115] A. P. Willis, P. Cvitanović, and M. Avila, "Revealing the state space of turbulent pipe flow by symmetry reduction", J. Fluid Mech. **721**, 514–540 (2013).

[116] A. P. Willis, K. Y. Short, and P. Cvitanović, "Symmetry reduction in high dimensions, illustrated in a turbulent pipe", Phys. Rev. E **93**, 022204 (2016).

[117] A. P. Willis, M. Farazmand, K. Y. Short, N. B. Budanur, and P. Cvitanović, Relative periodic orbits form the backbone of turbulent pipe flow, In preparation., 2017.

[118] S. Wold, K. Esbensen, and P. Geladi, "Principal component analysis", Chemometr. Intell. Lab. **2**, Proceedings of the Multivariate Statistical Workshop for Geologists and Geochemists, 37–52 (1987).

[119] A. Wolf, J. B. Swift, H. L. Swinney, and J. A. Vastano, "Determining Lyapunov exponents from a time series", Physica D **16**, 285–317 (1985).

[120] J. G. Yoder, *Unrolling Time: Christiaan Huygens and the Mathematization of Nature* (Cambridge Univ. Press, Cambridge, 1988).

[121] S. Zammert and B. Eckhardt, "Crisis bifurcations in plane Poiseuille flow", Phys. Rev. E **91**, 041003 (2015).